THE IMPACT OF CERIA-COATED PARTIAL-FLOW PARTICULATE FILTER ON DIESEL ENGINE COMBUSTION AND EMISSION CHARACTERISTICS USING B20

MYAT HSU THIN

A THESIS REPORT SUBMITTED IN PARTIAL FULFILLMENT
OF THE REQUIREMENTS FOR THE DEGREE OF
MASTER OF ENGINEERING IN AUTOMOTIVE ENGINEERING
SCHOOL OF ENGINEERING
KING MONGKUT'S INSTITUTE OF TECHNOLOGY LADKRABANG
YEAR 2023
KMITL-2023-EN-M-277-148

THESIS TITLE	The impact of ceria-coated partial-flow particulate filter on diesel engine combustion and emission characteristics using B20
STUDENT	Ms. Myat Hsu Thin
STUDENT ID	64601179
DEGREE	Master of Engineering
PROGRAM	Automotive and Advanced Transportation Engineering systems
THESIS ADVISOR	Assoc. Prof. Dr. Preechar Karin
CO-THESIS ADVISOR	Dr. Peerawat Saisirirat
CO-THESIS ADVISOR	Prof. Dr. Hidenori Kosaka

ABSTRACT

Due to increasingly stringent emissions standards, diesel engines and vehicles are now primarily oriented toward mitigating the release of hazardous exhaust gases and solid particulate matter. These emissions have garnered considerable attention due to their notable implications for environmental sustainability and public health. This paper examines the effects of incorporating a retrofit partial flow diesel particulate filter (P-DPF) on the combustion and emission characteristics of both the diesel engine and vehicle. The diesel engine was subjected to testing on an eddy current dynamometer, maintaining consistent engine speeds of 1000, 1500, and 2000 rpm while varying the engine torques at 56, 84, 112, and 140 Nm. The findings of the study indicated that the installation of the after-treatment system had no significant effects on fuel consumption and brake thermal efficiency. However, it was observed that the indicated thermal efficiency exhibited an increase, primarily attributable to the backpressure exerted by the after-treatment system. Additionally, despite receiving the same energy input, the positive indicated work experienced an elevation, resulting in higher combustion in-cylinder pressure and heat release rate. The retrofit partial flow diesel particulate filter (P-DPF) exhibited a significant reduction of approximately 65% in smoke emissions by effectively capturing and retaining soot particles within the partial filter. The analysis of nitrogen monoxide (NO), carbon dioxide (CO_2), oxygen (O_2), and exhaust temperature revealed that the trapped particles proceeded oxidation to CO_2 through the reaction with nitrogen dioxide (NO_2) and oxygen (O_2). Furthermore,

the soot morphology and nanostructure from the diesel engine would be analyzed by using the transmission electron microscope (TEM) and x-ray diffraction method (XRD). The diesel vehicle test was examined based on the New European Driving Cycle (NEDC) by employing non-catalyzed and ceria-coated P-DPF. The non-catalyzed P-DPF can reduce particle mass (PM) emissions by 57% while the ceria-coated one can achieve a reduction of 66%. The utilization of ceria P-DPF can reduce particle number (PN) by approximately 42%.

Keywords: Combustion characteristics, Thermal efficiency, Backpressure, Diesel oxidation catalyst, Partial flow diesel particulate filter.

ACKNOWLEDGEMENTS

I would like to express my heartfelt gratitude to everyone who has supported and contributed to the completion of this thesis. Without their invaluable assistance, guidance, and encouragement, this research would not have been possible.

First and foremost, I am deeply grateful to my supervisor, Assoc. Prof. Dr. Preechar Karin, for his unwavering support and invaluable guidance throughout the entire process. His expertise, patience, and insightful feedback have been instrumental in shaping this thesis and refining my research skills. I am truly fortunate to have had the opportunity to work under his mentorship.

I would also like to extend my sincere appreciation to my co-advisors, Prof. Dr. Hidenori Kosaka from School of Engineering, Tokyo Institute of Technology, and Dr. Peerawat Saisirirat from National Science and Technology Development Agency, for their valuable insights, constructive criticism, and suggestions that have greatly enhanced the quality of this research. Their expertise and thorough review of my work have significantly contributed to its overall improvement.

My sincere thanks go to the staff, KMITL laboratory members, and my seniors (Mr. Phyo Wai, Mr. Ban-Seok Oh, Mr. Poonnut Thaeviriyakul and Ms. Mizwe Mon Phyo) for providing an enriching academic environment and necessary resources to support my research. Their dedication to fostering an atmosphere of intellectual growth and learning has been immensely beneficial.

Lastly, I would like to acknowledge the support and encouragement of my fellow classmates and colleagues who have been a source of inspiration and motivation. Their intellectual discussions, shared experiences, and camaraderie have enriched my academic pursuits and made this journey more meaningful.

Myat Hsu Thin

TABLE OF CONTENTS

LIST OF TABLES

LIST OF FIGURES

CHAPTER 1

INTRODUCTION

1.1 Research Background

Owing to the deteriorating global climate challenge, there has been a significant surge in the adoption of electric vehicles in recent years, and this trend is expected to persist [1] [2] [3]. Despite efforts to expand charging infrastructure, a substantial gap persists between the distribution of charging stations and the extensive network of conventional petrol stations. Additionally, the comparatively higher upfront cost of electric vehicle adoption poses a notable impediment when contrasted with the more established and affordable internal combustion engine vehicles [4] [5] [6]. Meanwhile, diesel engines, known as compression ignition engines, remain prevalent, particularly in situations requiring substantial power and performance, specifically in the context of demanding heavy-duty applications. The diesel engine is widely acknowledged for its exceptional fuel economy and thermal efficiency, distinguishing it as a prominent choice among various internal combustion engine configurations. In Thailand, the combined consumption of gas and diesel fuels accounted for nearly 40% of total oil consumption in 2021 [7]. A report from the Department of Alternative Energy Development and Efficiency from 2016 to 2020 revealed a 5.7% increase in demand for diesel products over a span of four years [8]. However, diesel engines are associated with a notable drawback related to the emission of particulate matter (PM). In the context of Bangkok, Thailand, vehicles account for more than 40% of the total PM2.5 emissions, giving rise to considerable apprehension [9]. Diesel particulate matter is widely acknowledged as a hazardous substance, posing risks to public health and environmental well-being [10].

In order to address the prevalent issue of particulate matter (PM) emissions in Thailand, the government has implemented measures to restrict the quantity of PM emitted by vehicles, employing both conventional and contemporary approaches. The traditional regulations, applicable to older vehicles, involve opacity or intensity testing, which entails comparing the intensity of smoke before and after passing through a sensor. In contrast, modern vehicles are subject to regulations aligned with European emission standards, employing state-of-the-art instruments to measure emissions.

These modern standards incorporate a consistent driving protocol that simulates urban and extra-urban driving conditions. The onus of complying with modern standards primarily rests with automobile manufacturers for new vehicles, while adherence to classic standards falls under the responsibility of vehicle owners during the renewal of the registration tax. As regulations become more stringent, imposing lower limits on permissible PM emissions, there will be an increasing demand for the implementation of the exhaust after-treatment system such as diesel oxidation catalysts (DOCs) and diesel particulate filters (DPFs).

1.2 Objectives

This research aimed to achieve the following objectives.

- To conduct an analysis of the morphology, nanostructure, and chemical composition of soot emissions resulting from the use of biofuel blended diesel.
- To examine the effects of retrofitting a partial-flow diesel particulate filter (P-DPF) on the combustion, performance, and emission characteristics of a diesel engine.
- To observe the extent of particle and gaseous emissions reduction in diesel vehicles through the implementation of ceria-coated DOC and P-DPF.

1.3 Scope of the Work

This research was structured into three main components: analyzing the morphology and nanostructure of particulate matter (PM), examining the impact of P-DPF installation on the combustion and emission characteristics of the diesel engine, and assessing the reduction of particle and gaseous emissions in diesel vehicles through the utilization of ceria-coated DOC and P-DPF.

The microstructure of particulate matter (PM) was examined and investigated through the utilization of scanning electron microscopy (SEM). To analyze morphology, transmission electron microscopy (TEM) was employed to determine the agglomerate size and individual particle size. The TEM analysis also facilitated the assessment of the carbon nanostructure comprising the primary particles, focusing on parameters such as fringe length and interlayer spacing. A comparative analysis was conducted

with the X-ray diffraction method (XRD). Furthermore, the chemical and elemental composition of the PM was evaluated using energy-dispersive X-ray spectroscopy (EDS). The research simultaneously focused on investigating the combustion characteristics, encompassing parameters such as combustion pressure in relation to volume and crank angle, net heat release rate (NHRR), cumulative net heat release (CNHR), fuel consumption, and thermal efficiency. A comparative analysis was performed to assess the impact of employing the diesel oxidation catalyst (DOC) and partial-flow diesel particulate filter (P-DPF) on these combustion parameters. Throughout the study, a commercially available B20 fuel blend, comprising 20% biofuel and 80% diesel, was employed, while maintaining the engine configuration without any modifications. The gaseous emissions were quantified using an AVL exhaust gas analyzer, while the particulate matter (PM) was collected on a paper filter and its intensity was measured using a BOSCH smoke intensity meter.

The diesel vehicle test was carried out and simulated using the New European Driving Cycle (NEDC), which includes four urban driving cycles and one extra-urban driving cycle under no-load conditions. To evaluate the effects of the ceria catalytic partial flow filter, a comparative analysis was conducted on both real-time and specific driving cycle measurements to assess the reduction in gaseous and particulate emissions.

CHAPTER 2

Literature Review

2.1 Formation of particulate matter

To understand particulate matter (PM) comprehensively, it is imperative to examine the mechanism by which PM is generated, as this process is intrinsically connected to its inherent structure. The formation of particulate matter (PM) involves six commonly acknowledged processes: pyrolysis, nucleation, coalescence, surface growth, aggregation, and oxidation [11]. These processes collectively contribute to the intricate process of PM formation, as visually represented in **Figure 2-1**. It is important to note that these processes occur over varying time scales, ranging from microseconds to milliseconds [12]. Surface growth is a phenomenon wherein precursor molecules experience growth at the nanoparticle level. Concurrently, coalescence occurs, whereby smaller particles collide and merge, resulting in the formation of larger spherical particles. The process of aggregation contributes to the development of the distinct fractal structure often observed in soot formations [13]. The arrangement of carbon atoms in surface growth leads to hexagonal face-centered arrays bonded together in planes known as platelets, which then form layers and crystallites [14].

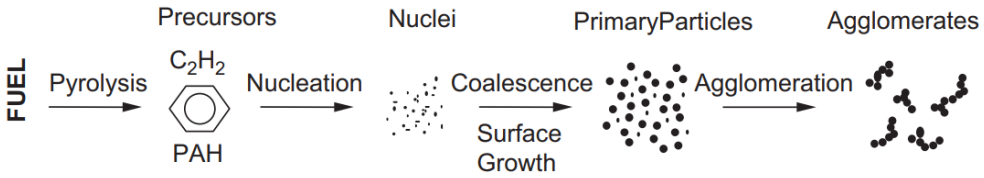

Figure 2-1 Schematic diagram of the PM formation process [11]

Engine-derived PM can be classified into three size categories based on the primary formation process dominating the particles: nucleation mode, accumulation mode, and coarse mode, as visually represented in **Figure 2-2**. The nuclei mode primarily encompasses particles ranging in diameter from 0.005 to 0.05 μm and predominantly consists of volatile organic and sulfur compounds formed during the process of exhaust dilution and cooling. The accumulation mode, with particle diameters ranging from 0.1 to 0.3 μm, contains the majority of particle mass. It consists of carbonaceous agglomerates and associated absorbed materials. As for the coarse mode, it ranges from approximately 5 μm and comprises accumulation mode particles

that have deposited on the surfaces of the engine cylinders and exhaust system. These particles may subsequently be re-entrained into the exhaust flow [15].

Moreover, the depiction of diluted and cooled diesel particulate matter (PM) can be observed in **Figure 2-3**, wherein it is characterized by the presence of two distinct particle types. Firstly, there are fractal-like agglomerates comprising primary particles primarily composed of carbon, accompanied by traces of metallic ash. These agglomerates are further coated with condensed heavier end organic compounds and sulfate. Secondly, nucleation particles are also present, which are composed of condensed hydrocarbons and sulfate [16].

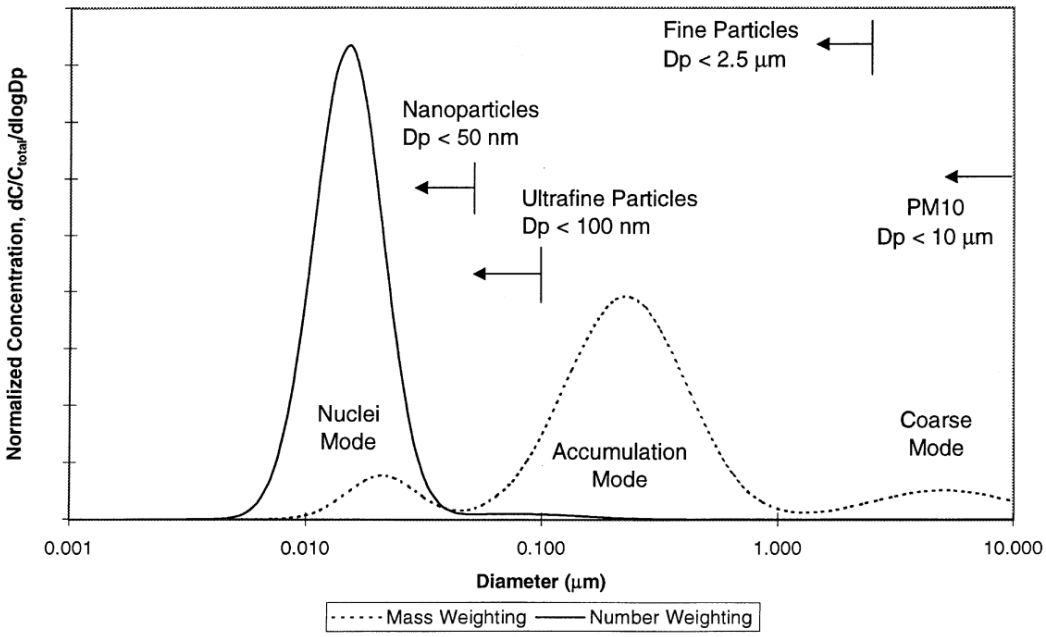

Figure 2-2 Size distribution of PM in terms of mass and number weighting [15]

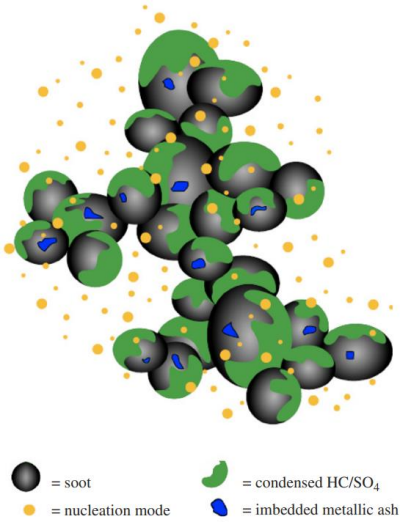

Figure 2-3 Deception of diesel particulate matter (PM) [16]

2.2 Particulate matter morphology and nanostructure

Understanding the morphology and nanostructure of aggregate particles has implications for understanding the mechanisms underlying soot formation and growth processes [17]. Various researchers have employed techniques such as scanning electron microscopy (SEM), transmission electron microscopy (TEM), and X-ray diffraction spectroscopy (XRD) to examine particulate matter. TEM images allow for the determination of the average primary particle diameter and offer insights into the carbon nanostructure by analyzing the fringes that correspond to carbon graphitic crystallites [18]. These fringes can be further analyzed for their length and interplanar spacing. Comparisons can be made with XRD analysis, which provides information regarding the graphitic structure of carbon in particulate matter [19]. Ishiguro et al., [20] initially identified two distinct components within a primary particle at the nano-scale level: an inner core and an outer shell. Subsequent investigations have provided further characterization of these inner core and outer shell structures. The inner core comprises numerous fine particles, featuring a nucleus enveloped by carbon layers with a turbostratic structure. Conversely, the outer shell consists of graphitic crystallites aligned parallel to the external surface of the particle [21].

Oo et al. [22] conducted an analysis of particulate matter (PM) emissions from the GDI engine, DDI engine, and carbon black for comparison purposes. The soot's elemental composition was assessed using EDS, while the morphology was examined through TEM. The nanostructure was characterized using TEM and XRD, and the oxidation kinetics were evaluated using thermogravimetric analysis (TGA). The EDS analysis revealed that the PM from all three sources consisted mainly of carbon and oxygen, with no detectable soluble fraction. Observations of the morphology of individual particles, as shown in **Figure 2-4**, indicated that carbon black exhibited the largest primary particles, followed by DDI PM and GDI PM. Fringe analysis of the nanostructure demonstrated that carbon black possessed the most graphitic characteristics, with shorter interlayer spacing and longer fringes, while GDI PM exhibited the least graphitic properties.

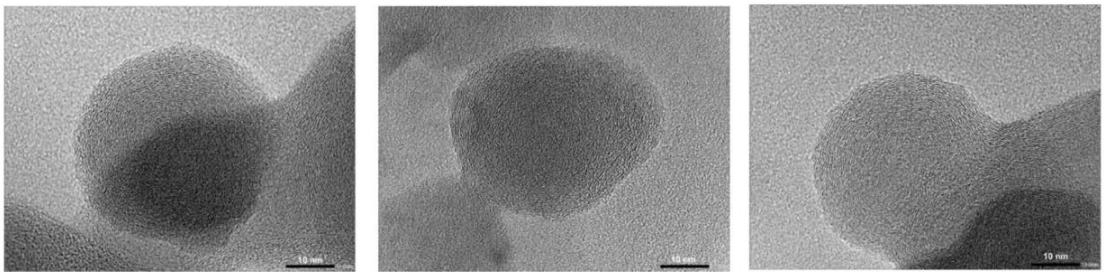

(a) (b) (c)

Figure 2-4 TEM images showing individual soot particles at the magnification of 800k: from (a) GDI engine, (b) DDI engine, and (c) carbon black [22]

Previous research on the impact of biodiesel on particulate matter (PM) emissions has reached a consensus that increasing the biodiesel content leads to a reduction in overall PM levels, primarily attributed to the higher oxygen content present [23] [24]. Verma et al [25] discovered that the presence of oxygen in biodiesel blends facilitates oxidation reactions, subsequently inhibiting the surface growth of soot particles. As a consequence, smaller primary particles of soot are formed. Additionally, the agglomerates of soot exhibit reduced sizes, corresponding to the smaller primary particles. The inclusion of oxygenated fuels was also found to yield shorter fringes and higher tortuosity.

2.3 Combustion and emission characteristics of renewable biofuels

In their study, Raman et al. [26] investigated the impact of rapeseed oil biodiesel on the performance, combustion characteristics, and emissions of a direct injection diesel engine operating at a constant speed of 1500 rpm under varying load conditions. The experiment involved blending different proportions of rapeseed oil biodiesel with diesel fuel, including blends of 25%, 50%, 75%, and 100% biodiesel. The findings indicated a slight reduction in brake thermal efficiency (BTE), with the lowest value observed for the B100 blend. This decrease was attributed to the lower calorific value of biodiesel blends, as well as the increased fuel flow rate resulting from higher blend percentages. The maximum cylinder pressure and heat release rate were lower for the biodiesel blends compared to pure diesel, mainly due to the rapeseed oil biodiesel's lower cetane number, higher viscosity, and density. The presence of oxygen in biodiesel resulted in lower carbon monoxide and unburned hydrocarbon emissions compared to pure diesel, indicating improved combustion processes.

However, an increase in the biodiesel blend percentage led to higher smoke density due to the heavier molecular structure, resulting in slower combustion and increased smoke emissions.

Baweja et al. [27] focused on exploring the utilization of mustard oil as a feedstock for biodiesel production through the transesterification process. Four different test fuels were prepared by blending mustard oil with diesel fuel at volumetric ratios of 10%, 20%, 30%, and 40%. The engine testing was conducted at a constant speed of 1500 rpm under various load conditions. The findings revealed that the B40 blend exhibited the highest cylinder pressure, which can be attributed to the increased proportion of biodiesel and its higher oxygen content. As a result, the cylinder pressure approached the level observed with pure diesel. However, the BTE was lower for B30 and B40 blends compared to B10 and B20 blends due to factors such as higher viscosity, lower calorific value, and poorer air-fuel mixing. Among all the blends, B20 demonstrated the lowest emissions of CO, NOx, and smoke opacity.

Karami et al. [28] conducted a study focusing on the utilization of tomato seeds oil (TSO) as an inexpensive and non-edible feedstock for biodiesel production. Engine testing was performed using pure diesel, B5, B10, and B20 blends at different engine loads and speeds. Additionally, the researchers developed an engine combustion model utilizing artificial neural networks (ANN) and computational fluid dynamics (CFD) within AVL FIRE software to predict combustion process parameters. The results indicated that the peak heat release rate (HRR) for B20 increased with engine speed, while for other fuels, it decreased. Furthermore, the B20 blend resulted in the minimum peak cylinder pressure as the cylinder pressure occurred at a greater distance from the top dead center (TDC) during the piston's expansion cycle. The ignition delay for B20 exhibited optimum conditions, leading to increased premixed combustion. Based on simulation results under standard conditions, the B10 blend demonstrated better performance and efficiency compared to other tested fuels.

Tripatara et al. [29] conducted a study in Thailand to explore the impact of palm oil biofuel on the combustion behavior and particle emissions in a single-cylinder compression ignition (CI) engine. The investigation compared three fuel blends: B7, B20, and B100, under varying engine load conditions of 20%, 50%, and 80% at 2400 rpm. Results showed that at high load conditions, B100 exhibited the highest fuel

consumption per unit of engine power. This outcome was attributed to factors such as the lowest heating value, shortest ignition delay, and highest indicated thermal efficiency associated with B100. Additionally, the smoke intensity decreased with an increase in the proportion of palm oil biofuel, which could be attributed to the higher oxygen content in the biofuel molecules. Furthermore, the study observed a gradual reduction in the agglomerated ultrafine particles of particulate matter (PM) from B7 to B100.

2.4 Exhaust after-treatment system

2.4.1 Diesel oxidation catalyst

As previously stated in the introduction, the more stringent regulations concerning exhaust emissions necessitate the incorporation of an exhaust after-treatment system alongside the engines. In the case of diesel engines or vehicles, this typically involves the utilization of a diesel oxidation catalyst (DOC), which employs specific material catalysts to facilitate the reduction and oxidation of carbon monoxide (CO) and hydrocarbon (HC) emissions. In the study conducted by V. Nadanakumar, S. Jenoris Muthiya, T. Prudhvi, and their colleagues [30], the researchers developed and constructed a diesel oxidation catalyst (DOC). The selection of materials for the wash coat included aluminum oxide, barium nitrate, orthophosphoric acid, and cerium, while manganese nitrate was chosen as the catalyst for coating the cerium beads. The experimental investigations were performed on a dm10 single-cylinder diesel engine, comparing the results obtained with and without the implementation of the DOC. The findings of the study demonstrated a reduction in CO and HC emissions upon the implementation of the DOC, which facilitated the conversion of water and carbon dioxide (CO_2). Additionally, the DOC effectively converted NOx emissions into nitrogen and oxygen, with a higher release of oxygen observed from the engine equipped with the DOC. Additionally, a minor decline in smoke emissions was observed.

In the study conducted by Liang et al. [31], they investigated the utilization of a ceria-modified monolithic platinum-based DOC with the objective of enhancing the generation of active oxygen species for effective NO oxidation. The results indicated that the maximum NO conversion achieved by the ceria-modified fresh DOC was approximately 60%, which represented a 10% improvement compared to the

unmodified counterpart. Additionally, the Ce sample exhibited a lower reaction temperature of 30% NO conversion, reduced by 12°C. The interaction between ceria and platinum facilitated the Ce^{3+}-Ce^{4+} cycle under the reaction atmosphere, promoting the production of active oxygen species and metallic platinum. As a result, a significant enhancement in the NO conversion performance was observed.

In the scholarly work conducted by Liu et al. [32], a comprehensive overview was presented regarding the advancements in ceria-based catalysts for soot oxidation, spanning across various catalyst types. Notably, researchers have made progress in developing ceria catalysts with diverse morphologies, such as nanoscale fibers and exposed lattice planes, aiming to enhance their surface area and mobility. Two primary mechanisms have been identified for ceria catalysts: the "active oxygen-assisted mechanism," where ceria facilitates the generation of highly reactive oxygen species for effective soot oxidation, and the "NO_2-assisted mechanism," where ceria oxidizes nitrogen monoxide (NO) into nitrogen dioxide (NO_2) to indirectly promote soot oxidation. Despite the generally stable nature of ceria catalysts, they exhibit poor thermal stability and are prone to thermal aging. Consequently, the inclusion of additives becomes necessary to enhance their durability. Moreover, ceria is susceptible to sulfur poisoning due to its alkaline properties, and this challenge can be mitigated by introducing noble metals, acidic species, or sacrificial alkaline additives.

2.4.2 Full-flow diesel particulate filter

In order to achieve further reduction and containment of particulate matter (PM), the utilization of diesel particulate filters (DPFs) has become increasingly prevalent. Typically, full-flow DPFs are composed of ceramic materials and possess a porous microstructure embedded within a honeycomb-like macrostructure. In their study, Khair and colleagues [33] conducted a comprehensive review of advancements in DPF technology and discussed potential future directions and developments required to enhance the performance of DPFs for diesel engines and vehicles. **Figure 2-5** provides a schematic representation of a wall flow DPF. Regardless of the specific design, DPFs have consistently demonstrated high trapping efficiencies, surpassing 90%. However, as PM accumulates and becomes trapped within the filter, it results in a gradual restriction of the exhaust flow, leading to increased pressure in the exhaust

pipe, which is known as back pressure. Consequently, a greater amount of work is required to overcome this elevated pressure. To alleviate the backpressure and enable the filter to effectively capture more PM, an external energy source, such as a burner, is employed to oxidize the trapped PM. Additionally, a control system is necessary to regulate both the external energy input and the resulting backpressure [34]. In modern vehicles, a combination of catalysts and filters is employed to minimize the energy required for the regeneration process. However, it should be noted that catalyst based DPFs still necessitate additional heat to successfully undergo regeneration across all operational conditions [33].

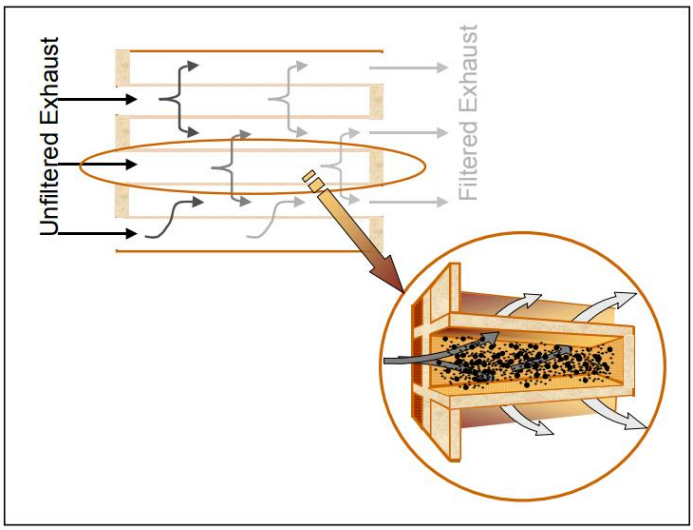

Figure 2-5 Schematic diagram of Wall flow diesel particulate filter [33]

2.4.3 Partial-flow diesel particulate filter

When utilizing wall-flow diesel particulate filters (DPFs) in diesel engines, several technical hurdles arise. One of these challenges involves the implementation of intricate engine calibration strategies, including the use of an external burner and a control system, to facilitate the oxidation of accumulated particulate matter and prevent excessive pressure buildup in the filter, which could result in increased fuel consumption. In contrast, partial-flow diesel particulate filters (P-DPFs) present a distinct advantage in this regard, as they do not necessitate the use of external energy input. The P-DPF is designed with a cylindrical or elliptical honeycomb structure comprising channels created by combining flat and corrugated layers [35]. It encompasses two key elements: a metal fleece composed of finely sintered metal wires, which possesses a specific porosity and facilitates controlled flow characteristics,

and a corrugated foil that redirects the gas flow toward the sinter fleece layers, enabling exchange between the layers and channels. **Figure 2-6** depicts an illustrative example of a metallic P-DPF, consisting of a gas flow layer and a microfiber fleece. Based on its design, the partial-flow diesel particulate filter (P-DPF) exhibits a comparable trapping efficiency to that of full-flow DPFs, reaching approximately 50%. However, due to its simpler design and absence of a control system, the P-DPF has gained popularity as a crucial initial measure for reducing particle emissions, particularly when employed as a retrofit exhaust after-treatment system.

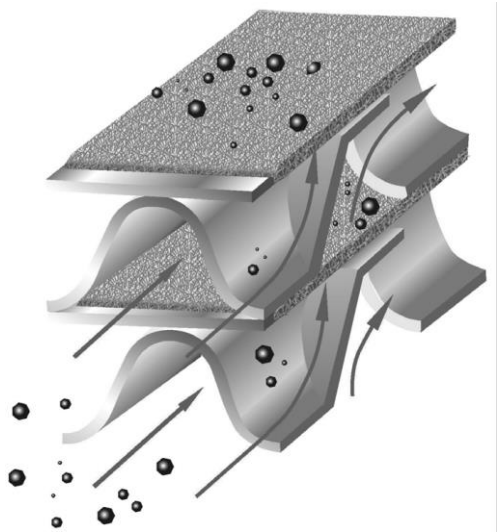

Figure 2-6 Layout of partial-flow DPF [35]

CHAPTER 3

RESEARCH METHODOLOGY

The aim of this research is to investigate and evaluate the consequences of retrofitting a partial flow diesel particulate filter (P-DPF) and a diesel oxidation catalyst (DOC) on both a diesel engine and a diesel vehicle. The experimental P-DPF retrofit system under investigation comprises a non-catalyzed P-DPF and a ceria-coated P-DPF. Additionally, the diesel oxidation catalyst implemented in this study is based on the ceria catalyst technology. The current investigation of the diesel engine focuses on analyzing the combustion characteristics, performance metrics, and emissions profiles under diverse operational conditions. The engine is subjected to varying levels of torque output, 56, 84, 112, and 140 Nm at fixed engine speeds of 1000, 1500, and 2000 rpm with measurements taken accordingly. The flow chart of the methodology overview is provided in **Figure 3-1**.

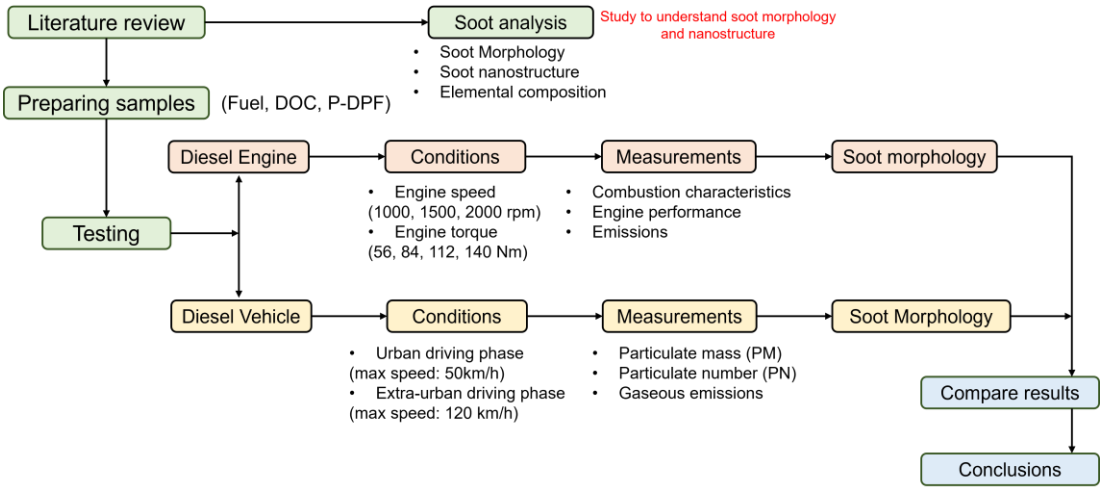

Figure 3-1 Flow chart of the methodology overview

3.1 Properties of biodiesel sample

The commercial biodiesel fuel utilized is composed of 20% pure biofuel blended with conventional diesel fuel. Biofuel is derived from palm oil by acid-esterification and transesterification with methanol. The properties of the B20 blend are comprehensively presented in **Table 3.1** with all properties assessed in accordance with the ASTM standards. The emissions of smoke during the pyrolysis combustion process may be decreased by increasing the proportion of pure biofuel in the blend

since pure biofuel has a lower ratio of carbon to hydrogen and a higher oxygen content than traditional diesel fuel [36].

3.2 Diesel Engine Experimentation

3.2.1 Technical Specifications of the Engine

In this experimental investigation, the ISUZU 4JJ1 TC internal combustion engine was employed as the subject of analysis. A visual depiction of the diesel engine experiment platform is presented in **Figure 3-2** for reference and the technical specifications of this engine are provided in **Table 3.2**. The engine's performance characteristics, including power, torque, and engine speed are graphically represented in **Figure 3-3**. The engine is an in-line four-cylinder direct diesel injection model with a three-litre total displacement. Its maximum power is 107 kW at 3600 rpm, and its maximum torque is 294 Nm between 1400 and 3400 rpm. In addition, the installation of the common rail injection system serves to provide enhanced injection pressure, with precise control of both injection timing and pressure facilitated by the engine control unit (ECU). Consequently, it is feasible to vary the injection parameters in accordance with the engine's speed and torque variations. The emissions of NO_x will be reduced with the installation of the Exhaust Gas Recirculation (EGR) system. However, it could also decrease the engine output power by reducing the maximum temperature within the engine cycle. To counteract this, the turbocharger was utilized to increase intake air pressure and consequently, recovered the engine output power.

Table 3-1 Properties of Biodiesel Sample (B20)

Fuel Properties	Standard	B20
Calorific Value (MJ/kg)	ASTM D 240	44.95
Viscosity @ 40°C (mm^2/s)	ASTM D 445	3.1
Density @ 15°C (kg/m^3)	ASTM D 1298	827
Distillation (°C)	ASTM D 86-11b	
T10		177.4
T90		348.4
Carbon (% mass)	ASTM D 5291	82.61
Hydrogen (% mass)	ASTM D 5291	13.45
Oxygen (% mass)	ASTM D 5291	3.94

Figure 3-2 ISUZU 4JJ-TC Direct injection diesel engine

Table 3-2 Technical specifications of the engine

Items	Details
Engine Model	ISUZU 4JJ1 TC
Engine type	Diesel, four-stroke
Cylinder layout and number	In-line, four-cylinder
Bore x Stroke (mm)	95.4 x 104.9
Compression ratio	18.3 : 1
Total Displacement (cc)	3000
Maximum power output	107 kW @ 3600 rpm
Maximum torque output	294 Nm @ 1400-3400 rpm
Injection System	Common rail
Addition devices	EGR, Turbocharger

3.2.2 Specifications of Eddy current dynamometer

The experimental setup involves the connection of an eddy current dynamometer to the engine flywheel to impose a load on the engine. A rotator shaft is employed to transfer power from the engine to the dynamometer, which is encompassed by a stator coil that provides mechanical friction. As the rotator rotates within the electromagnetic field of the stator coil, it generates eddy currents that flow through the short circuit surrounding the stator coil, dissipating into the heat. This heat is then conveyed to an external cooling system. Additionally, the load cell measures

the produced current, which is subsequently converted into torque. The particulars of the eddy current dynamometer that was utilized in this experiment are comprehensively provided in **Table 3.3** and a depiction of the physical arrangement of the eddy current dynamometer on the experimental test platform is presented in **Figure 3-3**.

Table 3-3 Specifications of Eddy current dynamometer

Items	Details
Model	Tokyo Plant ED-150-LC
Maximum Brake Torque	35.81 kgm
Maximum Brake Horsepower	150 PS/ 3000 rpm
Maximum Speed	3000 rpm

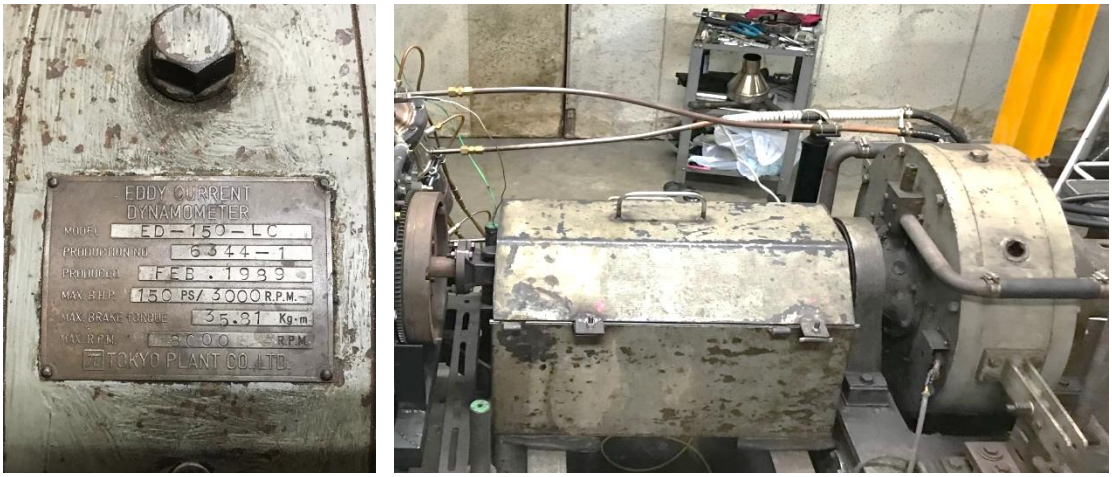

Figure 3-3 Tokyo Plant eddy current dynamometer

3.3 Diesel Vehicle Experimentation

A light-duty vehicle equipped with a 2.5-liter 4-cylinder common rail direct diesel injection engine was utilized to examine the impact and consequences of retrofitting a partial flow diesel particulate filter (P-DPF) on a commercial diesel vehicle during urban and extra-urban driving conditions. The specifications of the light-duty vehicle utilized in the experiment and the depiction of the vehicle mounted on the chassis dynamometer are provided in **Table 3.4** and **Figure 3-4**, respectively. The experimental conditions of this study were scrutinized at the Automotive Emissions Laboratory (AEL), which was founded according to the International Organization for Standardization 17025 (ISO/IEC 17025) with the aim to evaluate the quality systems of testing laboratories. All the equipment used in the AEL test conforms to European

Emissions Standards 4. This study used a driving cycle in compliance with the New European Driving Cycle that includes both urban driving with an optimal speed of 50 km/h and extra-urban driving with a peak speed of 120 km/h, as depicted in **Table 3.5** and **Figure 3-5**

Table 3-4 Specifications of Light-duty Vehicle

Items	Detail
Engine type	2KD-FTV (diesel), 4-cylinder, in-line
Vehicle mass	1590 kg
Displacement volume	2,500 cc
Compression ratio	18.5:1
Bore x Stroke	92 mm x 93.8 mm
Maximum Power	75 kW @ 3600 rpm
Maximum Torque	260 Nm @ 1600-2400 rpm
Valve mechanism	16 valve DOHC
Fuel System	Common rail, Direct injection

Figure 3-4 On-road performance evaluation of light-duty diesel vehicle

Table 3-5 The New European Driving Cycle

Characteristics	Urban Driving	Extra-urban Driving
Distance (km)	4	7
Duration (s)	780	400
Maximum Speed (km/h)	50	120

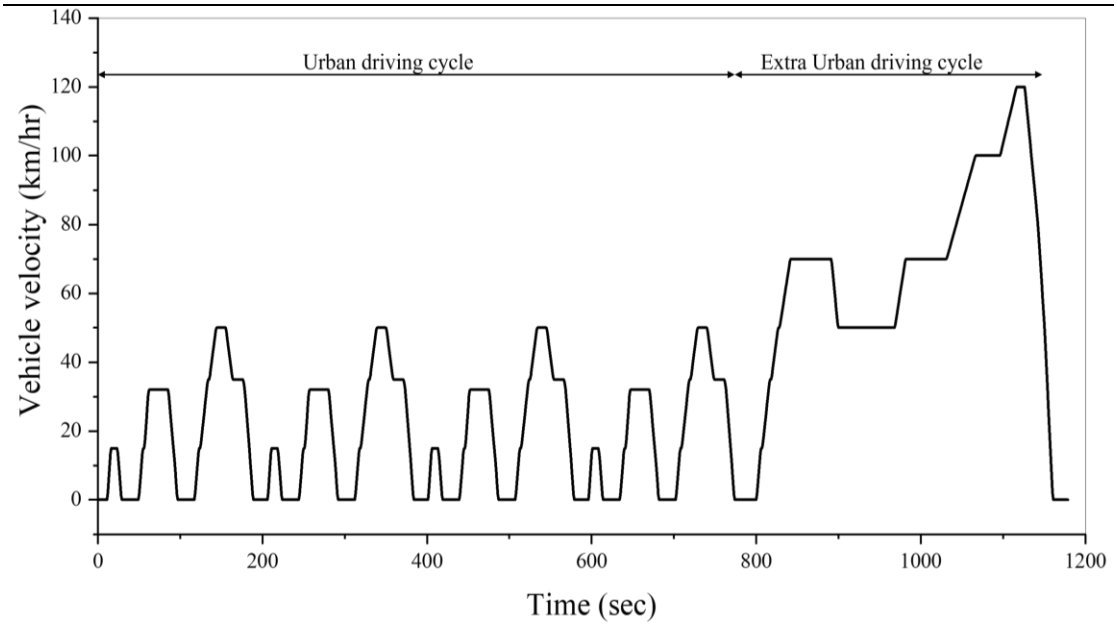

Figure 3-5 New European Driving Cycle

3.4 Data Acquisition Infrastructure

3.4.1 Pressure Sensor and Crank Angle Encoder

To facilitate the observation of the phenomenon occurring within the tested engine, a high thermal resistance piezoelectric crystal sensor, the Kistler 6052C31, is employed to measure the pressure within the combustion chamber and this sensor is meticulously mounted on cylinder number one. **Figure 3-6** shows how the pressure sensor was installed on the engine under test. This sensor can detect pressures up to 250 bars with a precision of 0.7 bar and a high degree of sensitivity. In order to capture the actual position of the crank angle, an optical crank angle encoder known as "CA-RIE-720" is mounted at the extremity of the dynamometer shaft. It is a specialized disc with 720 slits, offering a resolution of 0.5 degrees, and the mechanism operates based on the principle of transmitting light, where an infrared beam is emitted and subsequently detected by the sensor, as depicted in **Figure 3-7**.

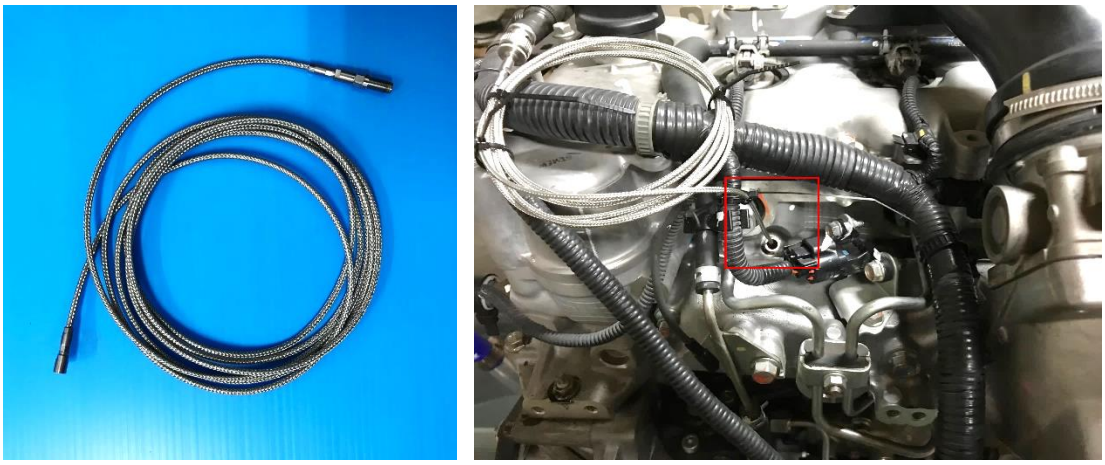

Figure 3-6 Piezoelectric Pressure Sensor

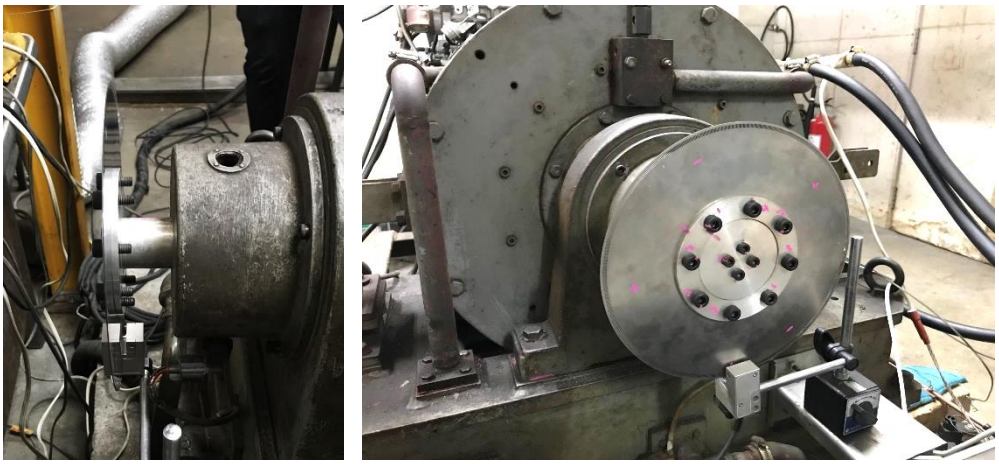

Figure 3-7 Crank angle encoder positioned at the end of dynamometer shaft

3.4.2 Collection of emissions data in diesel engine test

The quantity of particle exhaust emissions was assessed using a smoke intensity meter that leverages the reflection of light to optically measure the particulate matter (PM) deposited on a paper filter. It measured the concentration of PM both before and after being deposited on the paper filter. The intensity of smoke is expressed as a percentage, with 0% indicating the absence of PM on the paper filter and 100% signifying completer coverage of the filter. **Figure 3-8** illustrates the "Okuda DSM – 240" smoke intensity meter and the PM trapped on the paper filter. In addition, the study also utilized an exhaust gas analyzer, the "AVL DITEST GAS 1000", to evaluate the emissions of various other exhaust gases as provided in **Figure 3-9**.

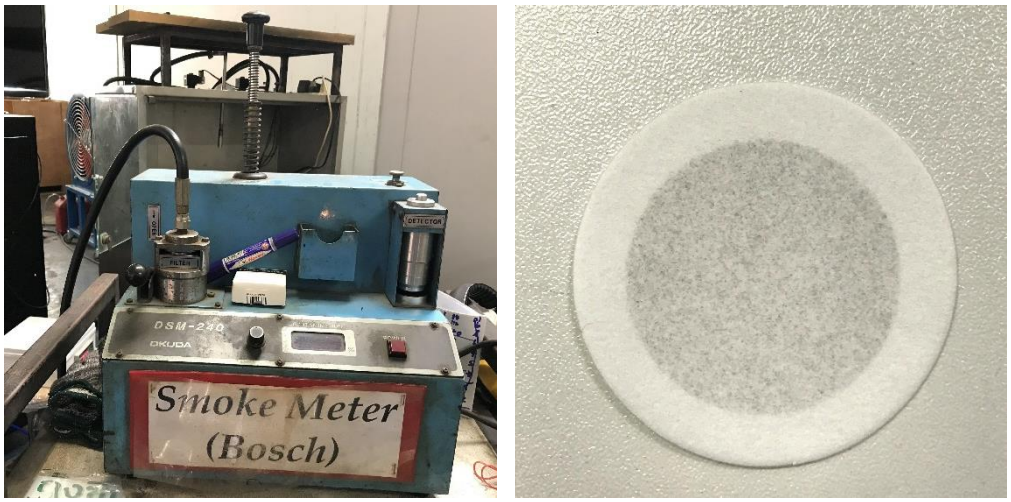

Figure 3-8 Smoke intensity meter and PM deposited on the paper filter

Figure 3-9 AVL exhaust gas analyzer

3.4.3 Collection of emissions data in diesel vehicle test

Emissions generated by the light-duty vehicle, including carbon dioxide (CO_2), nitrogen oxides (NO_x), total hydrocarbon (THC), and carbon monoxide (CO) are conveyed to a remote mixing unit where they are blended with air within the dilution tunnel. The resulting exhaust gases are directed to a constant volume sampler (CVS), an exhaust gas sampling system, and a gas analyzer equipped with a dilute measurement system. In order to maintain the physical and chemical characteristics of the emissions, the CVS system is designed to fix a constant dilution ratio, temperature, and moisture content. Measurements of the paper filter's weight before and after particle collection are used to determine the mass of particulate matter (PM), and the AVL particle counting equipment is used to determine the particulate number (PN).

3.4.4 Apparatus for data recording

In order to observe and record the combustion characteristics taking place within the combustion chamber, the Dewesoft “SIRIUS-HS” data acquisition system, shown in **Figure 3-10**, is utilized to store real-time crank angle and pressure data. A total of 1000 cycles of data collection from the system are recorded during which the engine is maintained in a stable operating condition for each specified engine condition. The collected data is then transferred to a computer for further analysis in the crank angle domain using the integrated Dewesoft software. This analysis enables the calculation of combustion parameters such as pressure versus crank angle and pressure versus volume, as depicted in **Figure 3-11**.

Figure 3-10 Dewesoft Data Acquisition System

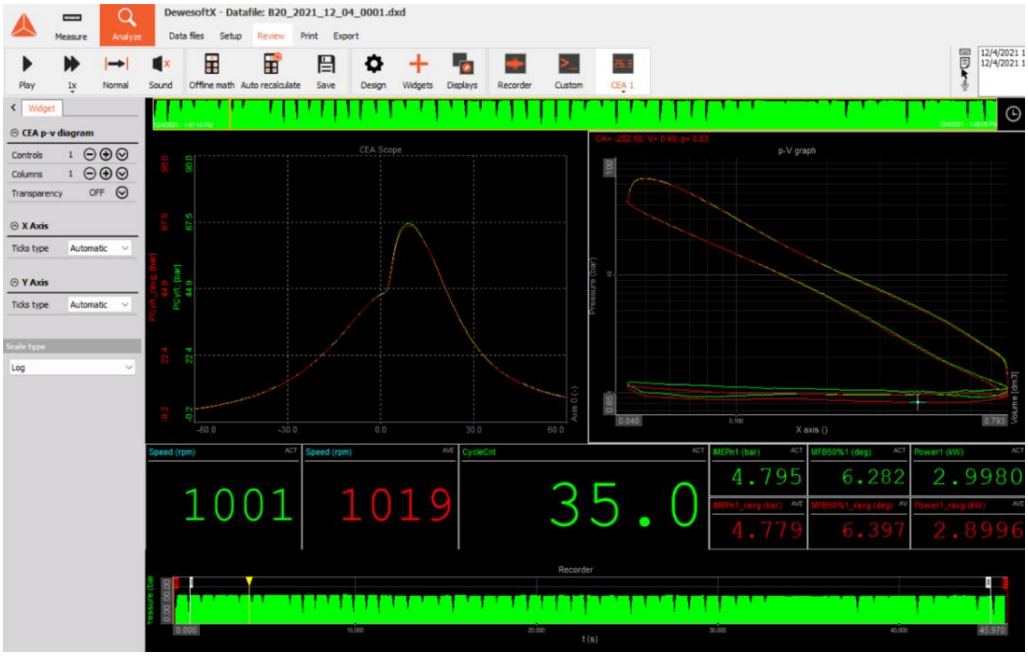

Figure 3-11 Data monitoring in Dewesoft software

3.5 After-treatment System for Exhaust Emissions

In order to mitigate the emissions of harmful gases from diesel vehicles and engines, the application of diesel oxidation catalyst (DOC) and partial flow diesel particulate filter (P-DPF) have been implemented. Typically, the DOC is installed upstream of the P-DPF and the specifications are predetermined as they were not developed in-house. This is useful because the goal of this research is to assess the impact rather than to develop a unique DOC and P-DPF system. The specifications of DOC and P-DPF are provided in **Table 3.6** and **Figure 3-12**.

Table 3-6 Specifications of DOC and P-DPF

Type	Element	Cell Density (cpsi)	Diameter (mm)	Length (mm)
DOC	CeO_2	300	144	80
P-DPF	Non-catalyst	300	144	150
	CeO_2	300	144	150

(a) (b)

Figure 3-12 (a) Diesel oxidation catalyst and (b) Partial-flow diesel particulate filter

The installation of DOC and P-DPF in the diesel engine and the vehicle is presented in **Figure 3-13**. The DOC is intended to chemically treat the exhaust gas by oxidizing carbon monoxide (CO), hydrocarbons (HCs), and volatile compounds that are present in the exhaust gas. Additionally, including a ceria catalyst leads to the oxidation of nitrogen oxide (NO) to nitrogen dioxide (NO2), elevating the NO_2/NO_x ratio in the exhaust. When the temperature of the exhaust gas exceeds 250°C, the resulting NO_2 can be utilized for the oxidation of particulate matter (PM) that is captured by the partial flow diesel particulate filter (P-DPF) downstream of the DOC [37].

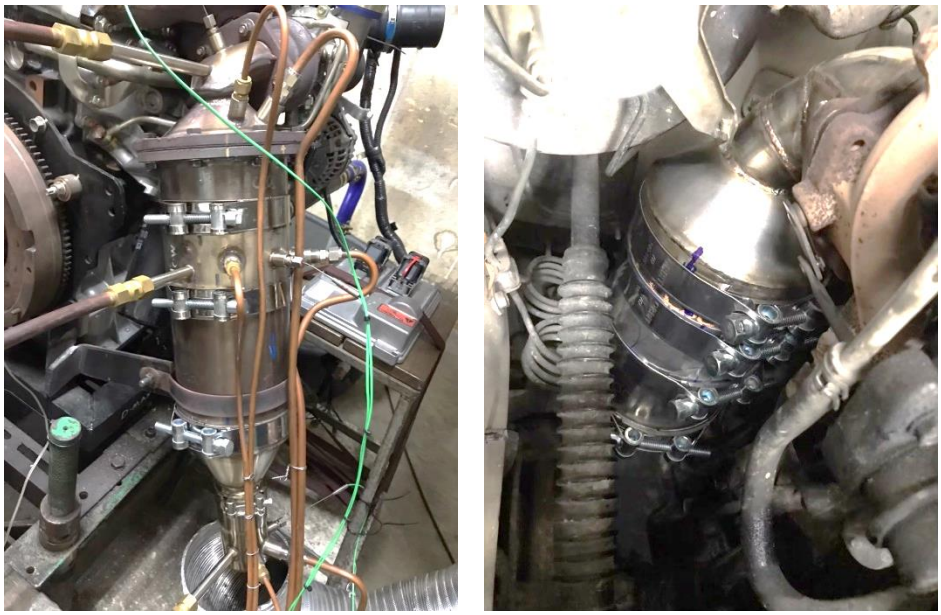

(a) (b)

Figure 3-13 Installation of the exhaust after-treatment system at (a) the diesel engine and (b) the light-duty vehicle

The design of the partial-flow diesel particulate filter employed in this study was analogous to that found in prior literature [38]. This P-DPF utilized in the study was composed of layers of metal flow guide foil and microfiber fleece. **Figure 3-14** illustrates the working principle of the P-DPF design, while **Figure 3-15** shows the cross-sectional cut of the P-DPF with the different layers that constitute the partial filter. The microfiber fleece is directed toward the filter layer meaning the specific trapping efficiency is very low. Despite the limitations, the trapping efficiency of the partial-flow diesel particulate filter is at an acceptable level. This has led to its adoption as a retrofit option for heavy-duty vehicles and gasoline direct injection (GDI) systems due to the filter's high number of layers and length [39].

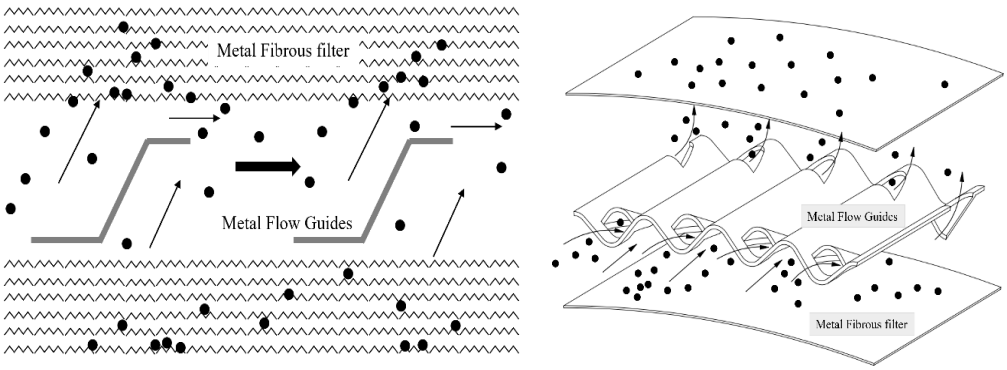

Figure 3-14 Working Principle of partial-flow diesel particulate filter (P-DPF)

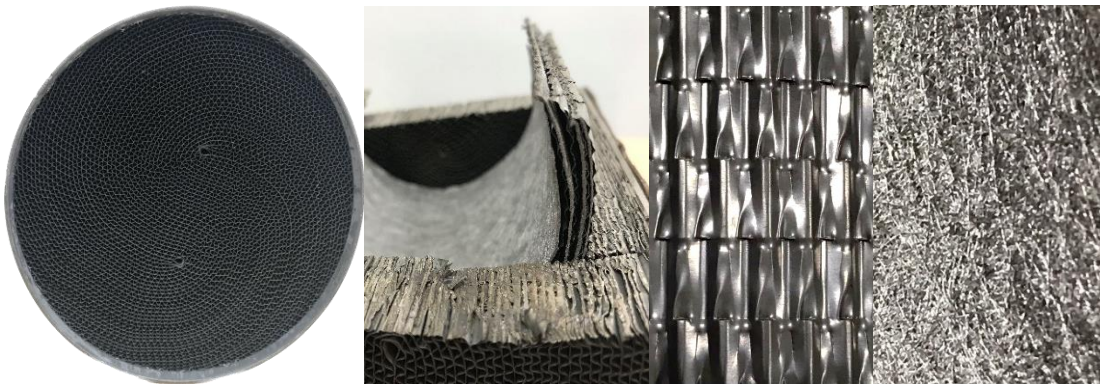

(a) (b) (c) (d)

Figure 3-15 Close-up view of (a) P-DPF showing (b) the cross-sectional cut made up of metal (c) fleece and (d) fiber

3.6 Schematic diagram

3.6.1 Experimental Setup of the diesel engine test

The schematic depiction of the experimental setup for diesel engine testing using an eddy current dynamometer is presented in **Figure 3-16**. The dynamometer is integrated with the dynamometer controller to impose load or torque on the engine. The engine was subjected to four fixed loads (56, 84, 112, and 140 Nm) at 1000 rpm (idle low speed), 1500 rpm (mid-engine speed), and 2000 rpm (the engine speed corresponding to the maximum torque). The experimental procedure involves conducted in two stages, first without the installation of the DOC and P-DPF, and subsequently after the installation of these components. The engine was operated by manipulating the accelerator pedal to attain the desired engine speed, while the fuel flow rate was determined by a weight scale during the experimental process. Furthermore, the engine control unit (ECU) was linked with an onboard diagnosis (OBD) tool, namely the Carman scan, to track and assess the status of the engine, including parameters like throttle position, oil temperature, and coolant temperature. To conduct combustion analysis, the pressure sensor was positioned on the first cylinder while the crank angle encoder was affixed to the output shaft of the dynamometer. These two sensors were then interfaced with the Dewesoft data acquisition system which served to capture and transmit the data obtained from the sensors to a computer 1 for subsequent analysis. In order to analyze emissions, the smoke intensity was measured three times per test condition by the BOSCH smoke intensity meter, and the engine exhaust gases were monitored using the AVL gas analyzer, recording data for one minute per test condition.

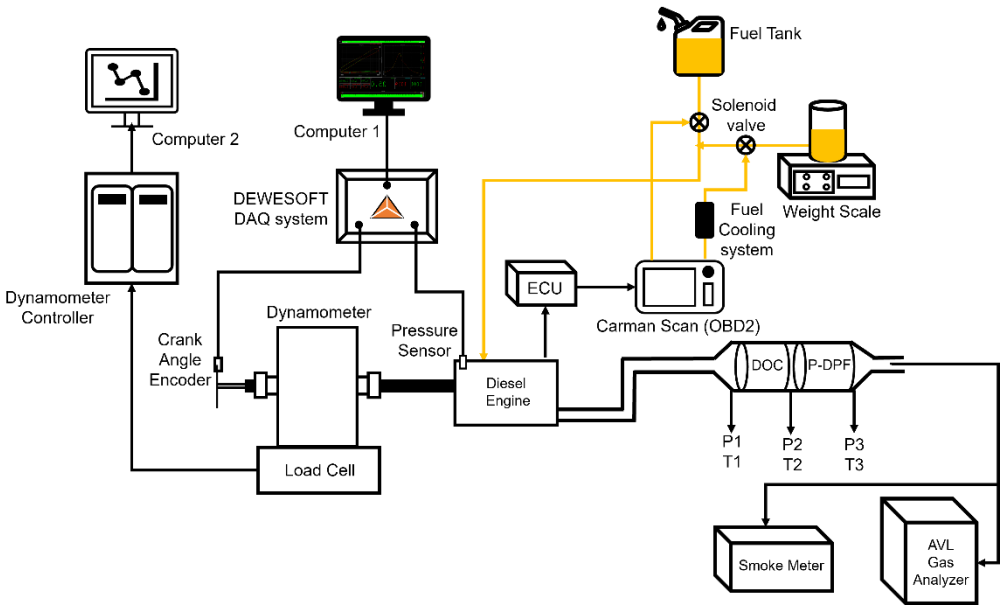

Figure 3-16 Schematic representation of the engine testbed

3.6.2 Experimental Setup of the diesel vehicle test

The diagram in **Figure 3-17** illustrates the layout of the diesel vehicle test conducted on the chassis dynamometer. Initially, the light-duty vehicle was positioned on the chassis dynamometer consisting of rollers and a cooling fan that supplies variable air velocity synchronized with the roller speed. The carbon balance method was used to estimate the fuel economy under investigation. The quantity of particulate matter (PM), the number of particulates (PN), and gaseous emissions in the exhaust were determined using the weight scale, the AVL particle counter, and the AVL gas analyser, respectively.

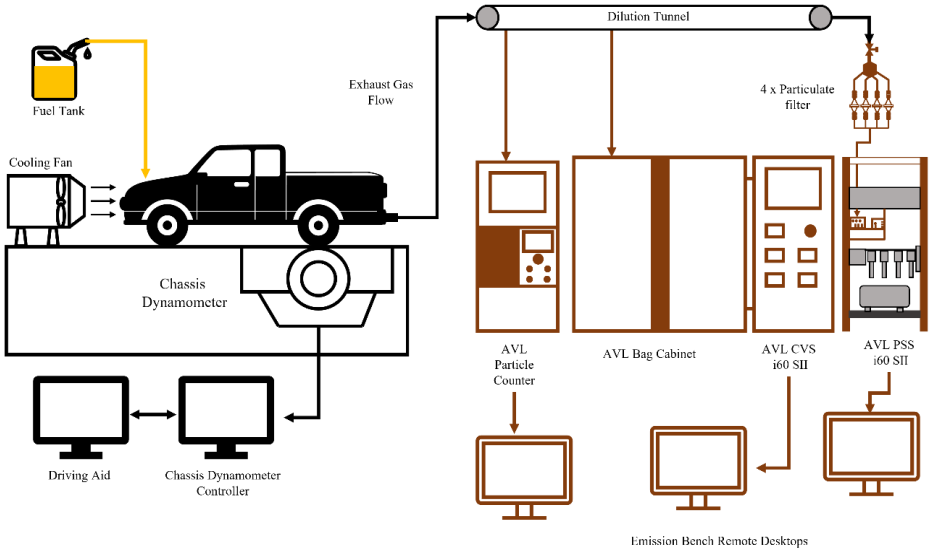

Figure 3-17 Schematic representation of diesel vehicle test on the chassis dynamometer

3.7 Research computational procedure

3.7.1 Combustion Characteristics

At stable operating conditions, the pressure sensor and crank angle encoder data were stored in the data acquisition system for 1000 engine cycles. However, due to inconsistencies caused by the engine vibration and other interference sources during these 1000 cycles, 200 representative cycles were selected and averaged to reduce the effect of noise. The averaged raw pressure data were then smoothed using a third-order least square with seven points method, as presented in **Equation 3.1** [40].

$$P_{\theta(smooth)} = \frac{[-2(P_{\theta-3}+P_{\theta+3})+3(P_{\theta-2}+P_{\theta+2})+6(P_{\theta-1}+P_{\theta+1})+7(P_{\theta})]}{21} \quad \textbf{3.1}$$

Where, p = pressure data in bar unit and θ = crank angle in degree unit

The distinction of combustion characteristics is facilitated by essential parameters such as the net heat release rate (NHRR) and cumulative net heat release (CNHR). In order to determine the net heat release rate (NHRR), smoothed pressure data, cranked angle, and the combustion chamber volume were used and the calculation was performed using the first law of thermodynamics, as described in **Equation 3.2** according to J.B.Heywood [41]. The NHRR serves as an indicator of the influence of the fuel injection system, as well as the premixed and diffused combustion modes on the combustion process. The cumulative net heat release (CNHR) was obtained by integrating the NHRR throughout the entire combustion process.

$$\frac{dQ}{d\theta}\left[NHRR\right] = \left[\frac{k}{k-1}\right].P.\frac{dV}{d\theta} + \left[\frac{1}{k-1}\right].V.\frac{dP}{d\theta} \quad \textbf{3.2}$$

Where: $\frac{dQ}{d\theta}\left[NHRR\right]$ = net heat release rate (J/deg)

k = ratio of specific heat (c_p/c_v)

P = pressure (Pa), V =volume (m^3)

$\frac{dV}{d\theta}$ = variation in cylinder volume as a function of crank angle (m^3/deg)

$\frac{dP}{d\theta}$ = variation in cylinder pressure as a function of crank angle (Pa/deg)

3.7.2 Engine performance

The specific fuel consumption, specific energy consumption, and thermal efficiency in both indicated and brake values are key parameters for evaluating engine

performance. The specific fuel consumption (SFC), which is determined as the ratio of fuel consumption to engine output and is frequently represented in kilograms of fuel per kilowatt-hour (kg/kWh), is a statistic used to quantify the fuel usage efficiency of an engine. Specific energy consumption (SEC) refers to the energy demand for generating a unit of engine power and is typically quantified in kilojoules per kilowatt-hour (kJ/kWh). How well a diesel engine transforms the chemical energy in the fuel into usable work is determined by its thermal efficiency, which is defined as the ratio of net work output to heat input from the fuel. All these calcuations are provided as follow, **Equation 3.3, 3.4, 3.5, 3.6, 3.7** and **3.8**.

$$\text{Indicated specific fuel consumption (ISFC)} = \frac{\text{Fuel consumpiton rate}}{\text{indicated power}} = \frac{\dot{m}_f}{PdV} \quad \textbf{3.3}$$

$$\text{brake specific fuel consumption (BSFC)} = \frac{\text{Fuel consumpiton rate}}{\text{brake power}} = \frac{\dot{m}_f}{4\pi T.\frac{N}{60}.1/2} \quad \textbf{3.4}$$

$$\text{indicated specific energy consumption (ISEC)} = ISFC \,.\, LHV \quad \textbf{3.5}$$

$$\text{brake specific energy consumption (BSEC)} = BSFC \,.\, LHV \quad \textbf{3.6}$$

$$\text{indicated thermal efficiency (ITE)} = \frac{\text{indicated power}}{\text{energy input}} = \frac{\dot{W}_i}{\dot{Q}_{in}} \quad \textbf{3.7}$$

$$\text{brake thermal efficiency (BTE)} = \frac{\text{brake power}}{\text{energy input}} = \frac{\dot{W}_b}{\dot{Q}_{in}} \quad \textbf{3.8}$$

Where, $\dot{m}_f$ = fuel consumption (g/s) , T = torque (Nm), N = engine speed (rpm), LHV = low heating value of fuel (kJ).

3.7.3 Diesel vehicle test

Real-time measurements of gaseous emissions are recorded in parts per million (ppm) and will be converted into milligrams per kilometer (mg/km) using **Equation 3.9**.

$$M_i = \frac{V_{mix}.Q_i.k_b.C_i.10^{-6}}{d} \quad \textbf{3.9}$$

Where:

M_i = mass emissions of the pollutant (i) in grams per kilometer

V_{mix}= volume of the diluted exhaust gas expressed in liters per test and corrected to standard conditions (273.2 K and 101.33 kPa), 129.05 for UDC and 66.01 for EUDC

Q_i= density of the pollutant i in grams per liter at normal temperature and pressure (273.2 K and 101.33 kPa)

Q_{CO} = 1.25, Q_{HC} = 0.619, Q_{NOx} = 2.05, Q_{CO2} = 1.94

k_b = humidity correction factor used for the calculation of the mass emissions of nitrogen oxides, 0.9 for UDC and 0.92 for EUDC

C_i = concentration of the pollutant (i) in the diluted exhaust gas expressed in ppm

d = distance corresponding to the operating cycles in kilometers, 4.09 for UDC and 6.98 for EUDC

Real-time measurements of particulate number are reported in units of #/cm³, which is determined based on the bag size. These measurements will be subsequently converted to #/km using **Equation 3.10**.

$$N = \frac{V.k.\overline{C_s}.\overline{f_r}.10^3}{d} \qquad \textbf{3.10}$$

Where:

N = particle number emissions expressed in particles per kilometer

V = volume of the diluted exhaust gas expressed in liters per test and corrected to standard conditions (273.2 K and 101.33 kPa), 129.05 for UDC and 66.01 for EUDC

K = calibration factor to correct the particle number counter measurements to the level of the reference instrument where is not applied internally within particle number counter. Where the calibration factor is applied internally within the particle number counter a value of 1 shall be used for k in the above equation

$\overline{C_s}$ = corrected concentration of particles from the diluted exhaust gas expressed as the average particles per cubic centimeter figure from the emissions test including the full duration of the drive cycle

$\overline{f_r}$ = mean particle concentration reduction factor of the volatile particle remover at the dilution setting used for the test which is 2000 for the above equation

3.8 Soot Morphology analysis

3.8.1 Scanning electron microscope (SEM)

The microstructural features of the deposited soot on the paper filter were evaluated using a scanning electron microscope (SEM-SU5000) illustrated in **Figure 3-18**. SEM operates by scanning a sample's surface with a highly focused electron beam to generate high-resolution images. The interaction between the sample's atoms and the electrons can be detected and utilized to produced an image.

Figure 3-18 Scanning electron microscope employed in this study

3.8.2 Transmission Electron microscope (TEM)

The morphology and nanostructure of the particulate matter were investigated at magnifications of 80k and 800k, respectively, using a transmission electron microscope (JEM-2100 Plus), as depicted in **Figure 3-19**. By measuring the diameters of the individual primary particles and then putting them into a size distribution histogram graph, an image processing program (ImageJ) was used to objectively assess the morphology and nanostructure. An example of such primary particle measurement is presented in **Figure 3-20**. The analysis of the nanostructure involved the conversion of the cross-sectional graphene sheets into single-pixel-wide lines to enable quantitative analysis. To this end, a single primary particle image at the 800k magnification was cropped into a 10nmx10nm square. Subsequently, the square image was transformed into grayscale, polarized into black and white, and rid of chaotic lines before being skeletonized into single pixel wide lines. These lines are then investigated automatically using a plug-in software in ImageJ to determine the finge lengths. The visualized image of each step is provided in **Figure 3-21**. The crystallite length, La, would be compared to the maximum fringe length as done in literature [22].

Figure 3-19 Transmission electron microscope employed in this study

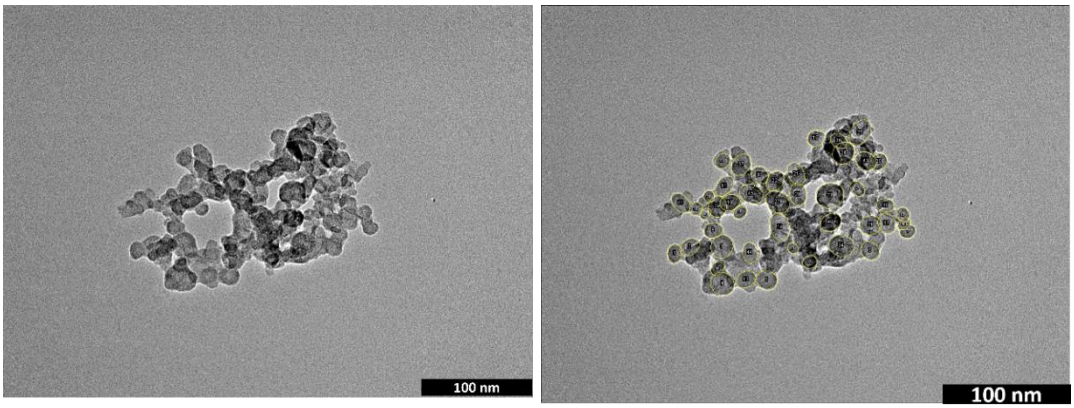

Figure 3-20 Example of individual particle size measurement

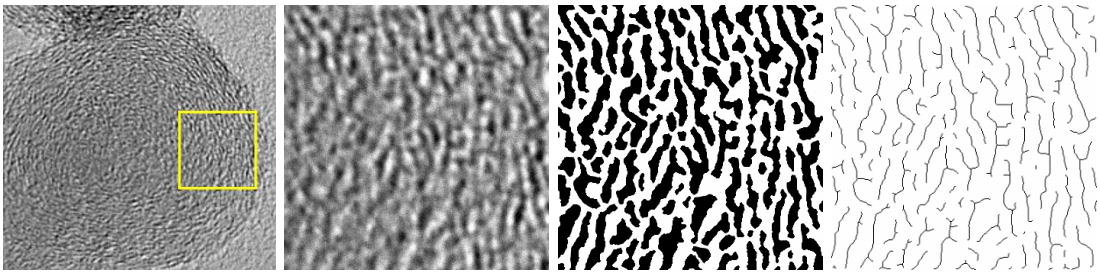

(a) (b) (c) (d)

Figure 3-21 Image processing steps of (a) selection of 10nmx10nm area, (b) cropping, (c) polarizing into black and white, and (d) skeletonizing

3.8.3 X-ray diffraction method

In this study, X-ray diffraction analysis was performed using a Bruker D8 Advance X-ray powder diffractometer that utilized a CuKα radiation source as presented in Figure 3-21. The scanning angle range was $10° < 2\theta < 90°$. Then, the analysis was processed by using Bragg's law and Scherrer's formulae.

Interplaner spacing, $d_{002} = \frac{\lambda}{2 \sin \theta_{002}}$ **3.9**

Number of stacking of graphene layer, $N = \frac{L_c}{d_{002}}$ **3.10**

Crystallite length, $L_a = \frac{1.84\lambda}{\beta_{100} \cos \theta_{100}}$ **3.11**

Where, λ = the x-ray wavelength (0.15406 nm), β = the full-width-at-half-maximum of the respective planes, and θ = the angle at which the respective plane is centred at.

These three equations facilitated a comparison between the X-ray diffractio (XRD) and TEM analyses by providing data on the crystallite length, interplanar spacing, and stacking number. In XRD raw data curve, there were two plane peaks, namely 002 and 100 peaks. The 002 peak was associated with the degree of graphitization or orientation of the carbonaceous aromatic layers whereas the 100 peak was associated with the degree of condensation or size of the aromatic layer [42]. The XRD equipment used in this study is shown in **Figure 3-22**.

Figure 3-22 X-ray diffraction apparatus employed in this study

CHAPTER 4

RESULTS AND DISCUSSION

4.1 Diesel engine's soot nanostructure and composition

4.1.1 Elemental composition

The elemental composition of the particulate matter (PM) was analyzed using energy-dispersive spectroscopy (EDS), a method that evaluates the energies of X-rays released by the atoms in the sample when they are excited by an electron beam. The resulting spectra of the EDS analysis are presented in **Figure 4-1**, and **Table 4.1** lists the elements detected by EDS along with their corresponding % mass units. The analysis confirms that PM primarily consists of carbon (C) and oxygen (O), with respective contents of approximately 88% and 10%, as demonstrated by the tested spectra. The presence of minute peaks of copper (Cu) and silicon (Si) can be attributed to impurities from the engine lubricant and also from the collection method [42].

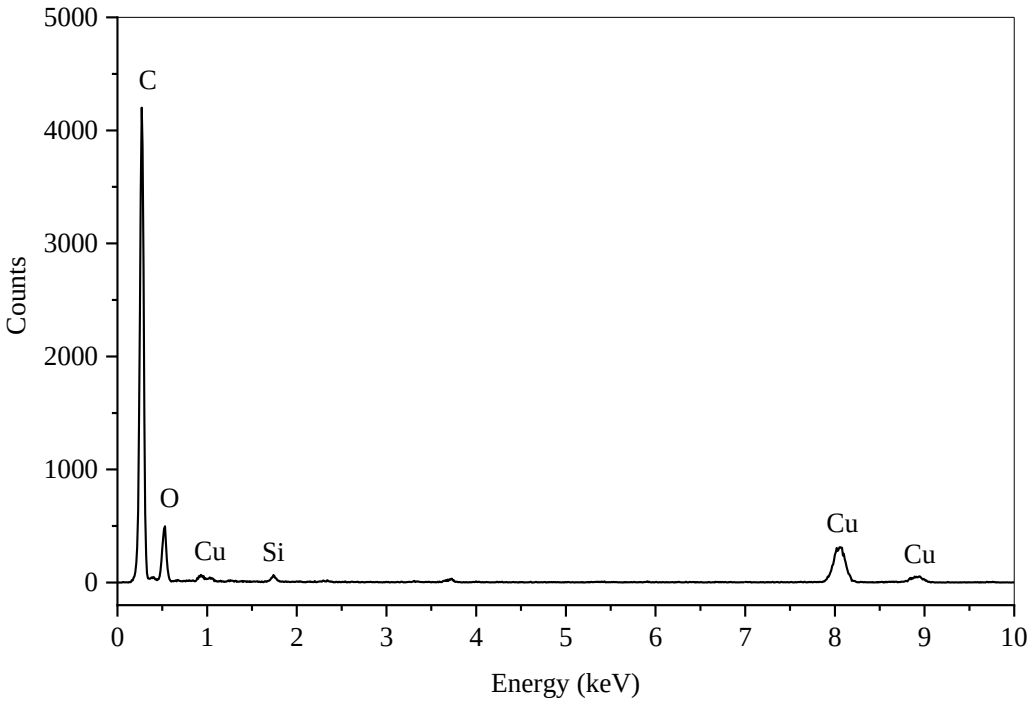

Figure 4-1 Tested spectra of Energy-dispersive spectroscopy (EDS)

Table 4-1 Elemental composition of particulate matter

Element	% mass
Carbon	87.68
Oxygen	10.22
Silicon	1.04
Copper	0.82
Nitrogen	0.24

4.1.2 Morphology and Nanostructure

Engine combustion particulate matter can be classified into two primary categories: volatile and non-volatile matter. Soot and ash are examples of non-volatile matter that result from incomplete fuel combustion within the combustion chamber. Based on their size ranges, particulate matter (PM) generated from diesel combustion can be categorized into different groups, namely PM10, PM2.5, PM1, and ultrafine particles. These categories represent particles with diameters less than 10 μm, 2.5 μm, 1 μm, and 0.1 μm, respectively [15] [44]. The morphology and nanostructure of PM including the agglomerate structure, individual particle size, fringe length, and inter-layer spacing were investigated using both transmission electron microscopy (TEM) and x-ray diffraction (XRD) methods. The agglomerate structure is made up of single primary particles, which can be visualized in **Figure 4-2** through the displayed TEM images of agglomerated ultrafine particles at 80,000x magnification. The particle size diameters were systematically measured using ImageJ image processing software, which randomly analyzed over one hundred particles. The collected data was then utilized to construct a size distribution histogram graph, presented in **Figure 4-3**. The results revealed that the single primary particles ranged from 10nm to 55 nm, with the highest peak of particle sizes observed within the range of 30-35 nm. Furthermore, the average individual primary particle diameter was approximately 29 nm.

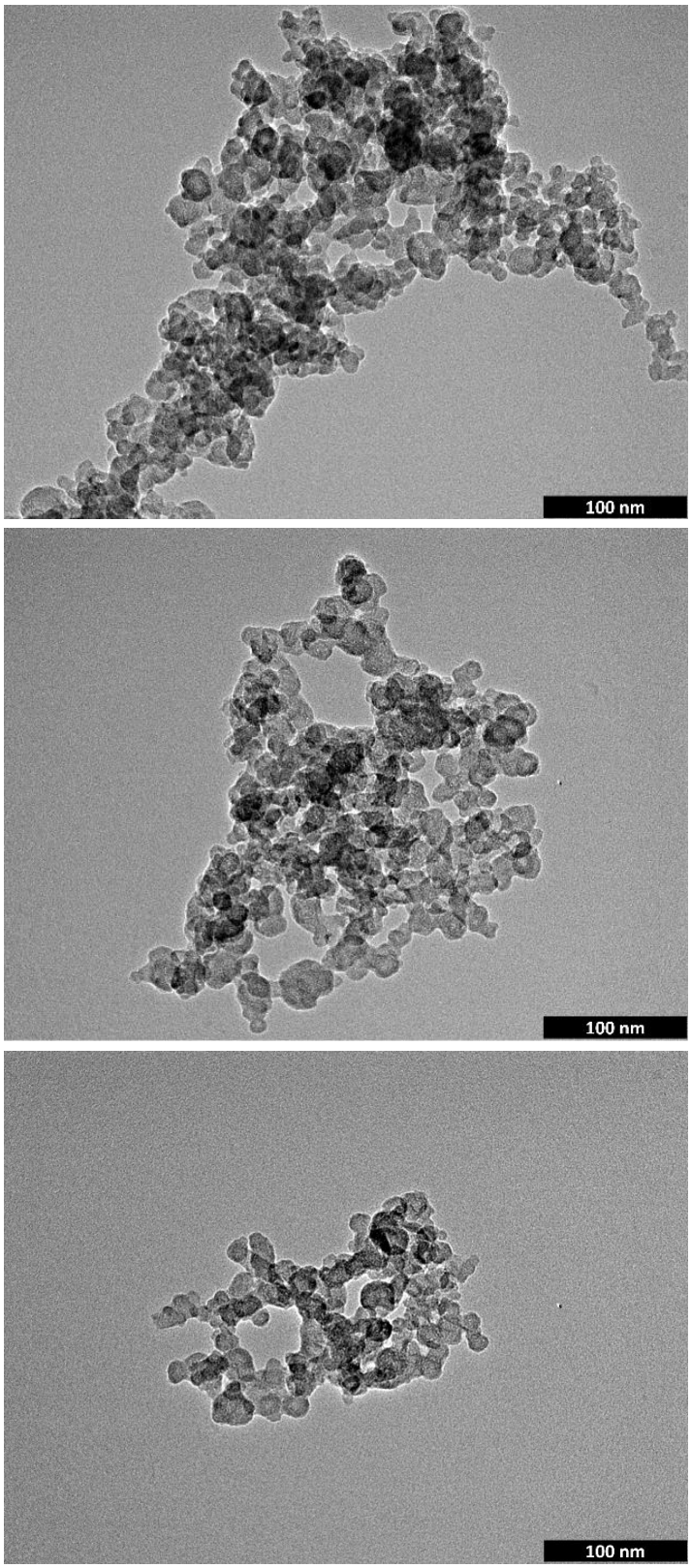

Figure 4-2 TEM images of PM agglomerate structure in 80,000x magnification

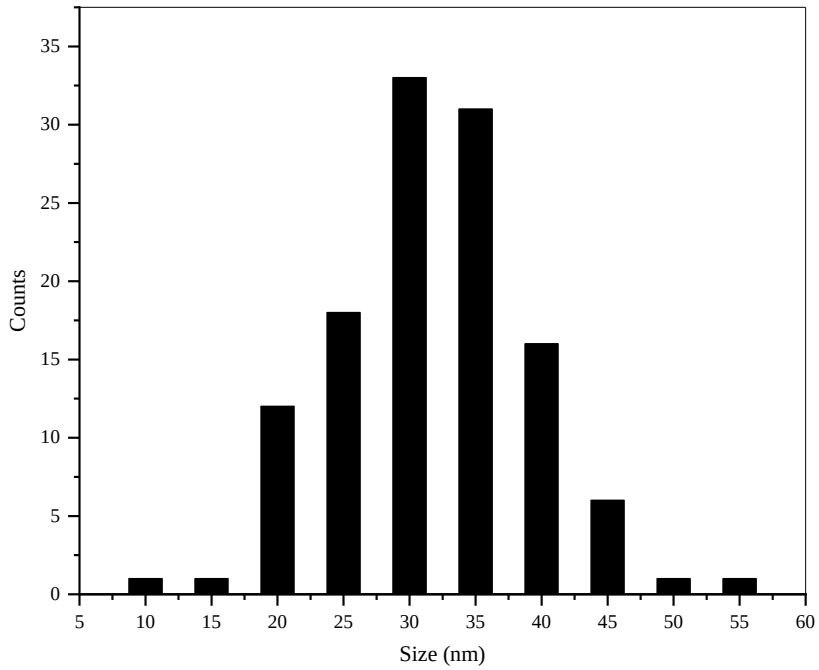

Figure 4-3 Particle size distribution obtained from ImageJ with TEM analysis

Figure 4-4 displays the results of TEM analysis in 800,000x magnification, showing individual single primary particles and the carbon fringes that represent the carbon crystallite comprising these particles. ImageJ software was utilized for further analysis of the TEM images. As a first step, these TEM images were polarized into black and white, allowing for the visualization of fringes representing the crystallite nanostructure., seen in the 20x20 nm image in **Figure 4-5**. The continuation of the analysis is presented in **Figure 4-6**, which depicted the initial cropped image, followed by the black and white conversion of the image, and finally, the skeletonized image. Subsequently, the skeletonized images were used to measure the curved skeletonized fringe lengths and interlayer spacing. The measurement results of the fringe lengths were presented as a distribution histogram graph in **Figure 4-7**. The summarized results of the TEM fringe analysis, including the maximum fringe length, average fringe length, and interlayer spacing are presented in **Table 4.2**. Based on the analysis, it was found that the fringe lengths of all carbon crystallites ranged from 0.5 nm to 7.5 nm, with the majority of them being concentrated within the range of 0.5 nm to 1.5 nm, with the interlayer spacing value representing the distance between carbon crystallites, estimated at 0.37 nm.

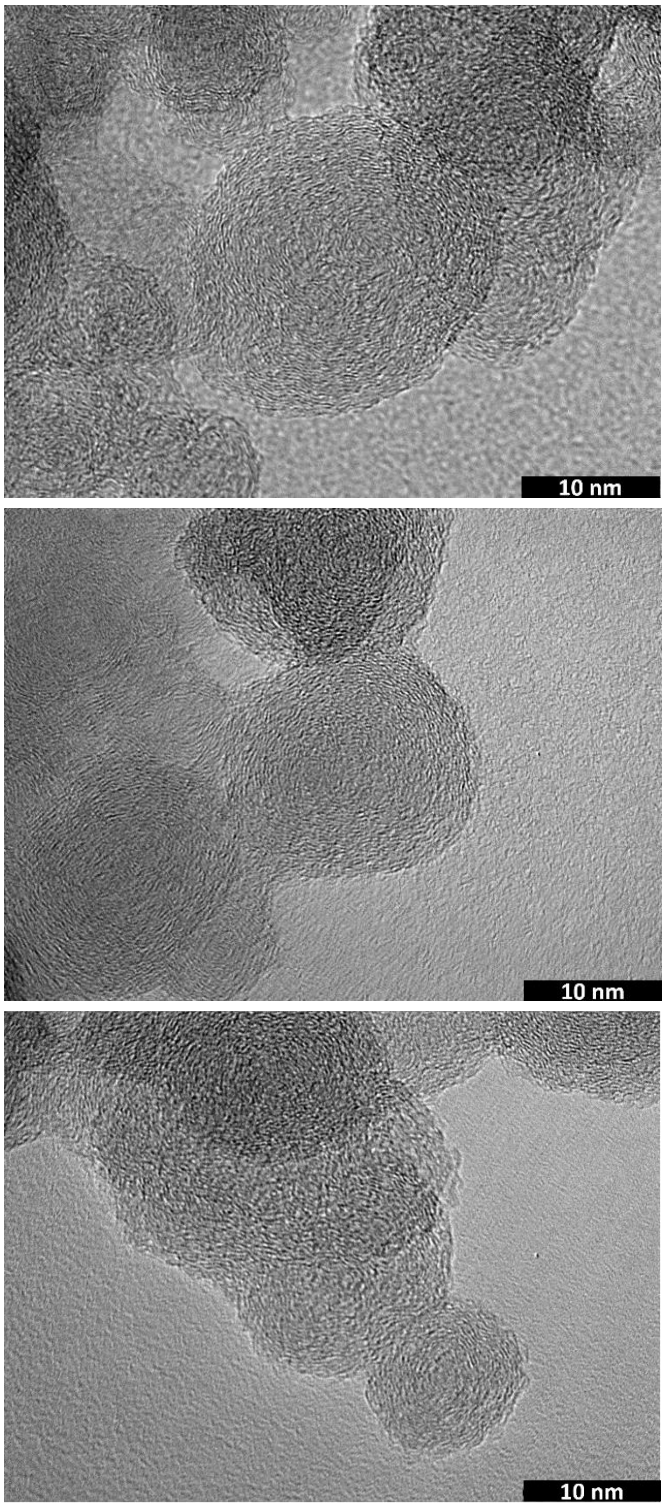

Figure 4-4 TEM images showing the individual primary particle of PM

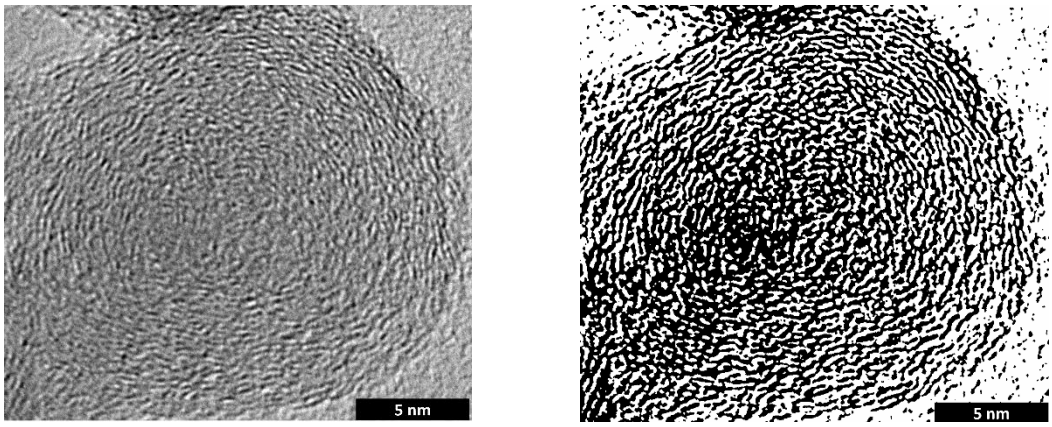

Figure 4-5 PM graphic nanostructure in 20x20 nm black and white image

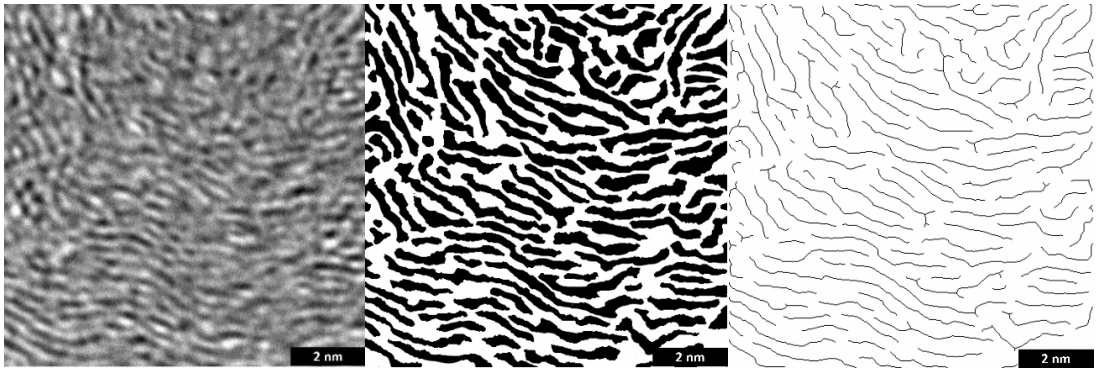

Figure 4-6 ImageJ combined with TEM image analyzing process

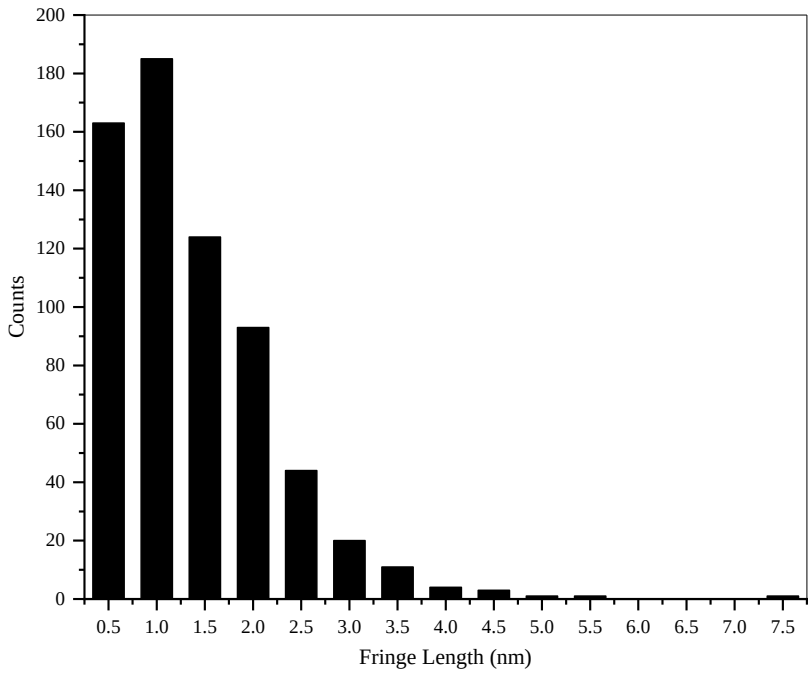

Figure 4-7 Fringe length distribution of particulate matter

Table 4-2 Summarized TEM fringe length analysis

	Average (nm)	Max (nm)	Count	D-space (nm)	Count
TEM	1.12	7.198	650	0.37	250

The X-ray diffraction (XRD) method was also used to determine the structural characteristics of the carbon material, including the crystallite length and interlayer spacing, in comparison to the TEM analysis. **Figure 4-8** displays the XRD pattern of PM, which was processed using a model fit. The resulting two curves, representing the 002 and 100 planes, were analyzed by Gaussian lines with an R^2 value higher than 0.95. After performing the Gaussian analysis on the XRD pattern, the results provided the parameter including full width at half maximum (FWHM), amplitude, and center and these parameters were then used to determine the structural characteristics of the carbon material, using equations 3.9-3.11. **Table 4.3** provides a summary of the comparison between the results obtained from XRD and TEM analyses. Based on the XRD analysis, the crystallite length and interlayer spacing were found to be 7.17 nm and 0.36 nm, respectively while the TEM analysis yielded values of 7.198 nm and 0.37 nm, respectively. Moreover, there were 3.29 nos. of graphene layers per stack. The study also involved an examination of a model that depicted the arrangement of carbon atoms, with an interatomic distance of 1.421 angstroms (Å) or 0.1421 nm between adjacent carbon atoms within the hexagonal ring. The integration of fringe length, interlayer spacing, and the number of graphene layers led to the calculation of a closed volume, which corresponded to the carbon atom density. The calculation revealed a density of 89 atoms per cubic nanometre and a carbon density of 1.77 grams per cubic centimeter, which were similar to the properties of commercial products of industrial graphite.

Table 4-3 Summary results from TEM and XRD analysis

TEM analysis		XRD analysis		
D_{002} (nm)	L_a (nm)	D_{002} (nm)	L_a (nm)	N (nos)
0.37	7.198	0.36	7.17	3.29

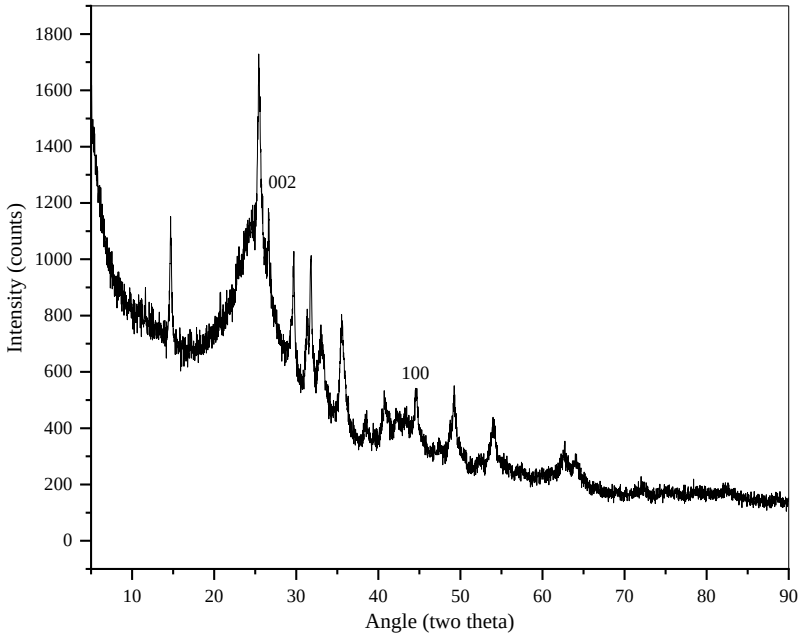

Figure 4-8 X-ray diffraction pattern of particulate matter

4.2 Diesel engine test

The primary purpose of the diesel engine test was to assess how the partial flow diesel particulate filter (P-DPF) and diesel oxidation catalyst (DOC) affected engine performance, emissions, and combustion characteristics.

4.2.1 Combustion characteristics

The combustion analysis focused on the examination of the combustion profile, including in-cylinder pressure versus volume and in-cylinder pressure versus crank angle diagrams, net heat release rate (NHRR), cumulative net heat release (CNHR), combustion duration, and mass fraction burned for both the cases with and without the after-treatment system.

Analysis of pressure within the combustion pressure

The variations in the in-cylinder pressure in relation to the volume of cylinder 1 are depicted in **Figure 4-9** for an engine operating at three different speeds: (a) 1000 rpm, (b) 1500 rpm, and (c) 2000 rpm. The measurements were conducted both with and without the installation of an after-treatment system. Additionally, four different torque levels were applied: 56 Nm, 84 Nm, 112 Nm, and 140 Nm, and the pressure axis of the diagram was presented on a logarithmic scale to enhance the visibility of the operating cycle. With and without the partial filter system, the pressure inside the combustion chamber is always different because the kinetic energy inside the residual

gas molecules increased when the partial filter is installed. This can be further contributed that the backpressure historically remains during the combustion cycles. At 1000 rpm, the pressure during the exhaust stroke and intake stroke increased. This can be contributed that the exhaust pressure increased due to the backpressure and the intake pressure increased because the high pressurized condition remained even at the end of the exhaust stroke. At 1500 and 2000 rpm, the pressure during the intake and exhaust stroke becomes stable. However, the pressure during the combustion and power stroke increased because the exhaust loss and heat loss were reduced by the partial filter system.

Figure 4-10 illustrates the combustion pressure profiles in relation to the crank angle for different engine conditions, comparing the results obtained with and without the after-treatment system. The analysis involved the selection of 200 representative cycles at each engine condition, and the data presented represents the average values for a single process. The analysis results for the maximum pressure values and corresponding crank angle locations, comparing the configurations with and without the Diesel Oxidation Catalyst (DOC) and Particulate Diesel Particulate Filter (P-DPF). These results are presented in **Table 4.4.** The findings indicated a direct correlation between combustion pressure peaks and engine torque with higher engine torque requiring increased fuel injection and combustion. In terms of engine speeds, faster combustion cycles at higher engine speeds resulted in reduced fuel-air mixing time. Thus, higher engine speeds led to a lower proportion of fuel burned in premixed combustion and a higher percentage of fuel burned in diffuse combustion, as compared to lower engine speeds. Consequently, the peak in-cylinder pressure diminished with faster engine revolutions or higher engine speeds. Additionally, when both engine speeds and torques increased, the peak locations of combustion pressure deviated from the 0° crank angle (top dead center, TDC). Following the installation of the diesel oxidation catalyst (DOC) upstream of the partial flow diesel particulate filter (P-DPF), the findings indicated a notable increase in peak in-cylinder pressure. This increase in pressure was attributed that the pressure and temperature inside the cylinder are induced by the higher kinetic energy inside the residual gas molecules due to the backpressure. Moreover, at 1000 rpm, a delay in the initiation of combustion was observed due to an extended ignition delay specific to this engine condition.

Further discussion regarding this matter will be provided in detail in the heat release rate section.

Figure 4-11 illustrates a comparative analysis of the combustion temperature as a function of crank angle both in the presence and absence of the partial filter system to provide a more in-depth insight into the thermal dynamics within the combustion chamber. In both scenarios, i.e., with and without the partial filter system, an increase in combustion temperature is evident, attributed to the presence of residual gas fractions within the combustion chamber. Furthermore, it is noteworthy that when the partial filter system is employed, a notable temperature augmentation is observed during the intake and exhaust strokes at 1000 RPM, while at 1500 and 2000 RPM, the temperature elevation primarily occurs during the combustion and power strokes, mirroring a consistent pattern observed in the pressure profile.

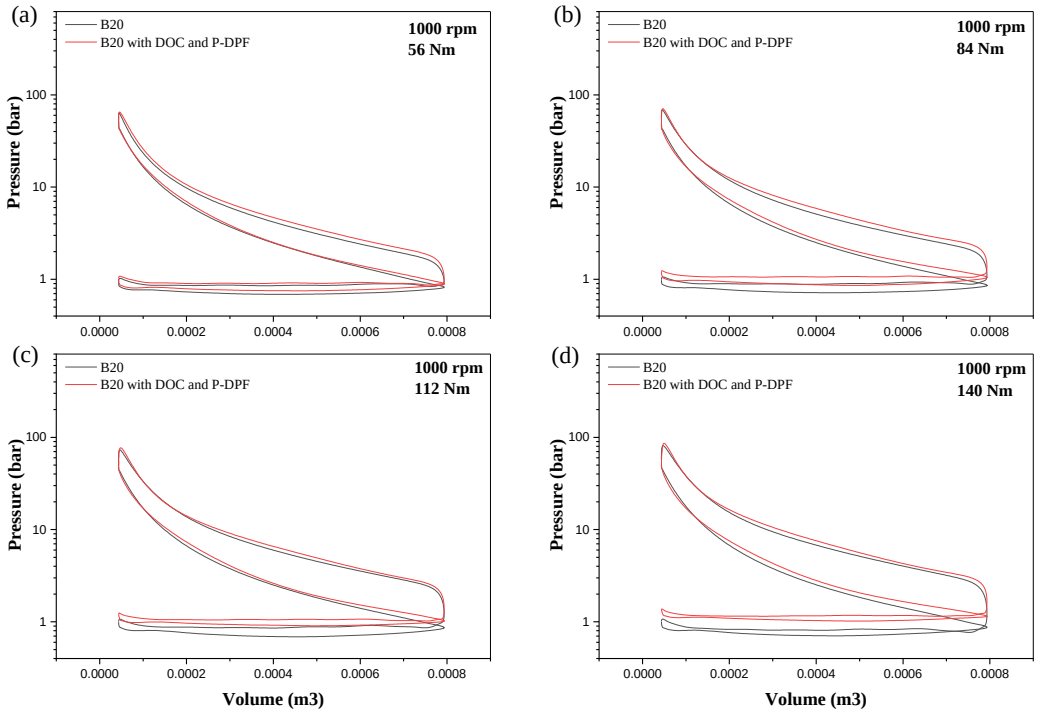

(a) 1000 rpm

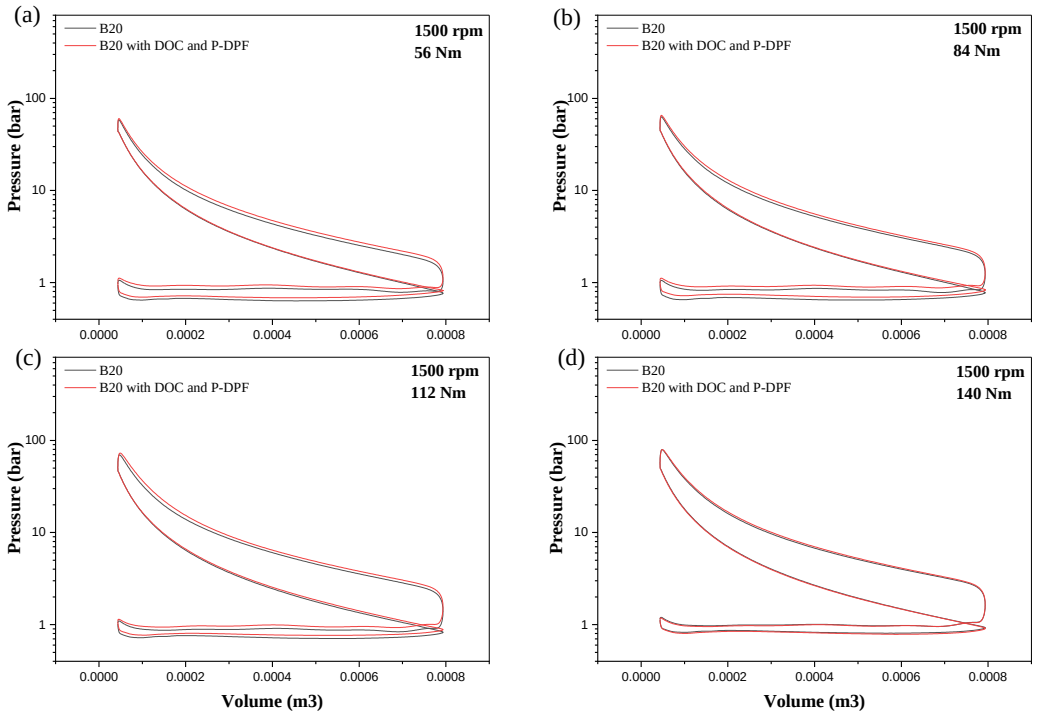

(b) 1500 rpm

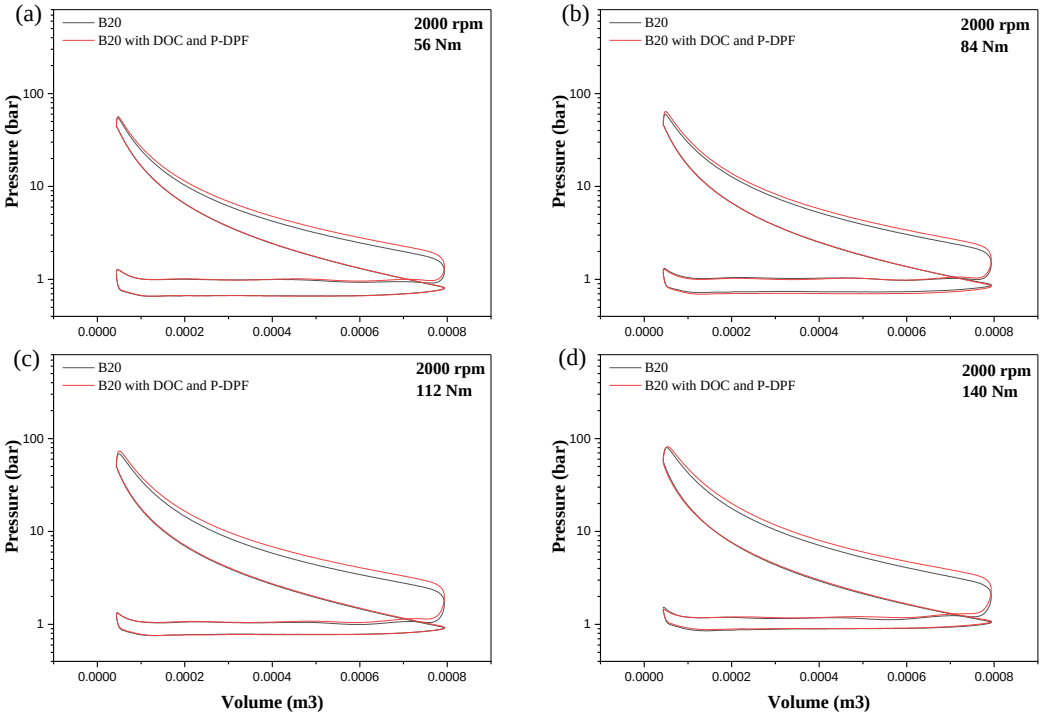

(c) 2000 rpm

Figure 4-9 Comparison of in-cylinder pressure versus volume diagram with and without the installation of DOC and P-DPF at three different engine speeds

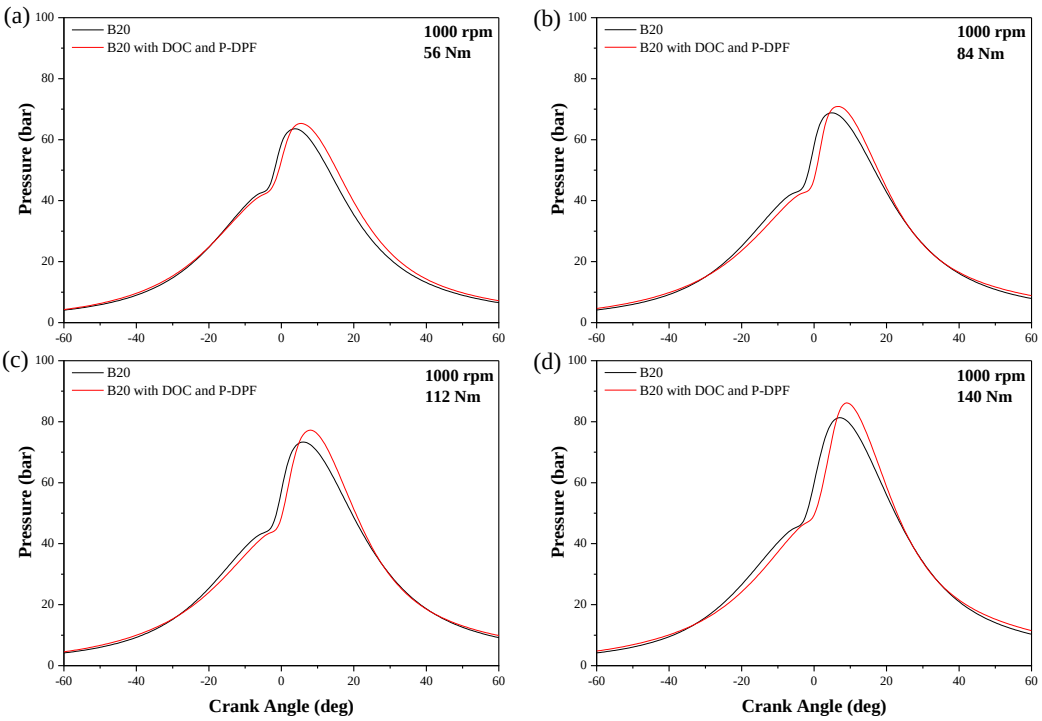

(a) 1000 rpm

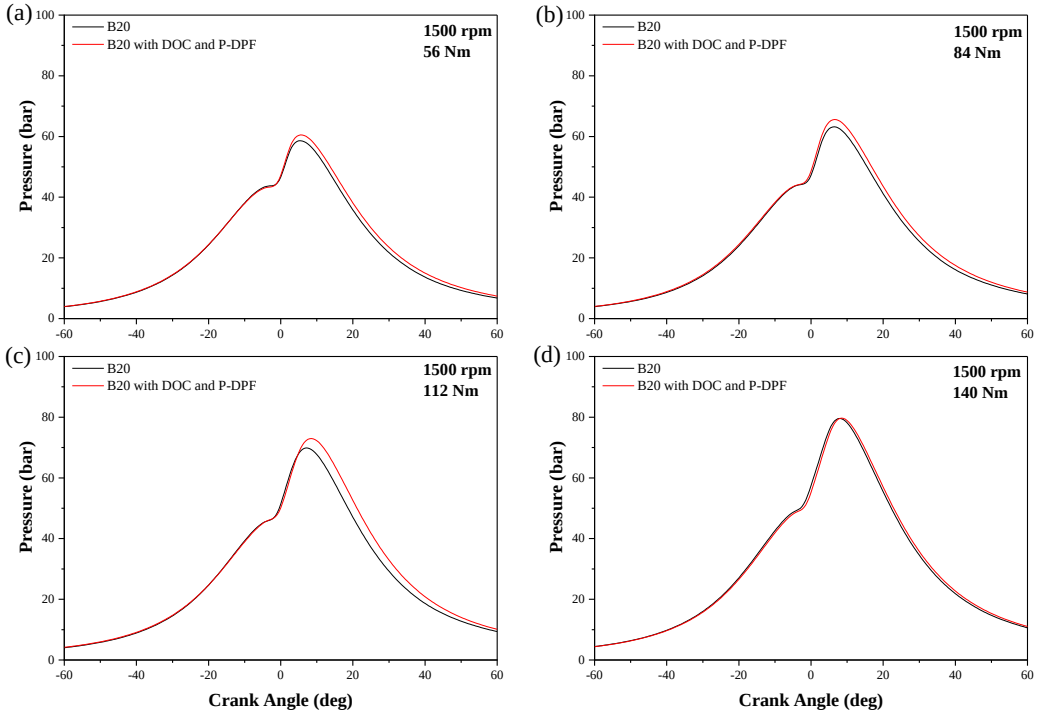

(b) 1500 rpm

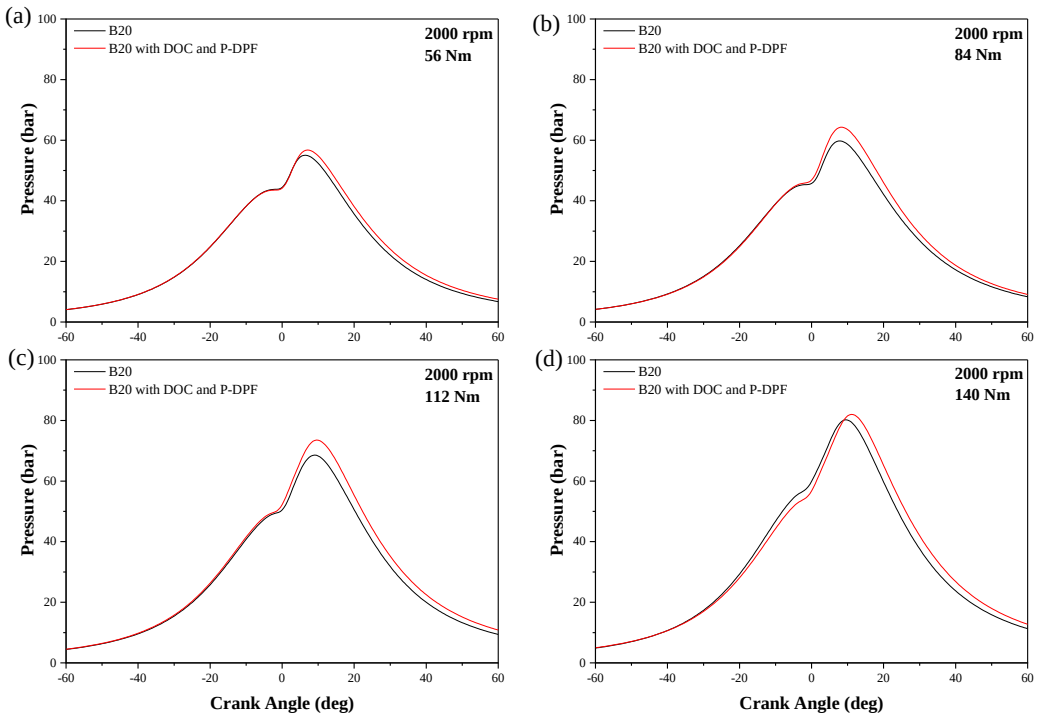

(c) 2000 rpm

Figure 4-10 Comparison of combustion pressure versus crank angle with and without the installation of DOC and P-DPF at three different engine speeds

Table 4-4 Comparison of maximum in-cylinder pressure and crank angle locations

Engine speed	Engine torque	B20		B20 with DOC and P-DPF	
		Pressure (bar)	Crank Angle (degree)	Pressure (bar)	Crank Angle (degree)
1000 rpm	56 Nm	64	4	65	5.5
	84 Nm	69	5	71	6.5
	112 Nm	73	6	77	8
	140 Nm	81	7	86	9
1500 rpm	56 Nm	59	5.5	60	5.5
	84 Nm	63	6.5	66	6.5
	112 Nm	70	7	73	8.5
	140 Nm	80	8	80	8.5
2000 rpm	56 Nm	55	6.5	57	7
	84 Nm	60	8	64	8.5
	112 Nm	69	9	74	9.5

	140 Nm	80	9.5	82	11

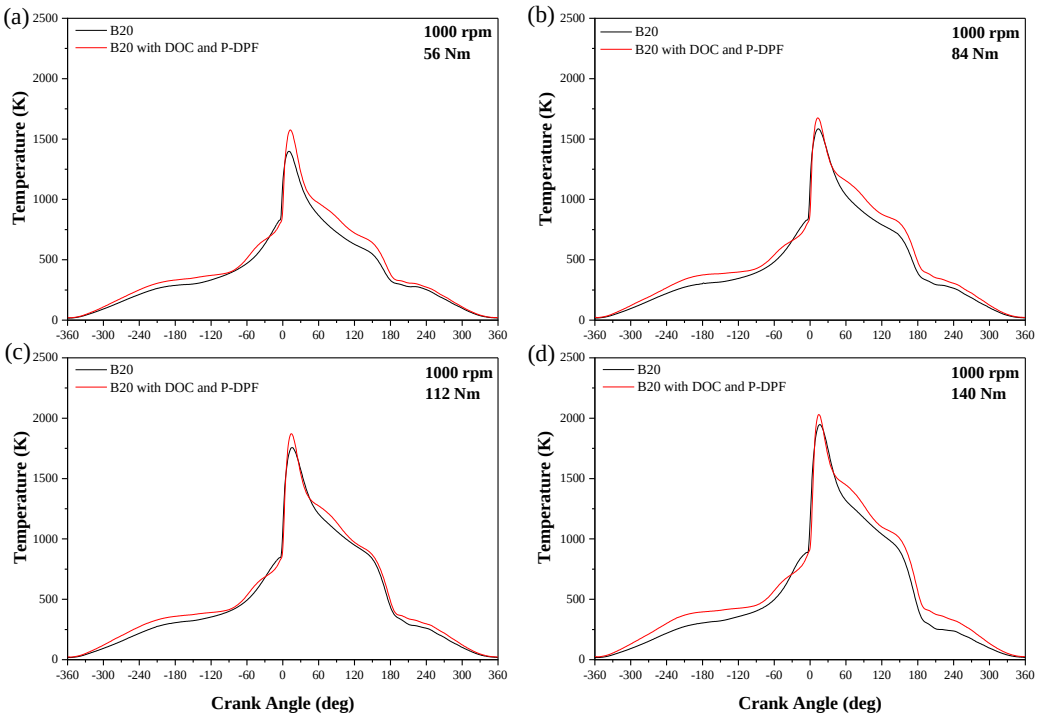

(a) 1000 rpm

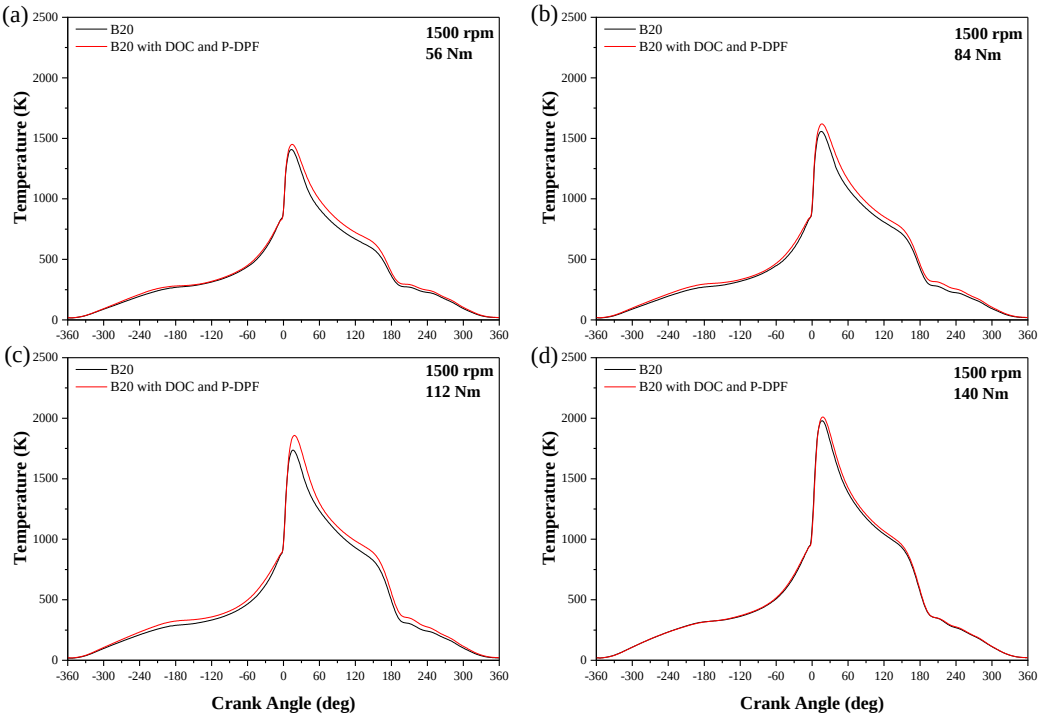

(b) 1500 rpm

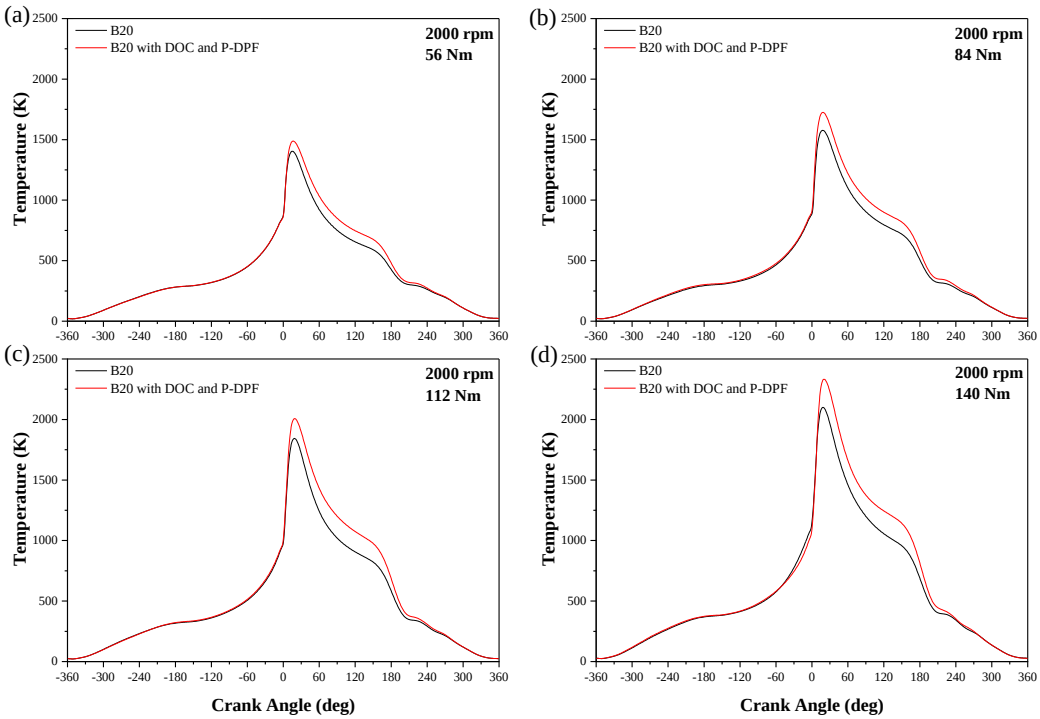

(c) 2000 rpm

Figure 4-11 Comparison of combustion temperature versus crank angle with and without the installation of DOC and P-DPF at three different engine speeds

Rate of net heat release and cumulative net release

Figure 4-12 depicts the variation in net heat release rate (NHRR) with respect to crank angle to facilitate a comprehensive understanding of the amount of heat energy available for efficient work conversion during the combustion process. The net heat release rate (NHRR) is significantly influenced by the ignition delay and injection timings. Under the measured conditions, the NHRR patterns show premixed combustion followed by diffuse combustion. At the start of the combustion, the NHRR showed a negative value due to the delayed vaporization of fuel during the ignition delay. As the combustion process started, the NHRR changed to a positive value [45]. With the augmentation of engine torque, there was a discernible elevation in both the cylinder wall temperature and charge temperature. There was also a simultaneous increase in the amount of fuel accumulating inside the combustion chamber. The combined effects of certain factors resulted in an improvement in ignition timing, leading to an increase in the net heat release rate (NHRR). At an engine speed of 1000 rpm, the entire fuel was combusted during the premixed combustion phase, which caused a longer ignition delay period compared to engine speeds of 1500 rpm and

2000 rpm. This extended ignition delay allowed for a longer duration for the fuel and air to evaporate and mix thoroughly. As a result, the prolonged mixing period contributed to a higher net heat release rate (NHRR), particularly at 1000 rpm, regardless of the utilization of the after-treatment system. When employing a diesel oxidation catalyst (DOC) and a particulate filter (P-DPF), it was observed that the net heat release rate (NHRR) exhibited an increase. This phenomenon can be attributed to the elevated pressure and temperature within the combustion chamber induced by the backpressure, as the retained exhaust gases contributed to the thermal energy of the system. Furthermore, at 1000 rpm, a prolonged ignition delay was observed. This can be attributed to the influence of backpressure on the residual gas fraction (RGF), which represents the quantity of exhaust gases retained in the cylinder during the exhaust and intake strokes which might influence the dilution effect of fuel and air, ultimately resulting in a lengthened ignition delay at low engine conditions. However, according to a study conducted by Dalla Nora et al. [46], higher engine speeds did not necessarily impede the process and the energy losses could be effectively recovered under these circumstances.

The variations in cumulative net heat release (CNHR) throughout the crank angle are illustrated in **Figure 4-13**, portraying the total amount of heat generated during the entire combustion process within the engine cylinder. The cumulative net heat release (CNHR) exhibited an upward trend as engine loads increased. This can be attributed to the larger quantity of fuel injected into the cylinder to generate higher output power. The implementation of the after-treatment system led to a noticeable increase in the trend of cumulative net heat release (CNHR), in contrast to the experiment conducted without DOC and P-DPF. However, the difference in CNHR between the two cases was not significantly different from the NHRR diagram. Additionally, it was observed that the presence of the after-treatment system leads to elevated heat dissipation during fuel vaporization at 1000 RPM in contrast to the conditions at 1500 and 2000 RPM. This discrepancy can be attributed to the lower heat capacity within the combustion chamber at 1000 RPM. It is conceivable that at higher engine speeds, the heat loss is potentially recuperated more effectively.

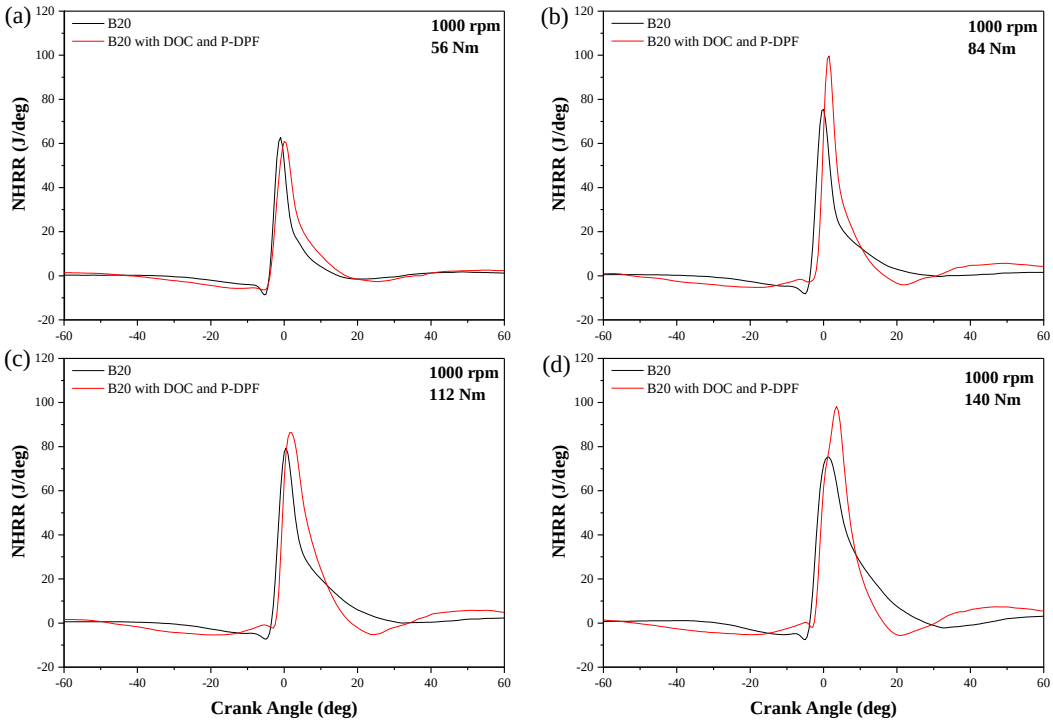

(a) 1000 rpm

(b) 1500 rpm

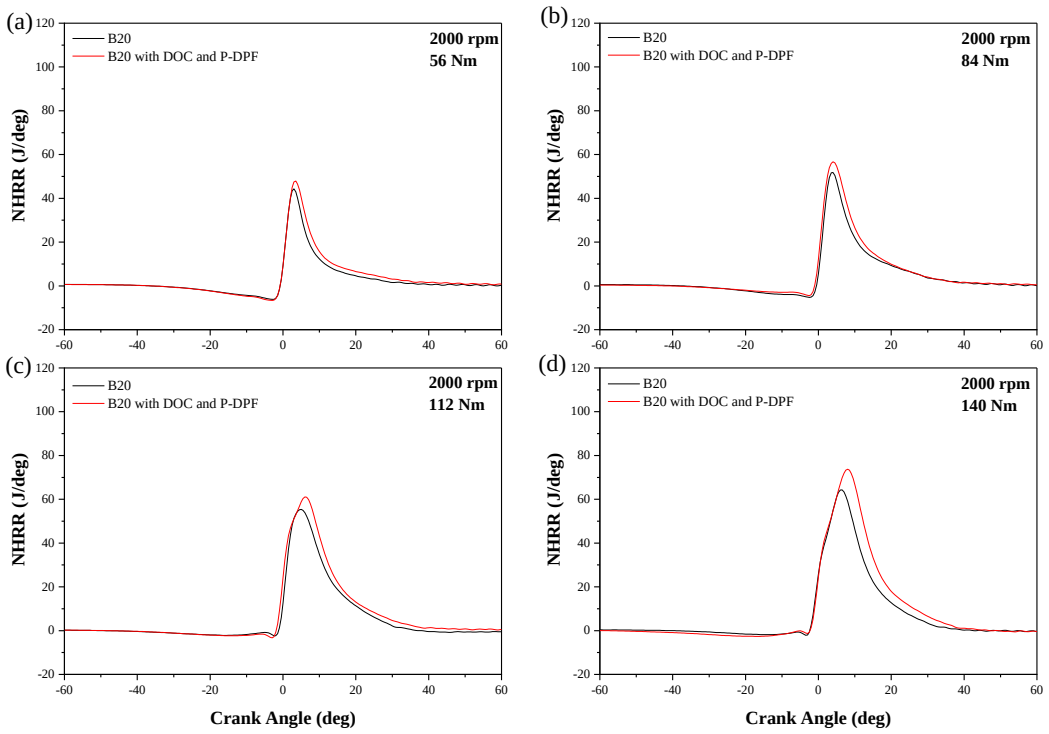

(c) 2000 rpm

Figure 4-12 Comparison of net heat release rate (NHRR) versus crank angle with and without the installation of DOC and P-DPF at three different engine speeds

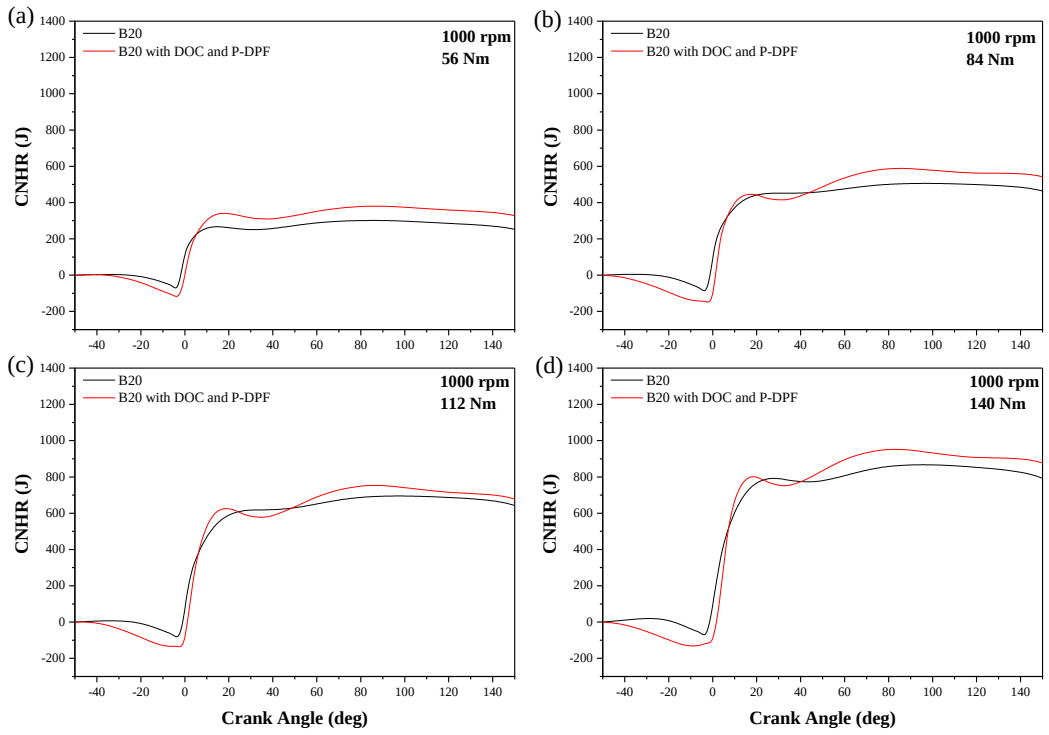

(a) 1000 rpm

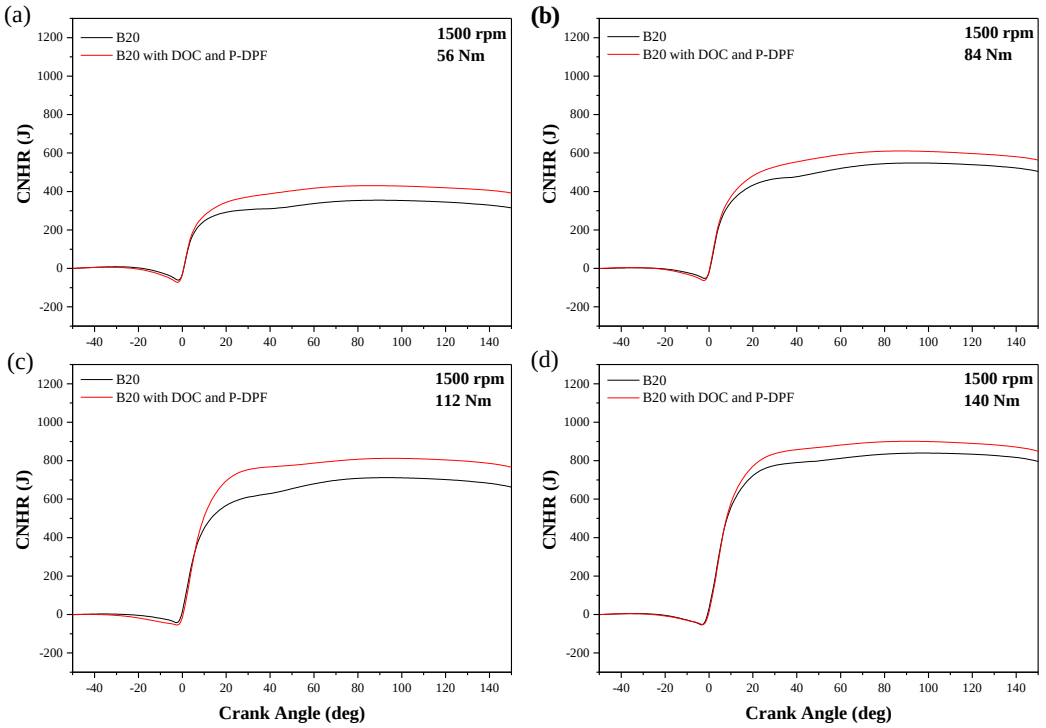

(b) 1500 rpm

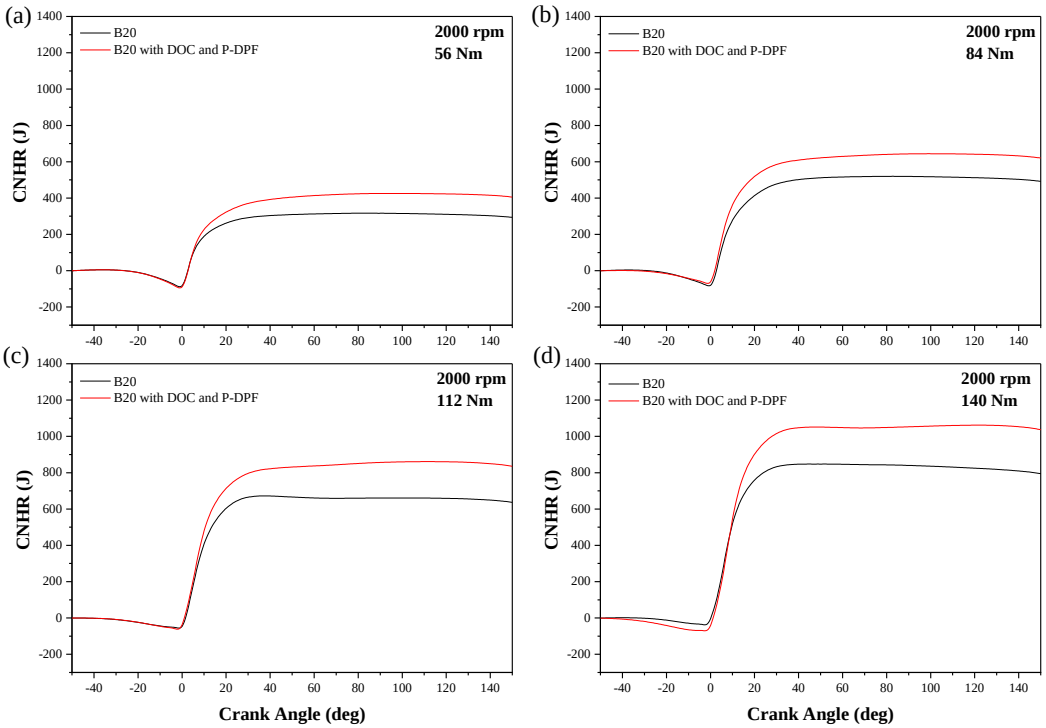

(c) 2000 rpm

Figure 4-13 Comparison of cumulative net heat release (CNHR) versus crank angle with and without the installation of DOC and P-DPF at three different engine speeds

4.2.2 Engine performance

In order to evaluate the impact of incorporating the DOC and P-DPF in a diesel engine, various metrics related to fuel consumption and efficiency were measured and analyzed. These metrics encompassed fuel consumption, indicated fuel consumption, indicated specific fuel consumption (ISFC), indicated specific energy consumption (ISEC), brake specific fuel consumption (BSFC), brake specific energy consumption (BSEC), indicated thermal efficiency (ITE), and brake thermal efficiency (BTE). The obtained measurements were subject to comprehensive examination and subsequent discussion regarding their significance. The calculation of indicated parameters, including ISFC, ISEC, and ITE, primarily relied on in-cylinder pressure, volume, and fuel consumption. On the other hand, the calculation of brake parameters involved engine speed, torque, and fuel consumption data.

Figure 4-14 illustrates the comparison of engine fuel consumption before and after the implementation of the DOC and P-DPF. The measurement of fuel consumption in this study involved the use of a weight scale and timer, with each recording lasting thirty seconds. The measurements were repeated three times, and the results were averaged to minimize uncertainties. The findings indicate that fuel consumption exhibited an increase in correlation with both engine speed and load, which is consistent with the requirement for higher power output under elevated engine conditions. After the diesel oxidation catalyst (DOC) and partial flow diesel particulate filter (P-DPF) were installed, a minor rise in backpressure was observed, ranging from 0.2 kPa at 1000 rpm and 56 Nm to 2.25 kPa at 2000 rpm and 140 Nm. This increase in backpressure resulted in a corresponding increase in fuel consumption. However, considering the relatively modest rise in backpressure, the installation of the after-treatment system had no discernible impact on fuel consumption, which, on average, experienced an approximate 1% increase.

Figure 4-15 and **Figure 4-16** depict the observed values of indicated specific fuel consumption (ISFC) and brake specific fuel consumption (BSFC) with the unit of kg/kWh for different engine conditions, comparing the results with and without the installation of the DOC and P-DPF. These figures provide valuable insights into the variations in fuel consumption efficiency under the influence of the after-treatment system across a range of operating conditions. A consistent downward trend was observed for both ISFC and BSFC as the engine load increased. This can be attributed

to the higher fuel requirement at lower engine loads due to the comparatively lower in-cylinder temperatures. The lower temperatures adversely affect fuel atomization and impede the formation of an ideal fuel/air mixture, resulting in diminished fuel efficiency and elevated specific fuel consumption during operation at lower engine loads. The installation of DOC and P-DPF resulted in a reduction in ISFC. This decrease in ISFC was determined based on indicated power, which was calculated using combustion pressure and volume. The findings revealed that as the combustion pressure increased, implying increasing indicated power, the indicated specific fuel consumption (ISFC) decreased. In terms of brake-specific fuel consumption (BSFC), it exhibited an increasing trend, aligning with the behavior observed in fuel consumption, when the brake power output was consistent between the two experiments. Resitoglu et al. [47] similarly reported an increase in BSFC upon the installation of exhaust after-treatment systems. The average decrease of ISFC was about 13% whereas the BSFC experienced an average increase of around 1% when the exhaust after-treatment system was used.

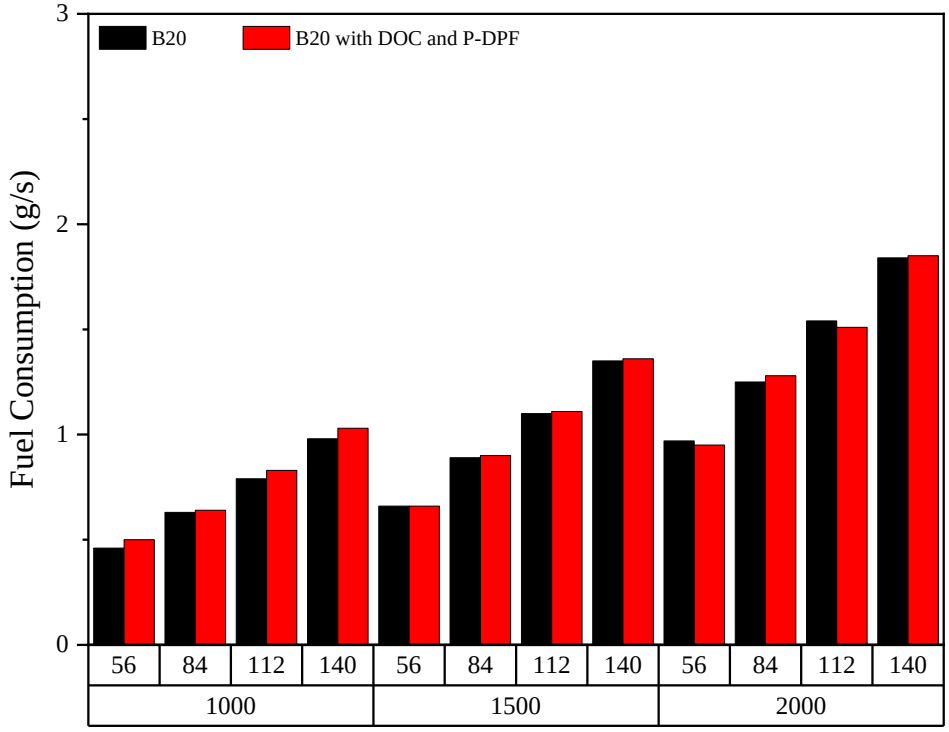

Figure 4-14 Observation of fuel consumption with and without DOC and P-DPF

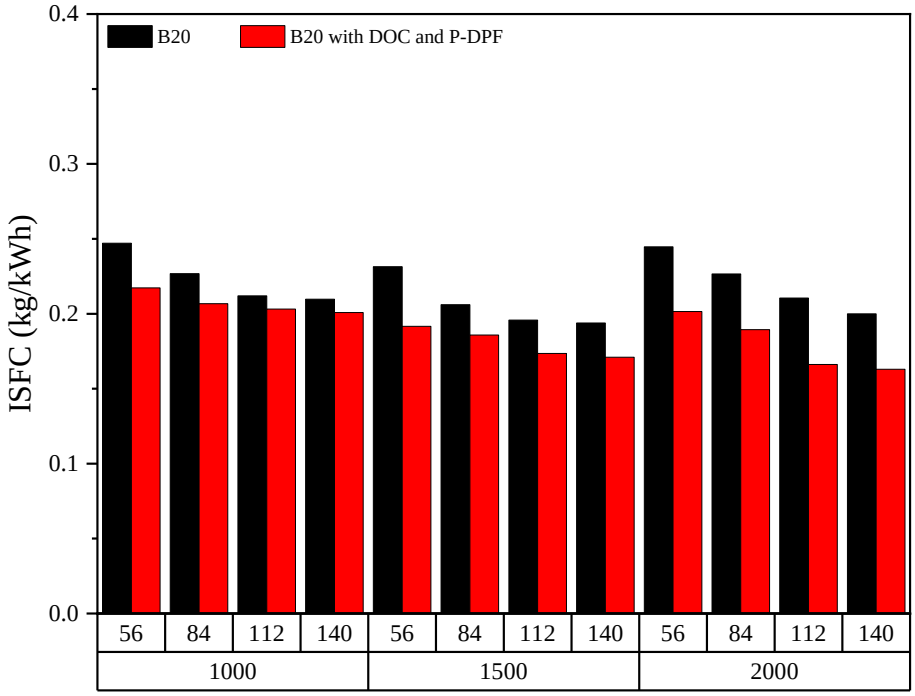

Figure 4-15 Observation of indicated specific fuel consumption (ISFC) with and without installing DOC and P-DPF

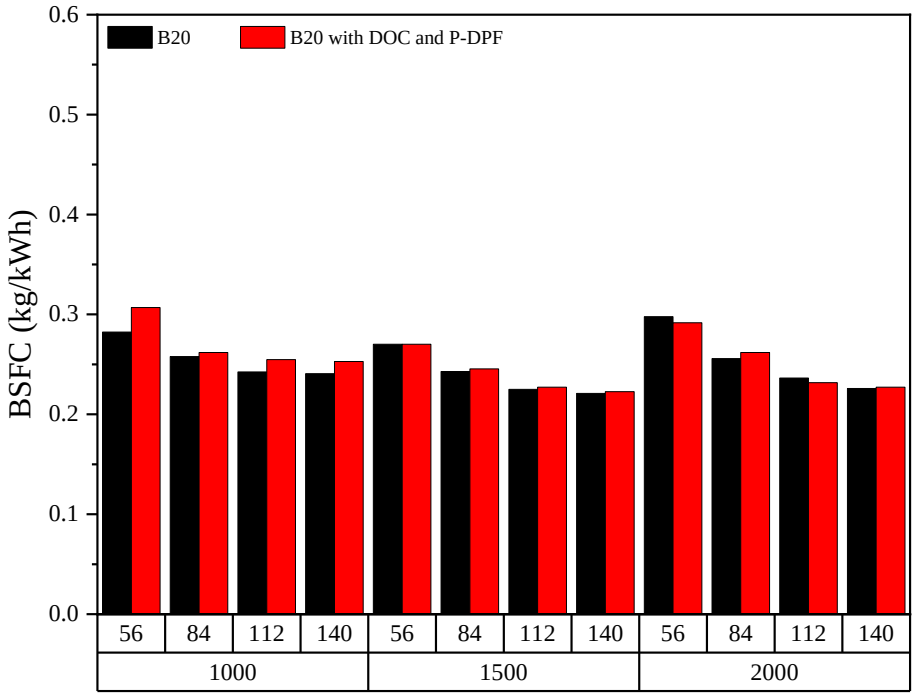

Figure 4-16 Observation of brake-specific fuel consumption (BSFC) with and without installing DOC and P-DPF

A comparison of the indicated specific energy consumption (ISEC) and brake specific energy consumption (BSEC) under various engine situations is shown in **Figure**

4-17 and **Figure 4-18**. The results are displayed for both the cases with and without the installation of DOC and P-DPF. Specific energy consumption refers to the amount of energy consumed per unit of power output and is expressed in units of kilojoules per kilowatt-hour (kJ/kWh). Both indicated specific energy consumption (ISEC) and brake-specific energy consumption (BSEC) exhibited a decreasing trend as the engine load increased. This is due to the reduced amount of heat loss experienced at increasing engine loads. After the DOC and P-DPF were installed, a reduction of approximately 13% was observed in ISEC while BSEC exhibited an increase of around 1%. These changes were consistent with the trends observed in ISFC and BSFC.

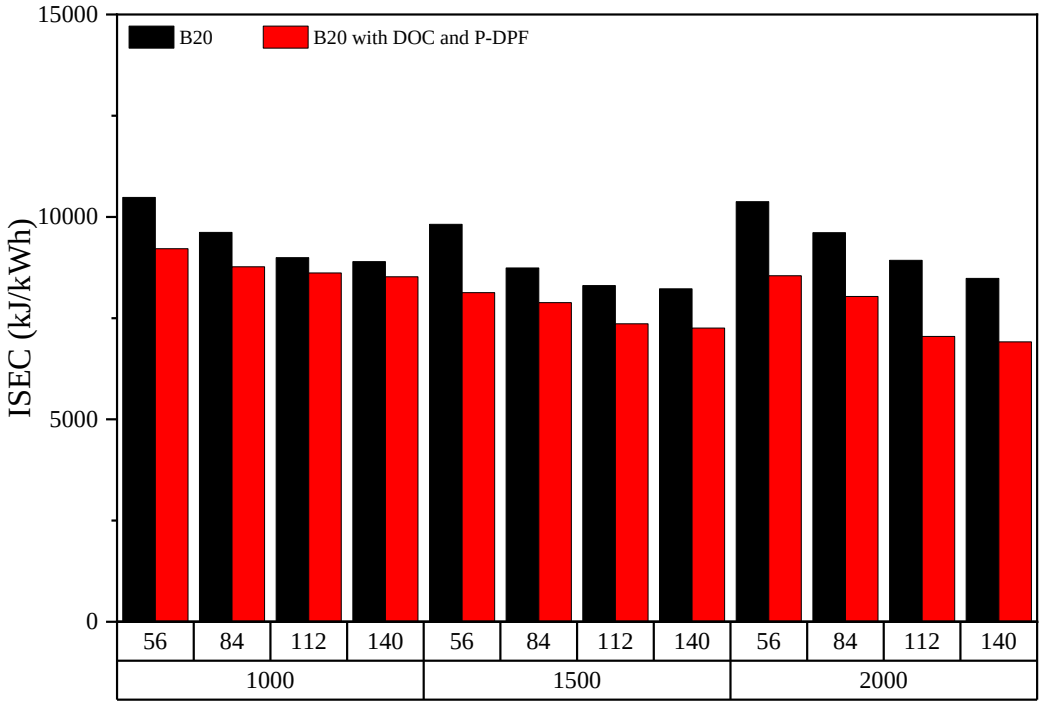

Figure 4-17 Observation of indicated specific energy consumption (ISEC) with and without installing DOC and P-DPF

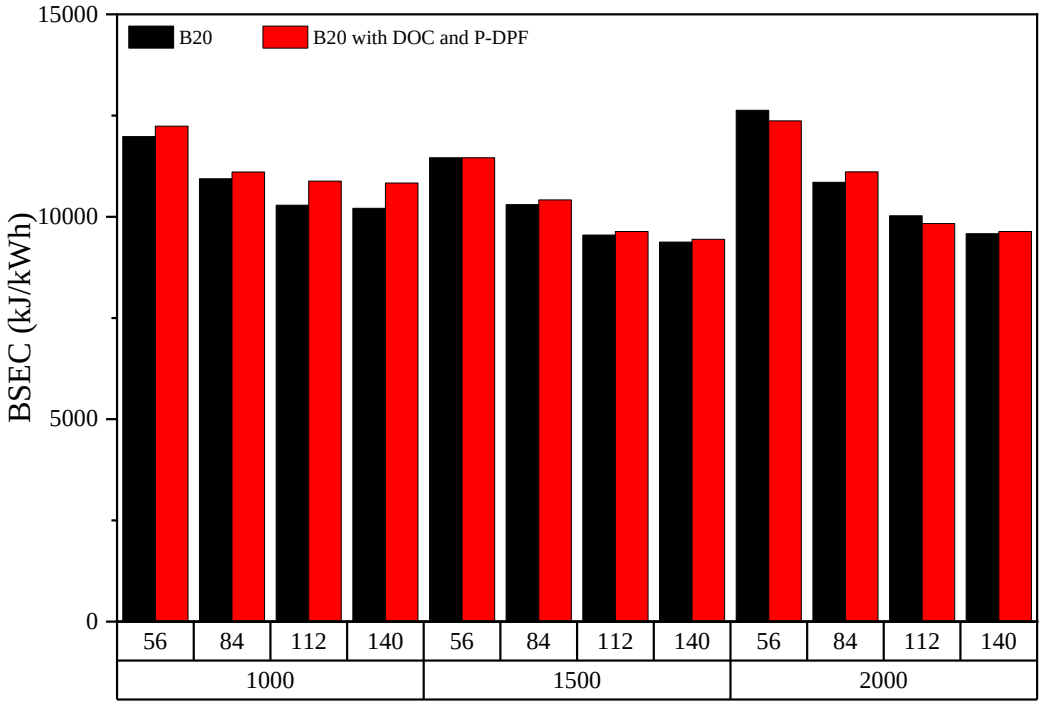

Figure 4-18 Observation of brake-specific energy consumption (BSEC) with and without installing DOC and P-DPF

Figures 4-19 and **4-20** illustrate the changes in indicated thermal efficiency (ITE) and brake thermal efficiency (BTE) when comparing the use of DOC and P-DPF to their absence. Both thermal efficiencies increased with the increased engine load and speed. In the analysis of indicated thermal efficiency (ITE), it is determined as the ratio of the output indicated power, measured using in-cylinder pressure and volume, to the input heat energy. In this calculation, thermal losses and mechanical friction losses are not taken into account, focusing solely on the combustion characteristics and quality of fuels. In the combustion pressure analysis, the in-cylinder pressure increased around 3 bar with the installation of the partial filter system which also led to increase the indicated power. As a result of this increased pressure, there was an observable increase in the indicated thermal efficiency. In contrast, brake thermal efficiency (BTE) was determined by dividing the output brake power, which was derived from the engine control torque and speed, by the input heat energy. The installation of the after-treatment system did not significantly impact on the brake thermal efficiency. In the absence of the after-treatment system, the deviation between ITE and BTE ranged from about 4% to 6% across all conditions while the deviation increased from approximately 9% to 15% when DOC and P-DPF were installed. The friction losses

increased with increasing engine speed due to the higher backpressure from the after-treatment system.

In summary, it can be concluded that the installation of the diesel oxidation catalyst (DOC) and partial flow diesel particulate filter (P-DPF) increased the indicated power which also led to increase the indicated thermal efficiency. However, the fuel consumption, BSFC, BSEC and BTE were not significantly affected by the installation of partial filter system. The difference between ITE and BTE with P-DPF system was higher than that without the filter system because the backpressure from the after-treatment system increased the friction loss.

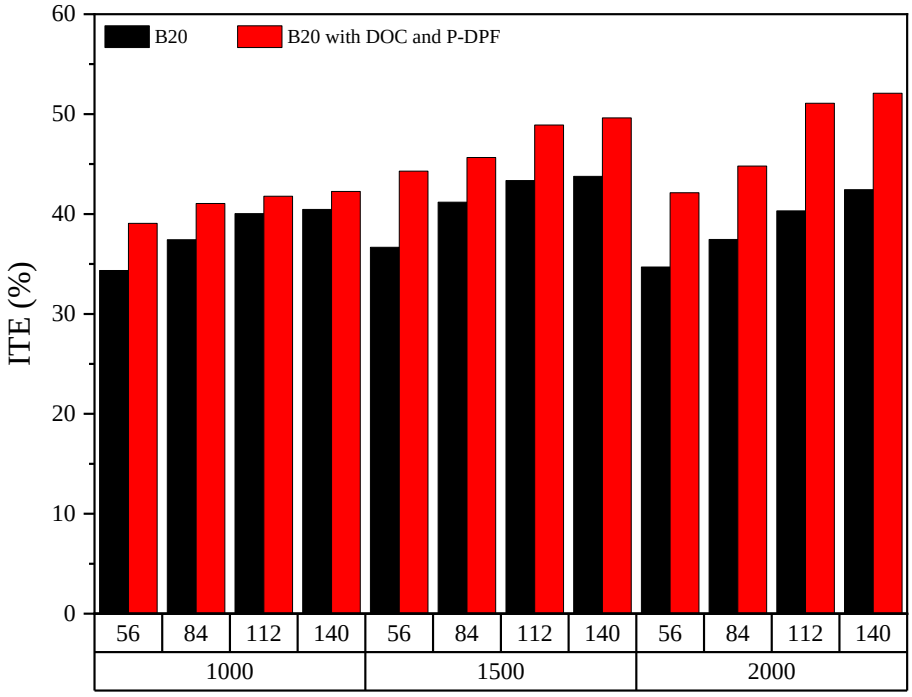

Figure 4-19 Observation of indicated thermal efficiency (ITE) with and without installing DOC and P-DPF

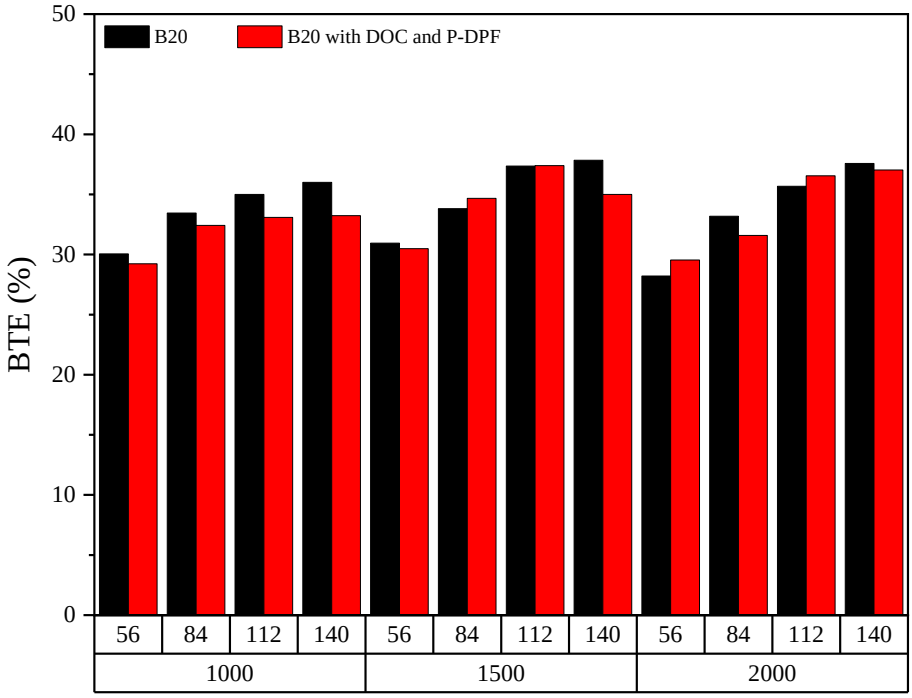

Figure 4-20 Observation of brake thermal efficiency (BTE) with and without installing DOC and P-DPF

4.2.3 Emission characteristics

To assess the effects of utilizing the diesel oxidation catalyst (DOC) and partial flow diesel particulate filter (P-DPF), several exhaust parameters were analyzed, including exhaust temperature (in degrees), smoke intensity (in percentage), carbon dioxide (CO_2), carbon monoxide (CO), oxygen (O_2), nitrogen oxide (NO) levels (in parts per million), and the equivalent fuel-air ratio (**È**). The fuel-air equivalent ratio was estimated from the exhaust emissions, as presented in **Figure 4-21**. It was observed that the equivalent ratio exhibited a gradual increase with increasing engine load. This is explained by the greater fuel injection rate into the cylinder that occurs in these circumstances. Conversely, the equivalent ratio decreased as the engine speed increased. This decrease was attributed to the elevated turbocharger boost pressure, which resulted in a greater volume of air being drawn into the intake system. The installation of the after-treatment system resulted in an increase in the fuel-air equivalent ratio. This can be attributed to the higher fuel consumption required to compensate for the additional resistance introduced by the backpressure from the after-treatment system.

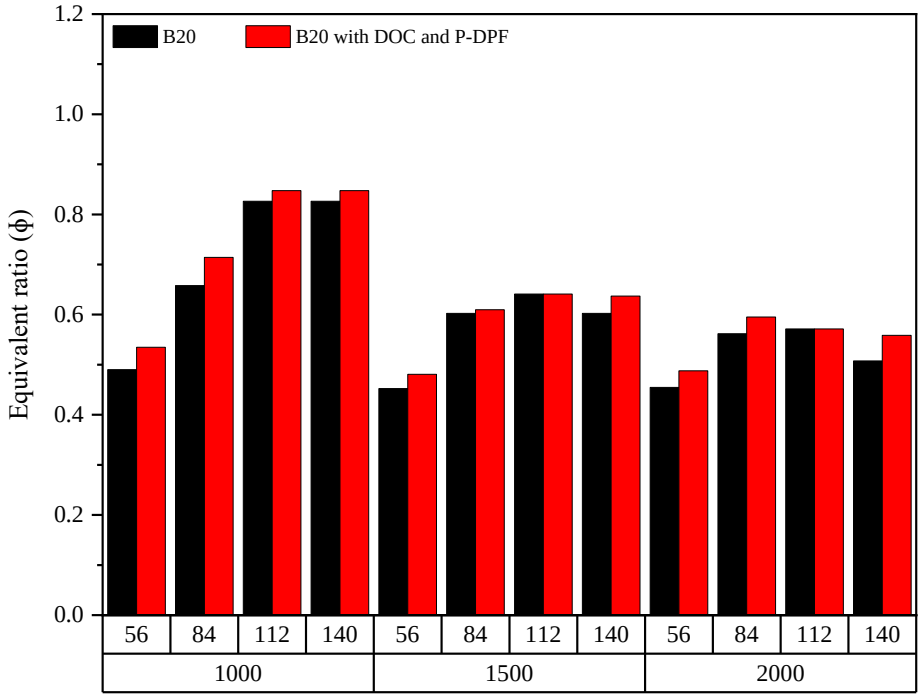

(a) Fuel-air equivalent ratio

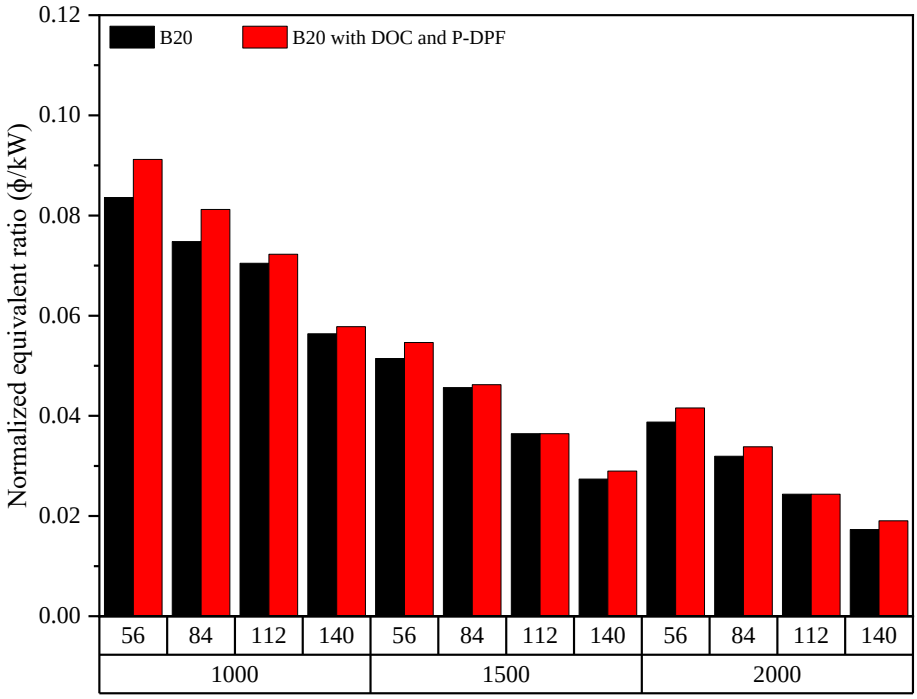

(b) Normalized fuel-air equivalent ratio

Figure 4-21 Observation of (a) fuel-air equivalent ratio and (b) normalized fuel-air equivalent ratio with and without installing DOC and P-DPF

Figure 4-22 depicts the variations of smoke intensity and its normalized values with the brake power for the tested fuel under two scenarios: with and without the

integration of the exhaust after-treatment system. This data is necessary for assessing the level of soot emissions in exhaust gases. The findings indicated that the peak smoke emissions occurred at torque levels of 112 Nm and 140 Nm, specifically when the engine was operating at 1000 rpm. This trend mirrored the observed fuel consumption pattern under these particular operating conditions. The combustion process at low engine speeds and high loads resulted in a higher fuel ratio, which consequently led to elevated levels of smoke emissions. After the installation of the DOC and P-DPF, there was an average reduction of 65% in smoke emissions. This reduction could be attributed to the trapping of soot particles on the partial filter as they passed through its trapezoidal channels. Consequently, the discussion will concentrate on the CO_2, O_2, and NO emissions, as well as the exhaust temperature, aiming to evaluate the continuous passive regeneration performance of the partial flow DPF.

Figure 4-23 illustrates the variations in carbon monoxide (CO) including its normalized values, with and without the integration of the exhaust after-treatment system. Carbon monoxide (CO) is released during the incomplete combustion of fuel, and its emissions were found to be higher at an engine speed of 1000 rpm and engine torque levels of 112 Nm and 140 Nm. These conditions are characterized by increased fuel injection and lower oxygen content, resulting in incomplete combustion. However, at constant speeds of 1500 rpm and 2000 rpm, CO emissions decreased with increasing engine load. This decrease can be attributed to the higher combustion temperatures associated with higher engine loads, which promote the oxidation of CO to carbon dioxide (CO_2) at a more rapid rate. Upon integrating the after-treatment system, particularly the diesel oxidation catalyst, the emissions of CO were significantly reduced by an average of 80%. However, in comparison to CO_2 emissions, CO emissions were very negligible.

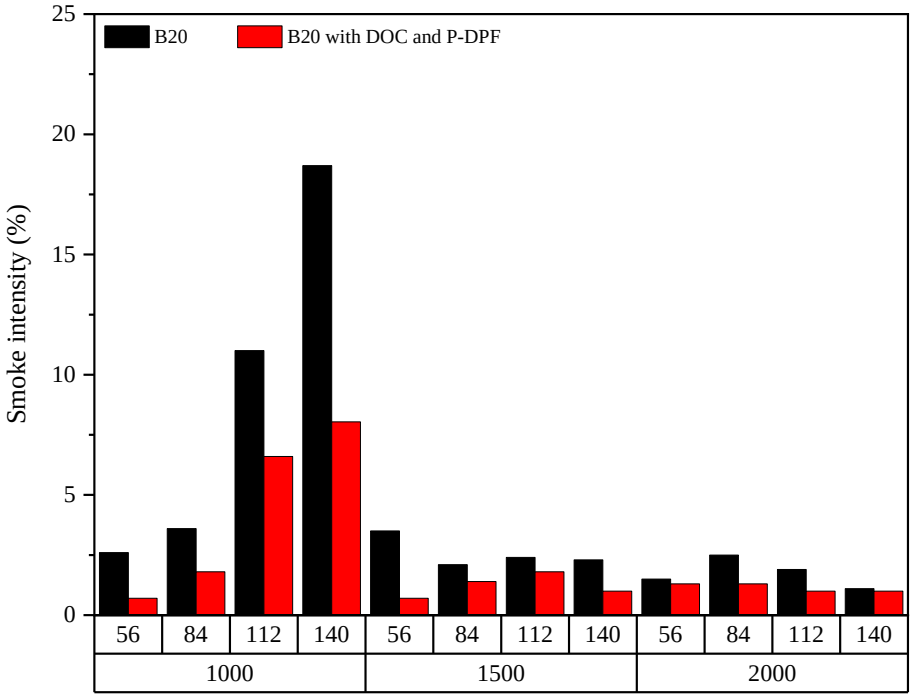

(a) Smoke Intensity

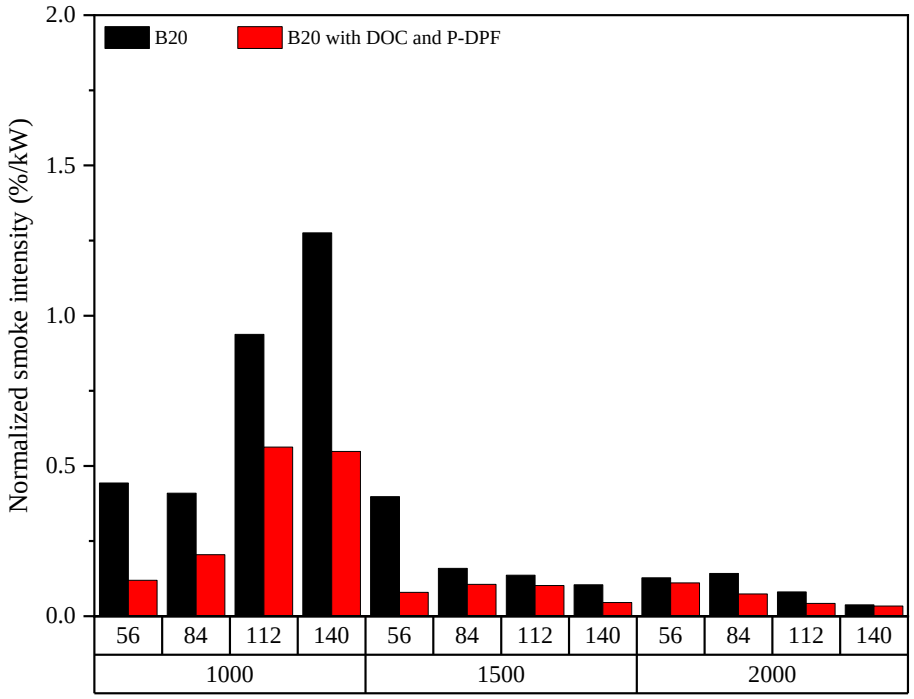

(b) Normalized smoke intensity

Figure 4-22 Observation of (a) smoke intensity and (b) smoke intensity with and without installing DOC and P-DPF

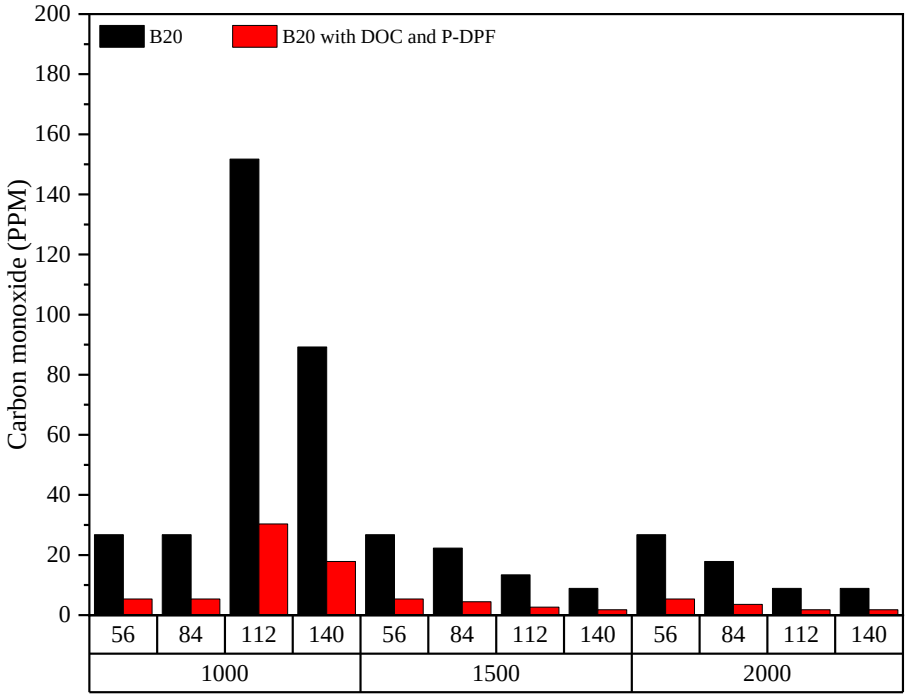

(a) Carbon monoxide

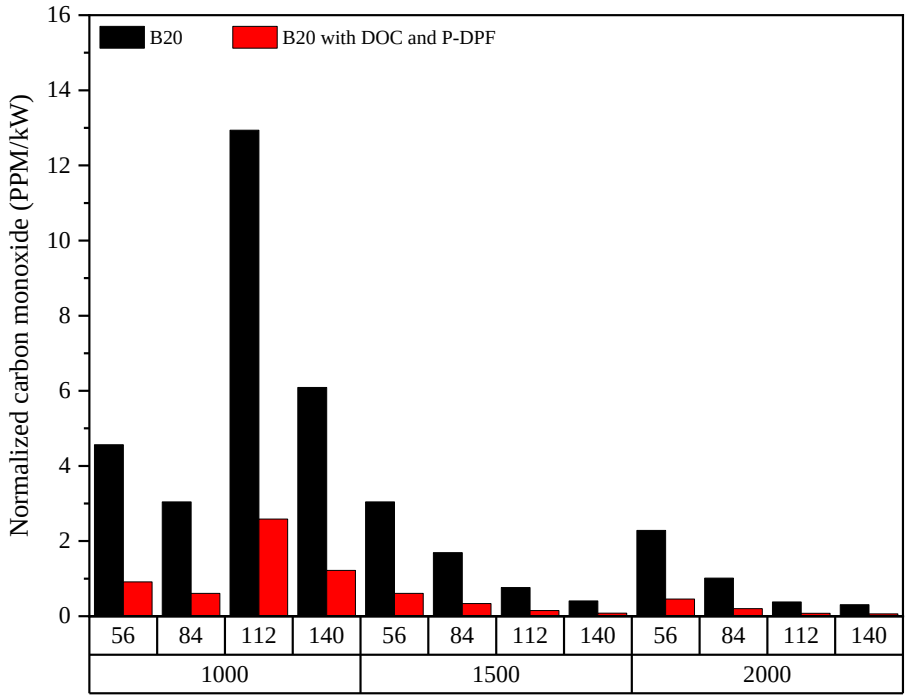

(b) Normalized carbon monoxide

Figure 4-23 Observation of (a) carbon monoxide and (b) normalized carbon monoxide with and without installing DOC and P-DPF

Figures 4-24 and **4-25** illustrate the variations in carbon dioxide (CO_2) and excess oxygen (O_2) emissions, including their normalized values, with respect to brake

power. The emissions of CO_2 exhibited an upward trend as engine loads increased while maintaining a constant speed. This can be attributed to the higher fuel injection rates associated with increasing engine loads. Conversely, the levels of excess oxygen in the exhaust stream decreased under the same engine conditions. This reduction can be attributed to the increased utilization of oxygen molecules during the combustion process, resulting in the production of CO_2. When the partial flow diesel particulate filter (P-DPF) was installed downstream of the diesel oxidation catalyst (DOC), the average increase in CO_2 emissions and decrease in O_2 levels were approximately 5% and 10%, respectively. This can be attributed to the oxidation of soot particles trapped on the partial filter by oxygen, resulting in the release of CO_2. Further insights into the soot oxidation process with oxygen can be obtained by analyzing the exhaust temperature.

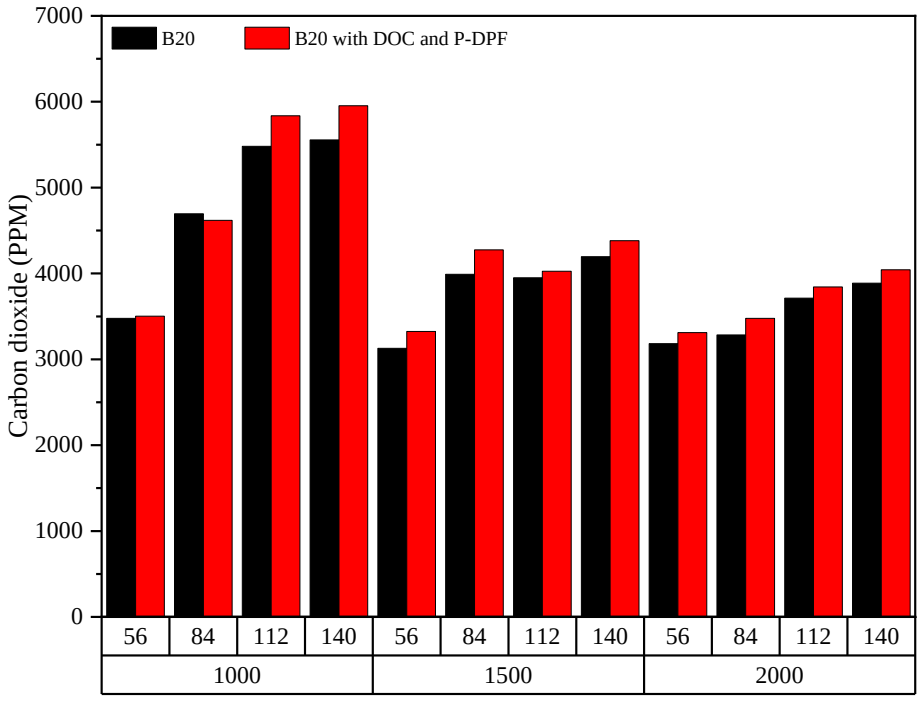

(a) Carbon dioxide

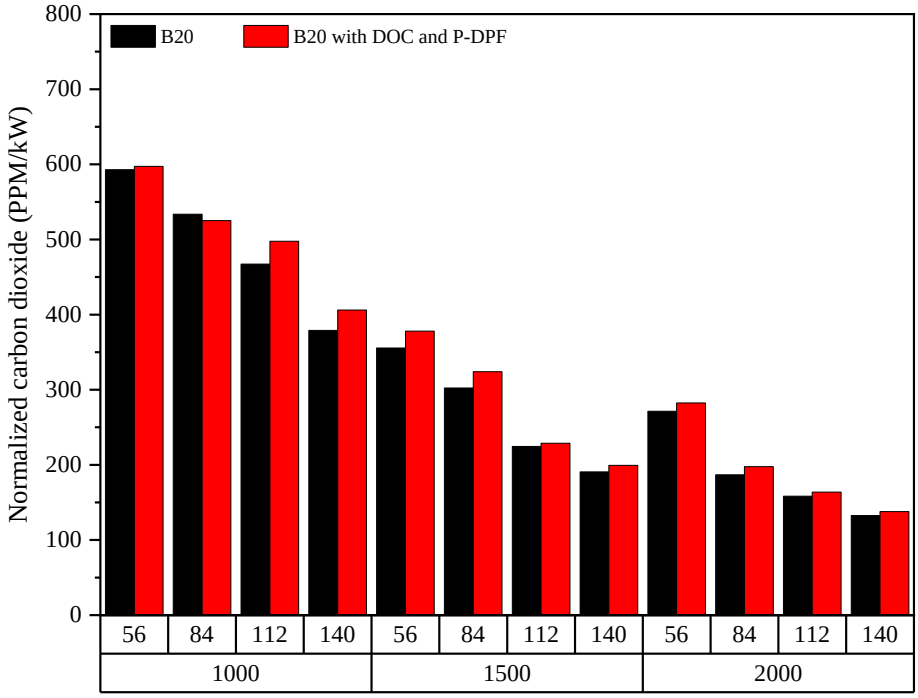

(b) Normalized carbon dioxide

Figure 4-24 Observation of (a) carbon dioxide and (b) normalized carbon dioxide with and without installing DOC and P-DPF

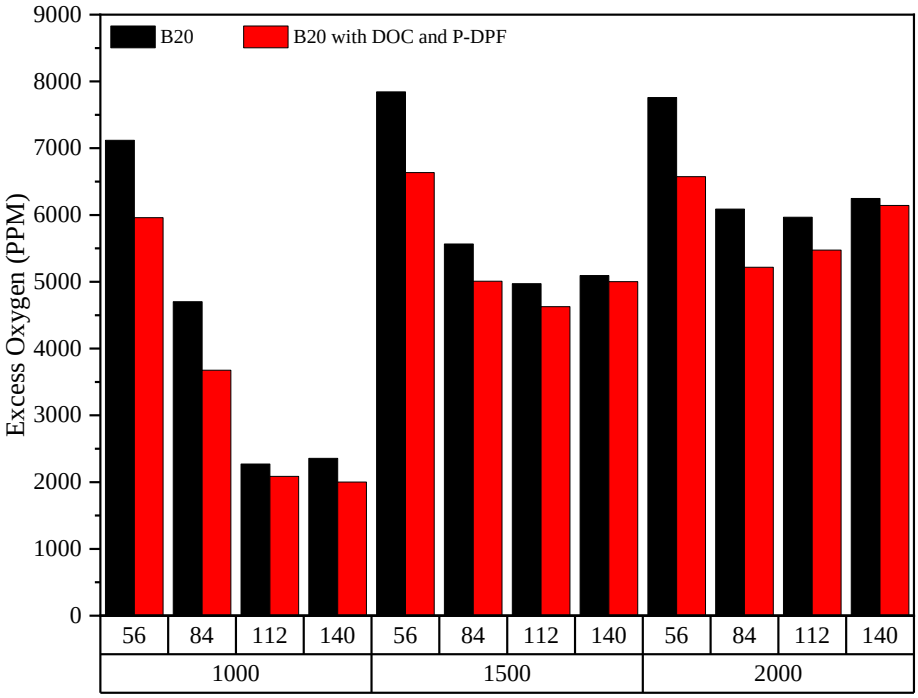

(a) Excess oxygen in the exhaust stream

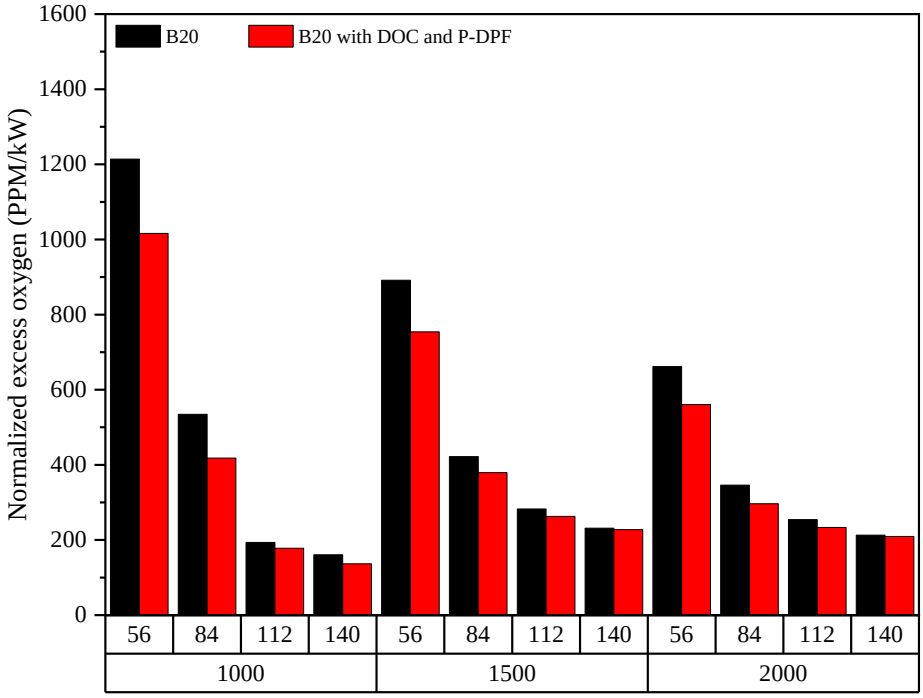

(b) Normalized excess oxygen in the exhaust stream

Figure 4-25 Observation of (a) excess oxygen and (b) normalized excess oxygen in the exhaust stream with and without installing DOC and P-DPF

Among the emissions released by diesel engines, nitrogen oxides (NOx) are considered highly hazardous. NOx consists predominantly of nitric oxide (NO), accounting for approximately 90-95% of the composition, while nitrogen dioxide (NO_2) constitutes around 5-10% of the mixture. The release of NOx emissions from diesel engines is influenced by factors such as combustion temperature, oxygen concentrations, and the fuel-air equivalent ratio [48]. **Figure 4-26** depicts the fluctuations in nitrogen monoxide (NO) emissions, along with their normalized values, in relation to brake power. NOx emissions exhibited an upward trend with increasing engine load due to the higher combustion temperatures associated with high engine loads. However, upon installing DOC and P-DPF, a significant average reduction of approximately 25% in NO emissions was observed at engine torques of 112 Nm and 140 Nm across all engine speeds. This reduction can be attributed to the potential conversion of NO to NO_2 within the diesel oxidation catalyst, which could subsequently contribute to the oxidation of soot within the partial filter.

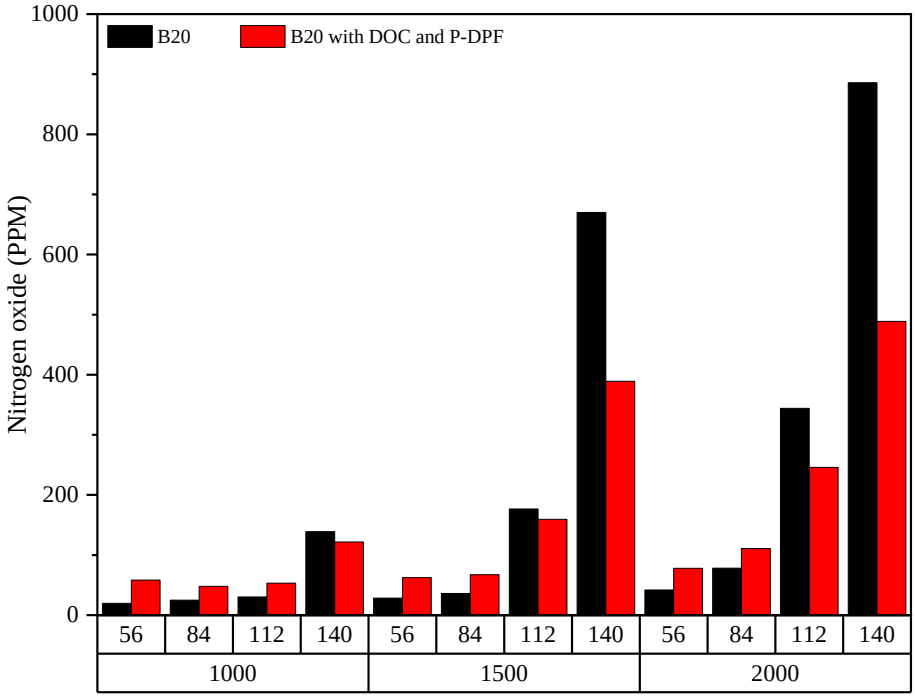

(a) Nitrogen monoxide

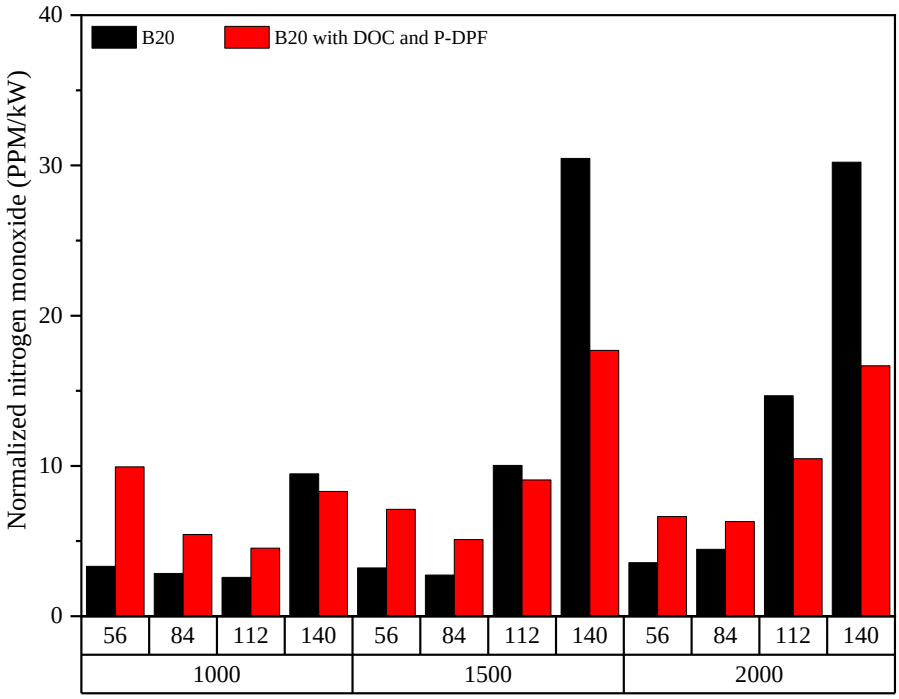

(b) Normalized nitrogen monoxide

Figure 4-26 Observation of (a) nitrogen monoxide and (b) normalized nitrogen monoxide with and without installing DOC and P-DPF

The measurement of exhaust temperature was conducted by placing a thermocouple at the exit of the exhaust manifold. **Figure 4-27** presents a comparison

of exhaust temperatures, considering both scenarios: with and without the implementation of the after-treatment system. The observed trend indicated an increase in exhaust temperatures as engine conditions, including load and speed, escalated. This correlation can be attributed to the elevated combustion temperature and pressure associated with higher engine loads and speeds. After the installation of the DOC and P-DPF, the exhaust temperature experienced an increase as a result of higher combustion pressure and increased fuel injection, enabling the engine to overcome the resistance imposed by the after-treatment system.

Based on the analysis of smoke intensity, nitrogen monoxide (NO), carbon dioxide (CO_2), oxygen (O_2), and exhaust temperature, it can be concluded that the continuous passive regeneration of soot through NO_2 occurred starting from an engine load of 84 Nm across all engine speeds. This regeneration process involved the oxidation of soot to CO_2 by NO_2, which took place even at relatively low temperatures of around 250°C [49]. Additionally, the oxidation of soot with O2 may take place at engine loads of 112 and 140 Nm, specifically at 1500 and 2000 rpm. According to Görsmann et al., the oxidation process of soot by O2 initiates gradually at temperatures as low as 350°C [37].

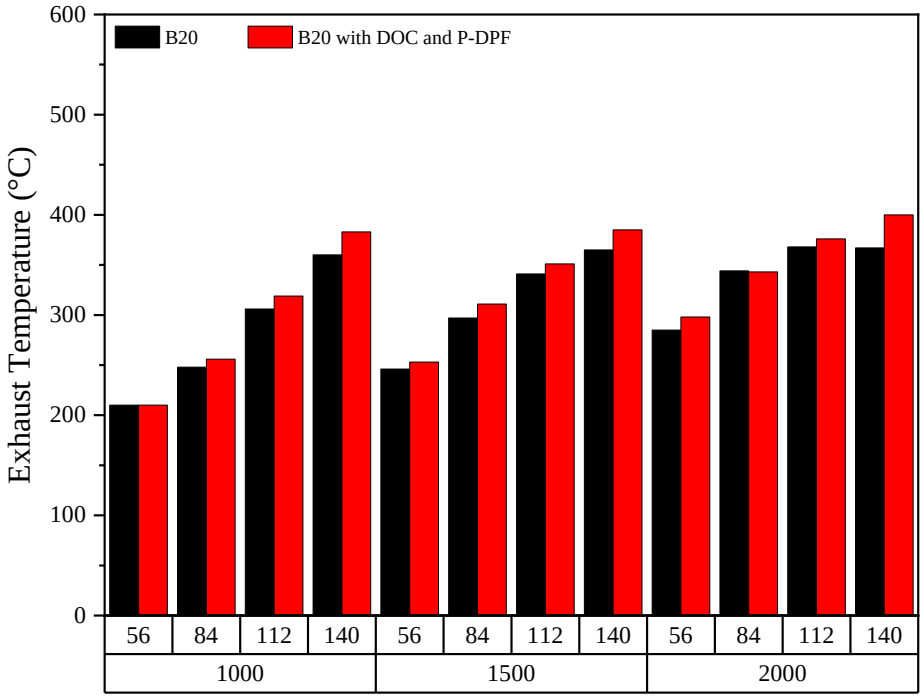

Figure 4-27 Observation of the exhaust temperature at the exit of the exhaust manifold with and without installing DOC and P-DPF

The condition with the highest smoke emissions, which occurred at 1000 rpm with 140 Nm, was selected for the visualization of collected soot on the paper filter. Scanning electron microscope (SEM) images at 10,000 magnifications were used to examine the morphology of the soot. **Figure 4-28** presents the results of this analysis. The use of B20 in combination with the after-treatment system resulted in the lowest particulate matter (PM) emissions from diesel engine combustion. The installation of P-DPF downstream of the DOC proved to be an effective approach for reducing PM emissions released into the atmosphere.

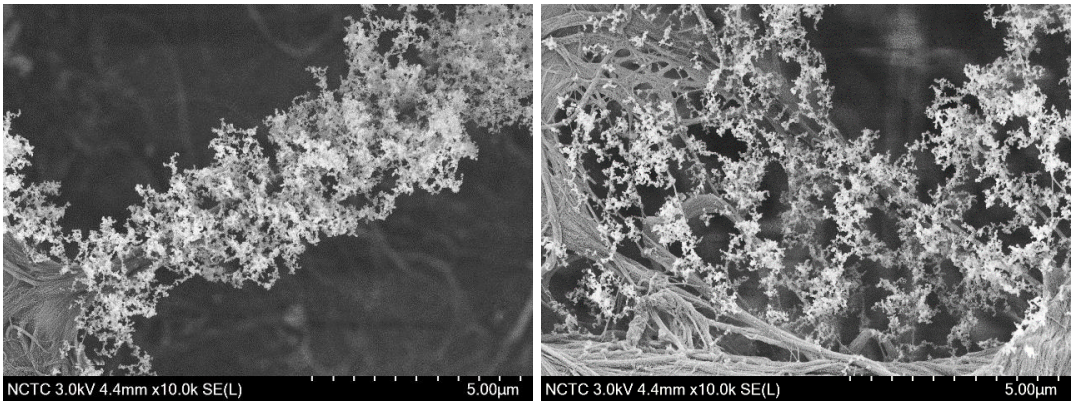

(a) B20 without DOC and P-DPF

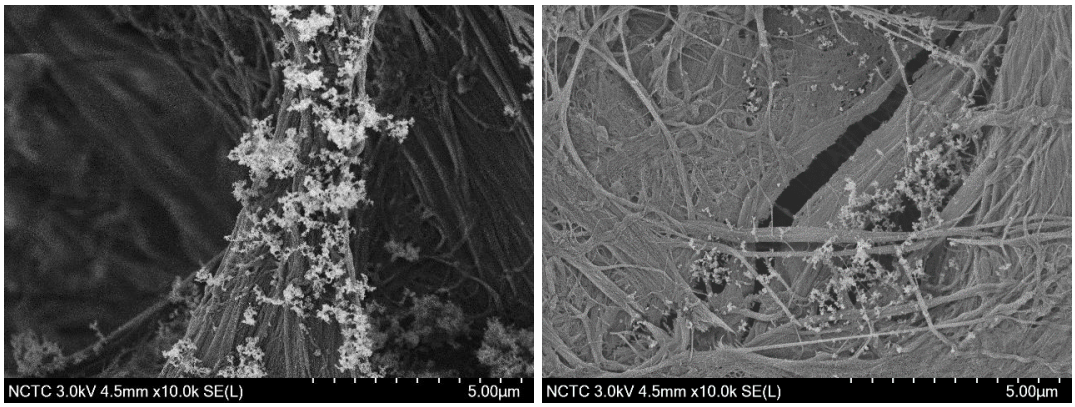

(b) B20 with DOC and P-DPF

Figure 4-28 Particulate matter accumulated on the paper filter with and without the after-treatment system at 1000 rpm and 140 Nm

4.3 Diesel vehicle test

The main focus of the diesel vehicle test was to compare the effectiveness of a ceria-coated partial-flow diesel particulate filter (P-DPF) to non-catalyzed P-DPF and without the usage of P-DPF in terms of its real-time and quantitative reduction of pollutant and gaseous emissions.

4.3.1 Real-time measurement of pollutant and gaseous emissions

This experiment was to evaluate the real-time performance of the non-catalyzed and ceria-catalyzed partial-flow diesel particulate filters (P-DPFs) in reducing emissions from the light-duty vehicle. **Figure 4-29 to 4-33** shows the temporal changes in particle counts (#/cm^3) and gaseous emissions (ppm) based on the diluted measurements, including three segments of urban driving cycles, one segment of extra driving, and the vehicle velocity profile. The instantaneous measurements of particle number (PN) showed that the use of P-DPF can reduce around 50% of PN and the ceria-catalyzed one showed better reduction performance than the non-catalyzed one. This is because the catalyst coating increases the number of contact points for soot trapping, making it more efficient at reducing particle number [50].

The study found that carbon monoxide (CO) and total hydrocarbon (THC) emissions exhibited a trend of higher emissions over urban routes and lower emissions over extra-urban routes. This is attributed to the stop-and-go nature of urban driving, which is more likely to produce CO and THC emissions compared to extra-urban driving. The diesel oxidation catalyst (DOC) was responsible for regulating the CO and THC emissions. However, the exhaust temperature did not reach high enough levels at low vehicle velocities to extract the CO and THC emissions efficiently, as it does under high-speed conditions. This is consistent with previous studies by Grigoratos et al., [51] and Qi et al., [52]. Moreover, the use of ceria-catalyzed P-DPF reduced THC and CO emissions on extra-urban routes. The continuous data plots of CO_2 and NO_x emissions for both the retrofitted and non-retrofitted vehicles showed that their emissions were primarily dependent on the driving conditions. CO_2 and NO_x emissions tended to be lower on urban routes and higher on extra-urban routes. During the extra-urban driving cycle, higher vehicle speeds and increased fuel injection resulted in higher carbon dioxide (CO_2) production than extra-urban driving at lower speeds. This finding suggests that elevated vehicle speeds contribute to greater CO_2 emissions, as

they necessitate higher fuel consumption rates. The observed increase in NOx concentration can be attributed to the elevated cylinder temperature and pressure experienced in the fuel-rich mode during acceleration. However, the use of DOC and P-DPF showed no significant impact on the emissions of CO_2 and NO_x.

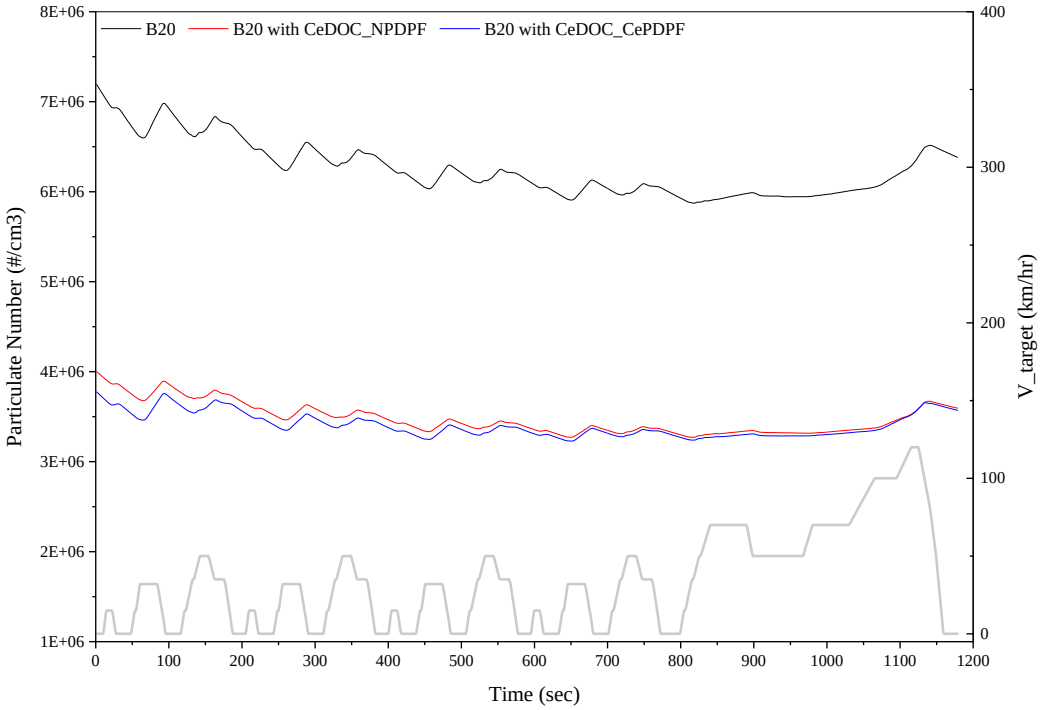

Figure 4-29 Real-time measurement of particulate number (PN) concentration

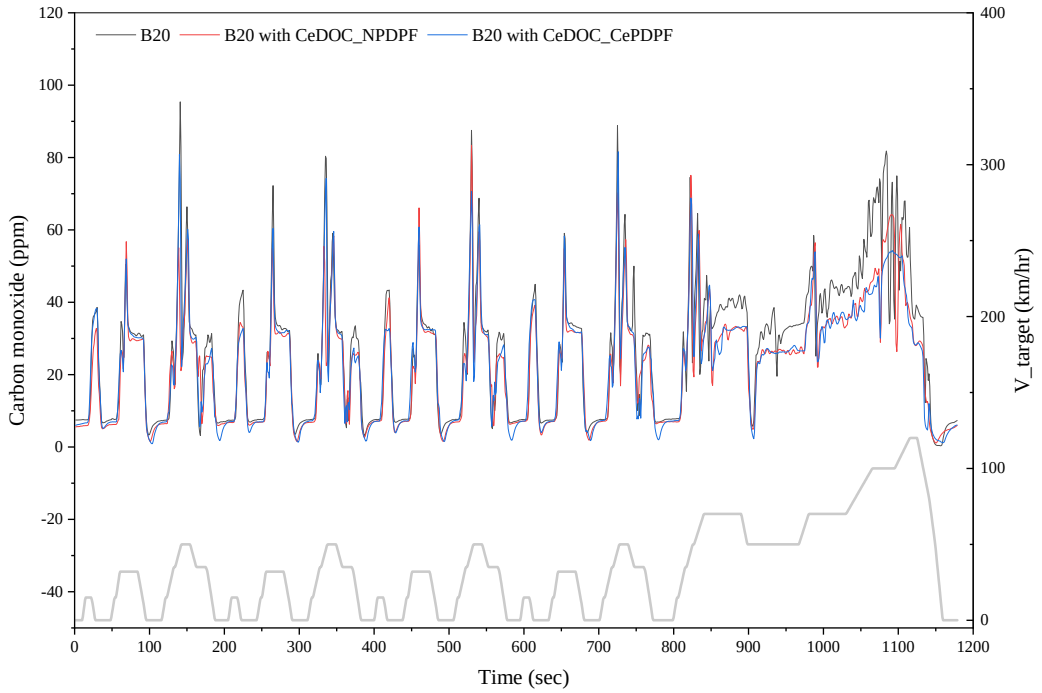

Figure 4-30 Real-time measurement of carbon monoxide (CO) emission

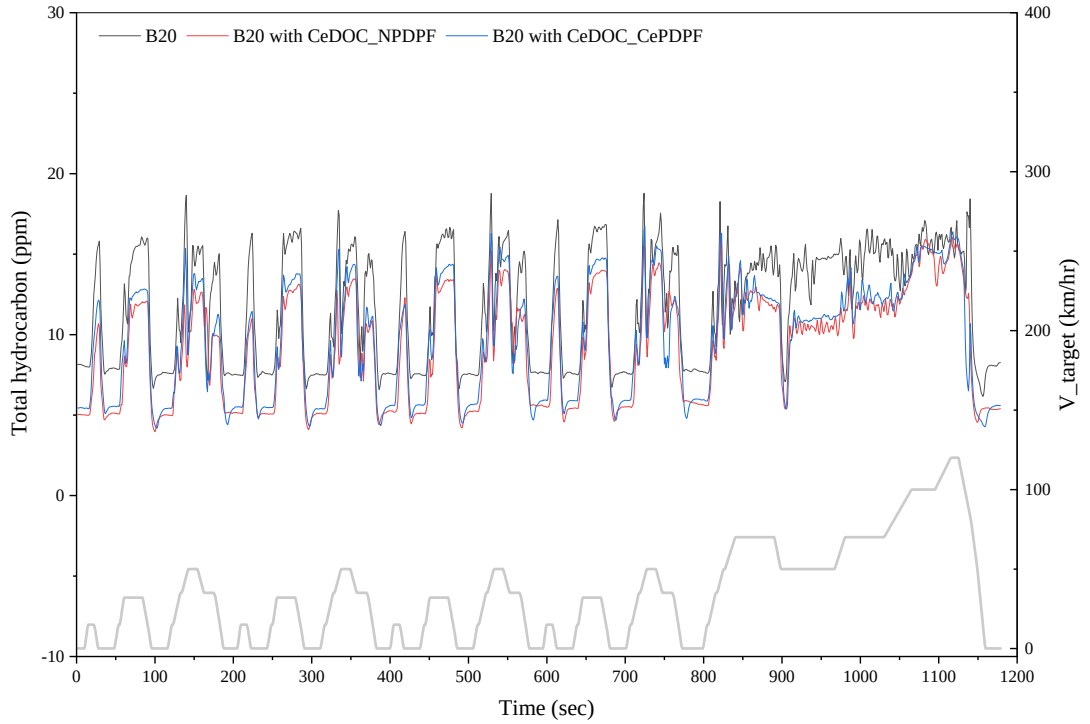

Figure 4-31 Real-time measurement of total hydrocarbon (THC) emissions

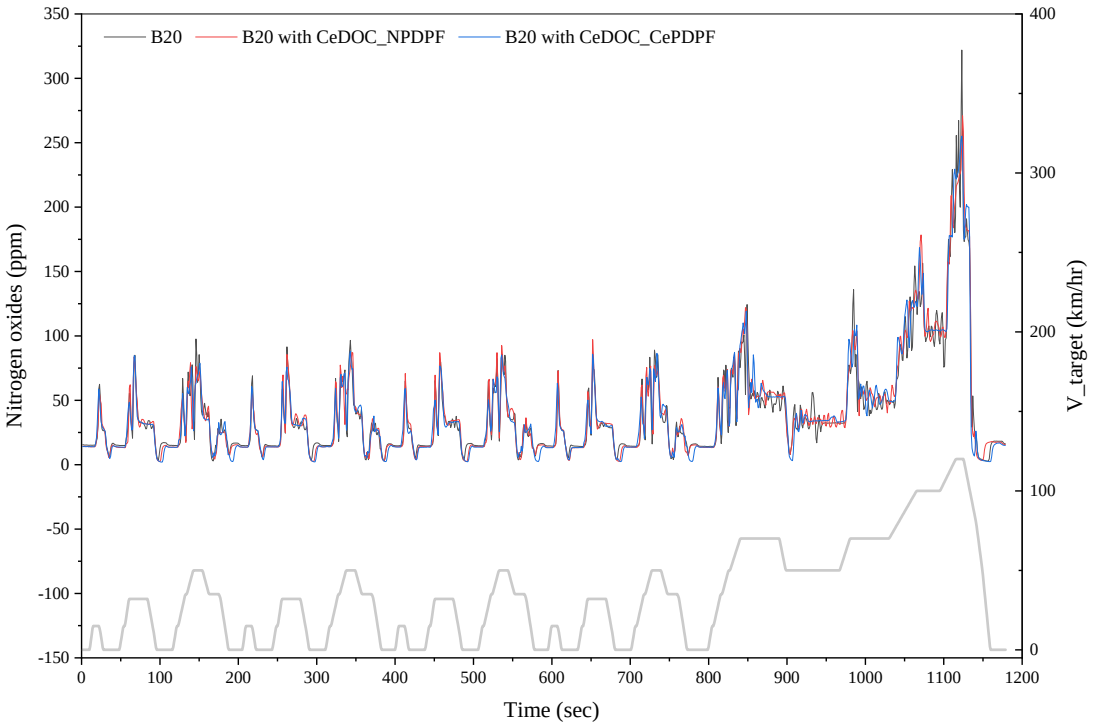

Figure 4-32 Real-time measurement of nitrogen oxides (NO_x) emissions

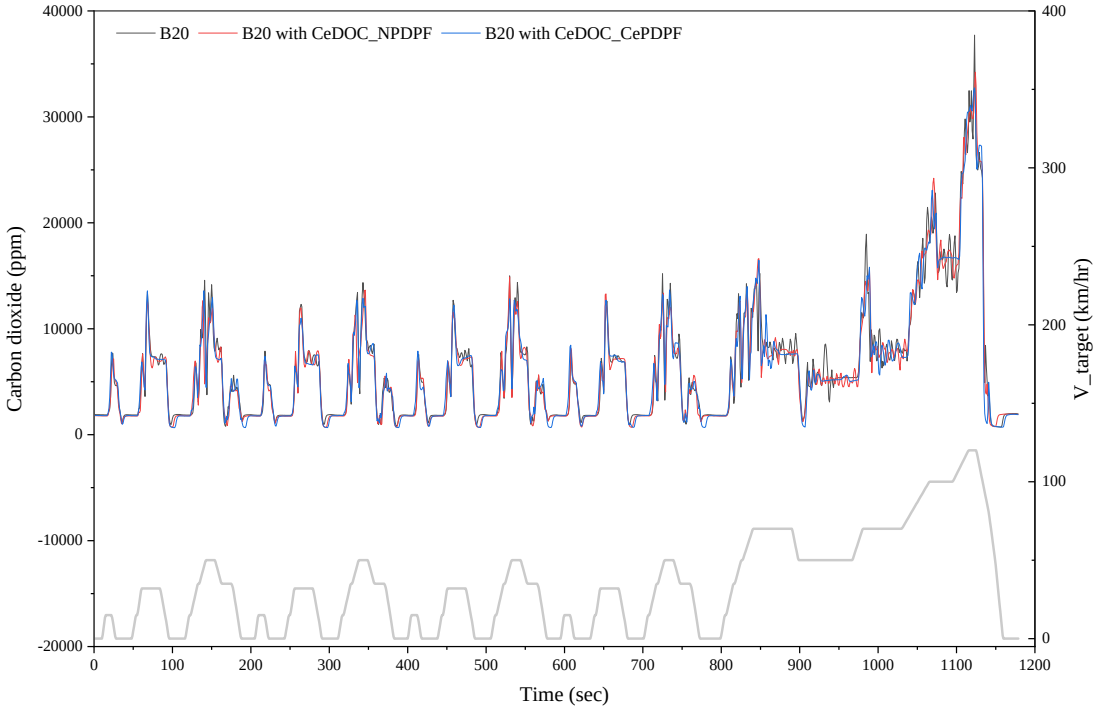

Figure 4-33 Real-time measurement of carbon dioxide (CO_2) emissions

4.3.2 Specific pollutant and gaseous emissions along the driving cycle

The investigation presents the results of regulated emissions reported in the specific mass unit of mg/km except for particle number concentration (#/km), which evaluates the consequences of non-catalyst and ceria catalyst coatings on the retrofit P-DPF in urban and extra-urban phases, as well as the mean values of both phases (total phase) of the new European driving cycle (NEDC). **Figure 4-34 (a)** presents the particulate mass (PM) emissions expressed in mg/km, which ranged from 14 to 40 mg/km and 8 to 25 mg/km during the urban and extra-urban phases, respectively. The PM emissions during the urban phase were higher compared to the extra-urban phase and this can be attributed to the lower vehicle speed which results in lower engine conditions that promote rich combustion. Conversely, higher vehicle speed during extra-urban driving led to leaner combustion and higher engine temperature, which can reduce PM emissions. However, all experiments performed under NEDC operation resulted in PM emissions below the Euro 4 emissions standard of 40 mg/km. When using the retrofitted partial filter, the non-catalyzed P-DPF can reduce PM emissions by 57%, while the ceria-coated P-DPF can achieve a reduction of 66%.

Figure 4-34 (b) displays the results of particle number (PN) concentration measurements during the regulatory test on the NEDC cycles. A comparable trend of

higher PN emissions was detected in the urban phase relative to the extra-urban phase. It is reasonable to assume that frequent start and stop operations under congested conditions during urban driving led to increased PN emissions. The lower PN emissions during the extra-urban phase may be due to the higher engine speed, which increased the in-cylinder temperature and improved the fuel-air mixing. The experiment's particle number (PN) measurement was higher than the $6x10^{11}$ #/km allowed by Euro 5 emission standards. This is probably because the P-DPF's filtration effectiveness was lower than that of the full-flow DPF, potentially as a result of the partial filter mechanism. Upon comparison with the outcomes obtained without the implementation of the P-DPF, it was observed that the utilization of the ceria P-DPF can reduce PN emissions by approximately 42%. Specifically, the PN concentration is reduced from approximately $1.09x10^{14}$ to $6.33x10^{13}$ by employing the ceria P-DPF.

Figures 4-35 (a) and (b) present the comparisons of total hydrocarbon (THC) and carbon monoxide (CO) emissions between the light-duty vehicle equipped with and without the after-treatment system. The results indicate that THC and CO emissions were significantly higher during the urban driving phase than during the extra-urban phase. This trend aligns with the findings of [53], which suggested that the operation of vehicles under low-speed conditions resulted in elevated concentrations of THC and CO emissions. However, the emissions of these two gases were recorded at relatively low levels compared to carbon dioxide emissions. The carbon monoxide emission levels were found to be within the limits set by Euro 3 regulations for urban driving (800 mg/km) and Euro 4/5 regulations for extra-urban driving (630 mg/km). When the after-treatment system, particularly the diesel oxidation catalyst (DOC), was used, the emissions of THC were found to decrease by up to 30%, and CO emissions decreased by up to 19%.

Figure 4-35 (c) illustrates the measurement of NO_x emissions from light-duty vehicles with and without the after-treatment system. It is observed that NO_x emissions exceed the Euro 4 and Euro 5 limits for both cases. This may be attributed to the engine control system being calibrated for conventional diesel vehicles and based on the NEDC operating setting. Additionally, while CO, THC, and PM emissions are effectively controlled to meet emissions regulations, it is possible for NO_x emissions to increase. The installation of the after-treatment system did not show any notable reduction in NOx emissions, indicating that additional examination is necessary for NOx

reduction. This could involve exploring the utilization of a catalytic converter, such as the selective catalytic reduction (SCR) system.

The measurements of CO_2 emissions in mg/km from both urban and extra-urban test cycles are presented in **Figure 4-35 (d)**. The urban phase showed CO_2 emissions of approximately 230,000 mg/km, while the extra-urban driving phase exhibited about 150,000 mg/km. The energy consumption was estimated based on fuel economy, calculated from exhaust emissions' carbon balance. This resulted in a similar trend of energy consumption at around 250 MJ/100 km. Upon examination of the results, it was found that the installation of the retrofit ceria-catalyzed partial filter did not result in any significant changes in fuel consumption as well as CO_2 emissions. Based on the CO_2 emission measurements, it is possible to hypothesize that the passive regeneration of particulate matter within the catalyzed partial filter may have been slow or not happened by the limited duration of the experiments.

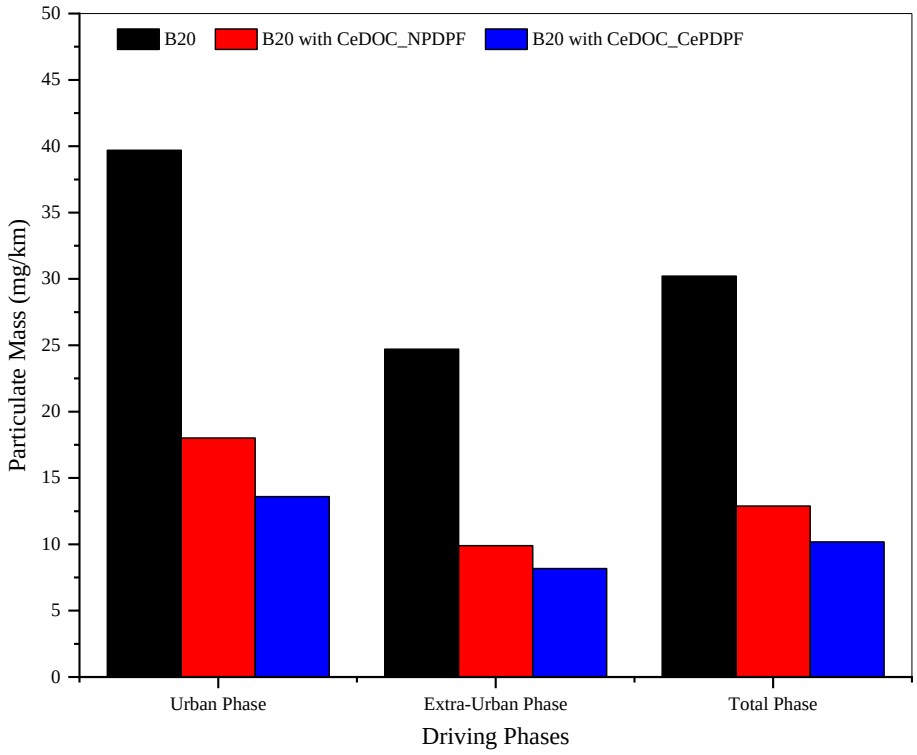

(a) Particulate mass (PM) emissions

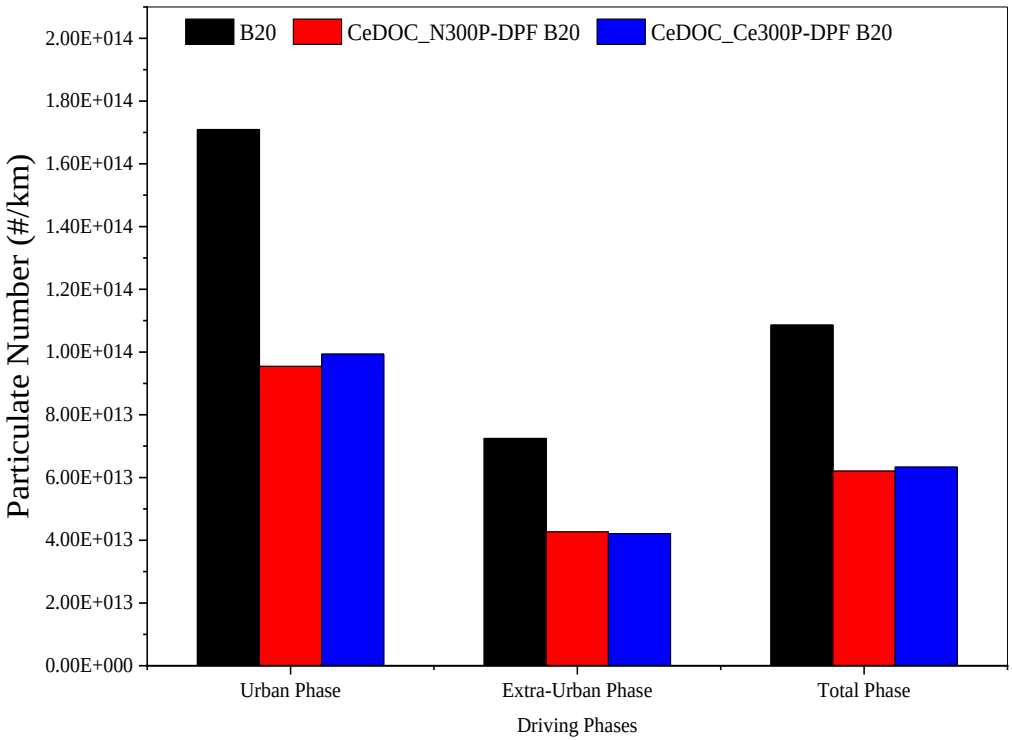

(b) Particulate number (PN) concentration

Figure 4-34 Comparison of (a) PM and (b) PN emissions from diesel vehicle

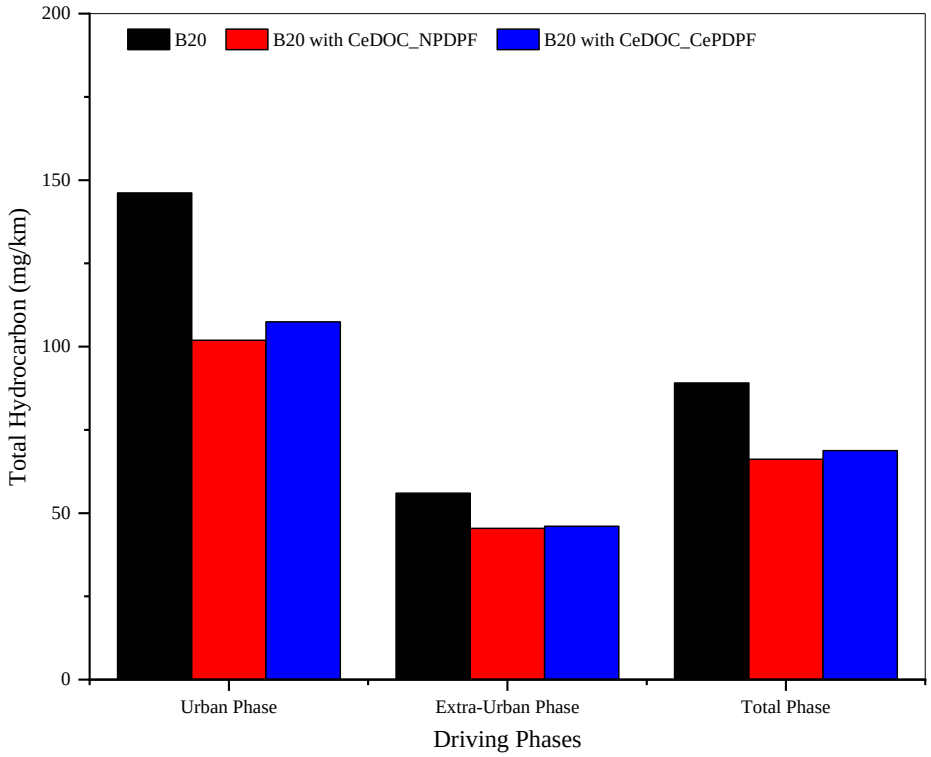

(a) Total hydrocarbon (THC) emissions

(b) Carbon monoxide (CO) emissions

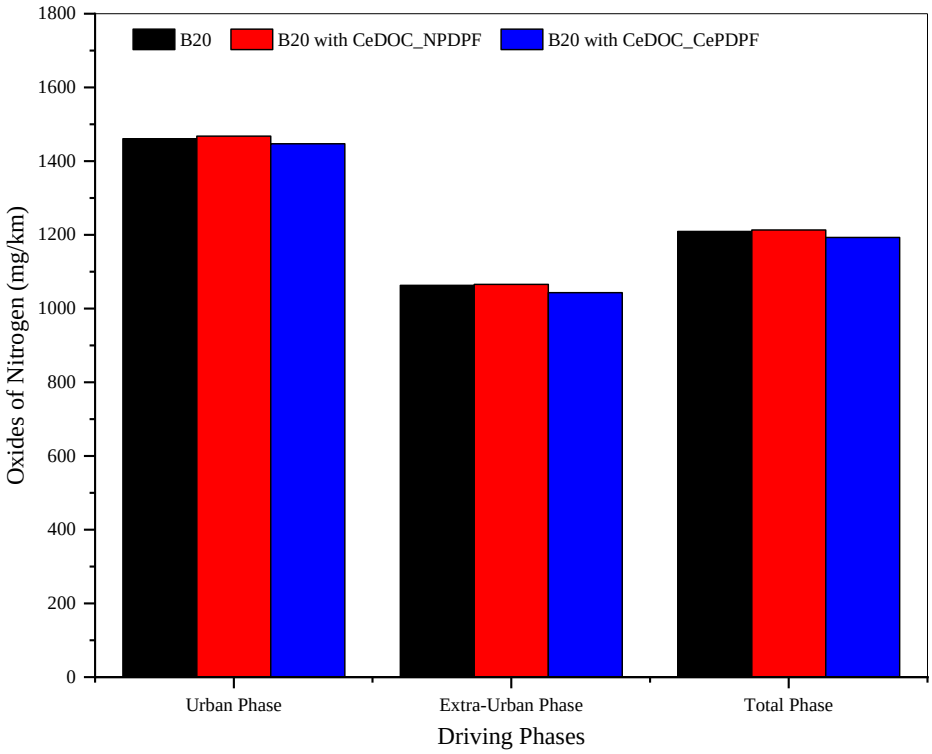

(c) Oxides of nitrogen (NO_x) emissions

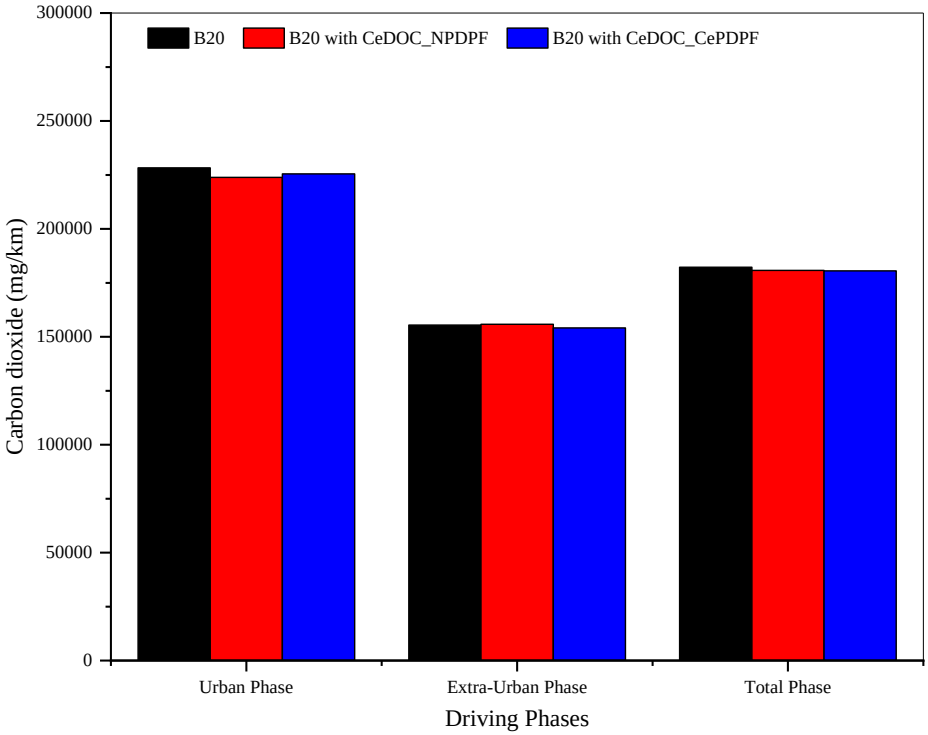

(d) Carbon dioxide emissions (CO_2)

Figure 4-35 Comparisons of (a) THC, (b) CO, (c) NO_x, and CO_2 emissions from vehicle

4.3.3 Impact of ceria catalyst coating on soot microstructure

Scanning electron microscopy (SEM) was utilized to investigate the impact of the ceria catalytic partial filter on the microstructure of particulate matter collected on the paper filter, with magnifications of 10,000x and 50,000x. **Figure 4-36** illustrates the 10,000x magnification of PM by contrasting the use of non-catalytic and ceria-catalytic P-DPF. The results revealed that the accumulation of agglomerated soot reduced when P-DPF was used, and the ceria catalyst exhibited a higher reduction in the accumulation of soot. Additionally, **Figure 4-37** displays the 50,000x magnification of PM, where non-catalyzed P-DPF reduced the soot aggregate build-up, while the use of ceria catalyst demonstrated the most significant reduction in the size of the soot aggregate.

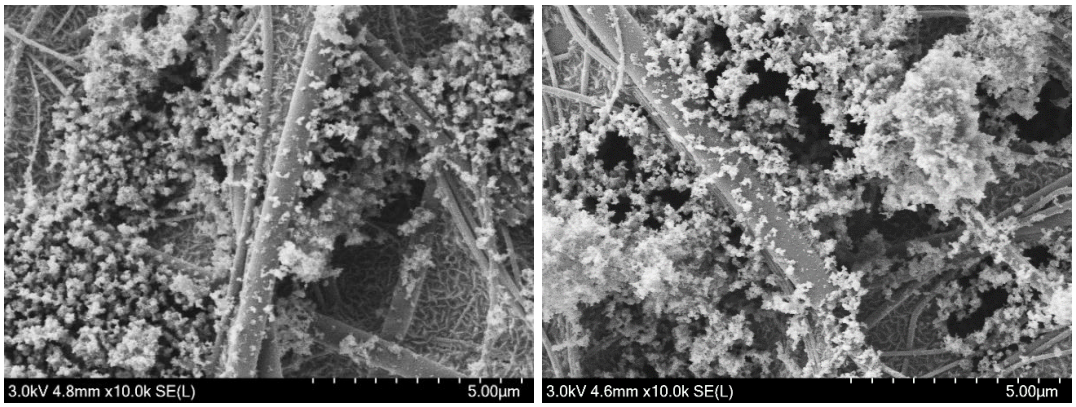

(a) B20

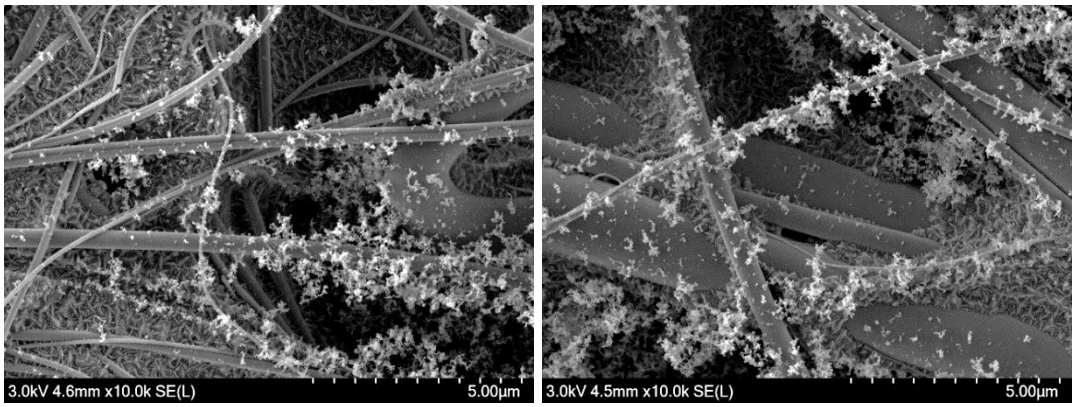

(b) B20 with CeDOC_NPDPF

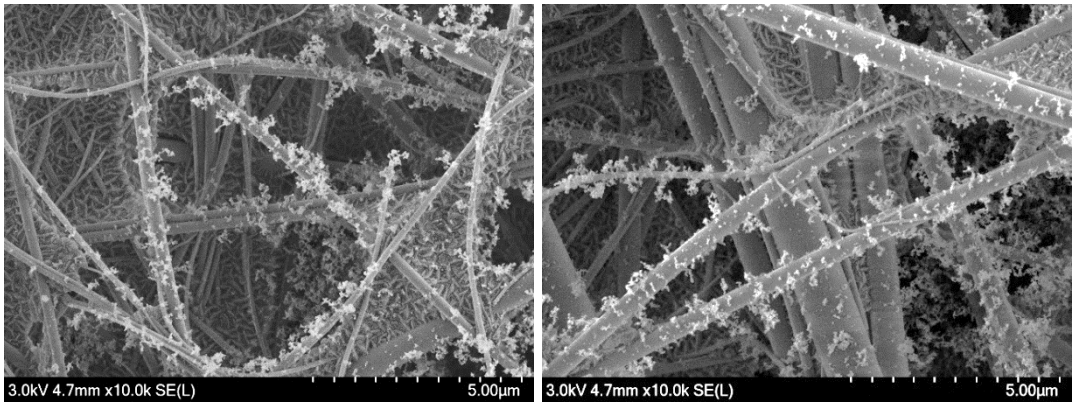

(c) B20 with CeDOC_CePDPF

Figure 4-36 10,000x magnification of particulate matter collected on the paper filter under urban driving cycles.

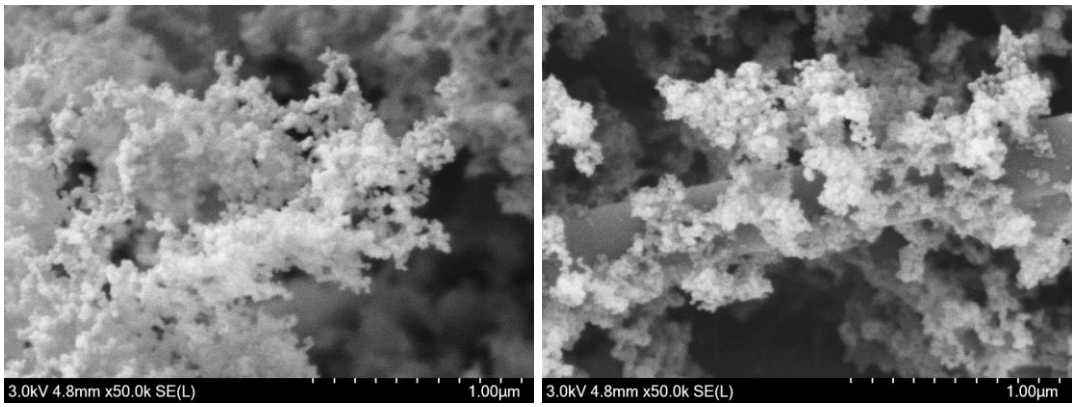

(a) B20

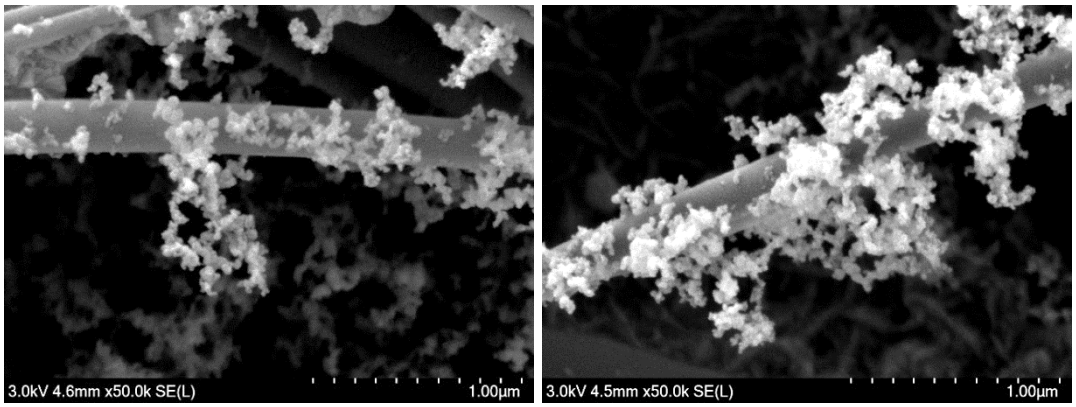

(b) B20 with CeDOC_NPDPF

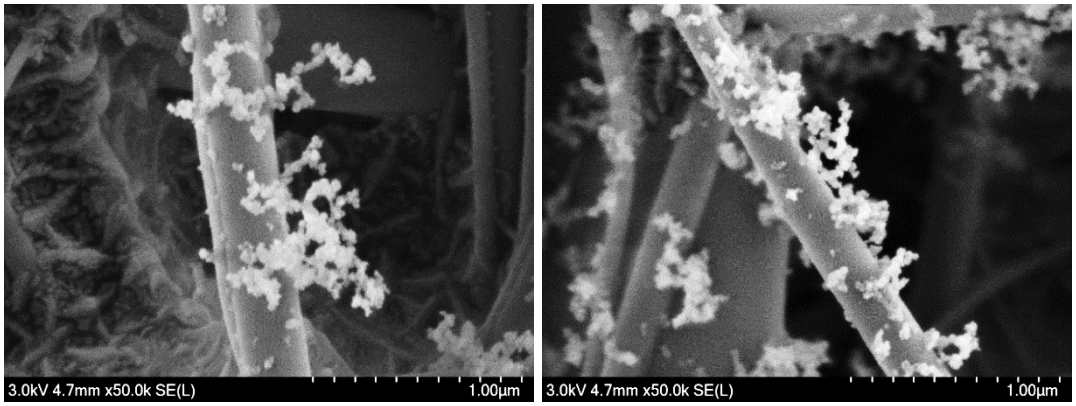

(c) B20 with CeDOC_CePDPF

Figure 4-37 50,000x magnification of particulate matter collected on the paper filter under urban driving cycles

CHAPTER 5

CONCLUSIONS

The aim of this study was to investigate the properties of particulate matter (PM) produced from the combustion of B20 biodiesel, specifically focusing on its chemical composition, morphology, and nanostructure. The research was conducted without the implementation of an exhaust after-treatment system. Initially, energy-dispersive spectroscopy (EDS) was employed to determine the elemental composition of the PM. The analysis indicated that the majority of the PM consisted of carbon (88%) and oxygen (10%). Subsequently, the morphology of the PM was examined using transmission electron microscopy (TEM) and ImageJ software, allowing for the measurement of individual primary particle sizes ranging from 10 to 55 nm, with an average diameter of 29 nm. Moreover, TEM and X-ray diffraction (XRD) were utilized to analyze the nanostructure of the PM, providing valuable insights into parameters such as skeletonized fringe length, interlayer spacing, and carbon density within one cubic centimeter.

When considering the combustion characteristics, a comparative analysis of the obtained data with and without the implementation of an after-treatment system demonstrated notable effects. The combustion in-cylinder pressure, net heat release rate (NHRR), and cumulative net heat release (CNHR) exhibited an increase in the presence of DOC and P-DPF. This increase can be attributed to the elevated temperature within the combustion chamber induced by the backpressure generated by the after-treatment system. The retention of exhaust gases within the chamber contributed to the overall thermal energy of the system, resulting in these enhancements. Moreover, a prolonged ignition delay was observed at an engine speed of 1000 rpm. This delay can be ascribed to the influence of backpressure on the residual gas fraction present in the combustion chamber. The interaction of backpressure with the residual gas fraction may affect the dilution effect of fuel and air, leading to an extended ignition delay and increased heat losses under these engine conditions. However, it is important to note that these energy or heat losses can be effectively recuperated as the engine speed increases.

The engine performance revealed that the indicated specific fuel consumption (ISFC) and indicated specific energy consumption (ISEC) decreased while the indicated

thermal efficiency (ITE) increased by an average of approximately 13% after the installation of the DOC and P-DPF. This can be contributed to the enhanced indicated work or power, despite the same energy input, resulting from the backpressure generated by the after-treatment system under consistent engine conditions. However, brake-specific fuel consumption (BSFC) and brake-specific energy consumption (BSEC) experienced an average increase of around 1%. Additionally, the brake thermal efficiency (BTE) decreased due to the backpressure generated by the after-treatment system. Hence, the installation of the DOC and P-DPF had minimal influence on fuel consumption, as indicated by insignificant changes in brake-specific fuel consumption (BSFC), brake-specific energy consumption (BSEC), and brake thermal efficiency (BTE). This can be attributed to the relatively modest increase in backpressure, ranging from 0.2 to 2.25 kPa.

The emissions analysis revealed substantial reductions in smoke intensity, averaging around 65%, after implementing the partial flow filter. The reduction in soot was visually confirmed using scanning electron microscopy (SEM) on the paper filter. Furthermore, nitrogen oxide (NO) emissions experienced a decrease of approximately 25% at engine torques of 112 Nm and 140 Nm across three engine speeds. This reduction can be attributed to the conversion of NO to nitrogen dioxide (NO2) as the exhaust gases passed through the diesel oxidation catalyst (DOC), which aids in the oxidation of soot within the particulate filter (P-DPF). Moreover, there was a 5% increase in carbon dioxide (CO2) emissions, accompanied by a 10% decrease in excess oxygen levels. This can be explained by the oxidation of soot captured on the partial filter through the combined action of oxygen and NO2, leading to the release of CO2. These reactions typically occur when the exhaust temperature reaches approximately 350-400°C under engine torques of 112 Nm and 140 Nm across the specified range of engine speeds.

Additionally, the diesel vehicle test was performed on a chassis dynamometer using the New European Driving Cycle to evaluate the effectiveness of a ceria-coated particulate filter (P-DPF) in reducing emissions, both in real-time and specific phase measurements. The findings indicated that the non-catalyzed P-DPF achieved a 57% reduction in particulate matter (PM) emissions. In contrast, the ceria-coated P-DPF demonstrated an even higher reduction of 66%. The improved performance of the ceria-coated P-DPF could be attributed to the catalyst coating, which increased the

number of contact points available for soot trapping. This enhanced the efficiency of particle emission reduction. Moreover, the utilization of ceria P-DPF could also reduce PN emissions by approximately 42%. However, it was found that the installation of the retrofit partial filter did not result in any significant changes in CO_2 and NO_x emissions. It was possible to hypothesize that the continuous passive regeneration of particulate matter within the partial filter may have been slow or not occurred due to the limited duration of the experiments and the absence of load conditions on the vehicles.

REFERENCES

[1] M. Bharathidasan, V. Indragandhi, V. Suresh, M. Jasiński, and Z. Leonowicz, "A review on electric vehicle: Technologies, energy trading, and cyber security," *Energy Reports*, vol. 8. Elsevier Ltd, pp. 9662–9685, Nov. 01, 2022. doi: 10.1016/j.egyr.2022.07.145.

[2] M. Tran, D. Banister, J. D. K. Bishop, and M. D. McCulloch, "Realizing the electric-vehicle revolution," *Nature Climate Change*, vol. 2, no. 5. pp. 328–333, May 2012. doi: 10.1038/nclimate1429.

[3] Z. Li, A. Khajepour, and J. Song, "A comprehensive review of the key technologies for pure electric vehicles," *Energy*, vol. 182. Elsevier Ltd, pp. 824–839, Sep. 01, 2019. doi: 10.1016/j.energy.2019.06.077.

[4] J. A. Sanguesa, V. Torres-Sanz, P. Garrido, F. J. Martinez, and J. M. Marquez-Barja, "A review on electric vehicles: Technologies and challenges," *Smart Cities*, vol. 4, no. 1. MDPI, pp. 372–404, Mar. 01, 2021. doi: 10.3390/smartcities4010022.

[5] S. Z. Rajper and J. Albrecht, "Prospects of electric vehicles in the developing countries: A literature review," *Sustainability (Switzerland)*, vol. 12, no. 5, Mar. 2020, doi: 10.3390/su12051906.

[6] S. Habib, M. M. Khan, F. Abbas, L. Sang, M. U. Shahid, and H. Tang, "A Comprehensive Study of Implemented International Standards, Technical Challenges, Impacts and Prospects for Electric Vehicles," *IEEE Access*, vol. 6. Institute of Electrical and Electronics Engineers Inc., pp. 13866–13890, Mar. 05, 2018. doi: 10.1109/ACCESS.2018.2812303.

[7] I. energy Agency, "Statistics report Key World Energy Statistics 2021," 2021.

[8] S. Kamalad, "Energy Outlook and Energy Saving Potential in East Asia 2020," ERIA, 2020.

[9] C. ChooChuay *et al.*, "Impacts of PM2.5 sources on variations in particulate chemical compounds in ambient air of Bangkok, Thailand," *Atmos Pollut Res*, vol. 11, no. 9, pp. 1657–1667, Sep. 2020, doi: 10.1016/j.apr.2020.06.030.

[10] S. Steiner, C. Bisig, A. Petri-Fink, and B. Rothen-Rutishauser, "Diesel exhaust: current knowledge of adverse effects and underlying cellular mechanisms," *Archives of Toxicology*, vol. 90, no. 7. Springer Verlag, pp. 1541–1553, Jul. 01, 2016. doi: 10.1007/s00204-016-1736-5.

[11] D. R. Tree and K. I. Svensson, “Soot processes in compression ignition engines,” *Progress in Energy and Combustion Science*, vol. 33, no. 3. pp. 272–309, Jun. 2007. doi: 10.1016/j.pecs.2006.03.002.

[12] J. P. A. Neeft, T. X. Nijhuis, E. Smakman, M. Makkee, and J. A. Moulijn, “Kinetics of the oxidation of diesel soot,” 1997.

[13] P. Eastwood, “Particulate Emissions from Vehicles,” 2008.

[14] O. I. Smith, “FUNDAMENTALS OF SOOT FORMATION IN FLAMES WITH APPLICATION TO DIESEL ENGINE PARTICULATE EMISSIONS.”

[15] D. B. Kittelson, “ENGINES AND NANOPARTICLES: A REVIEW,” 1998.

[16] M. Matti Maricq, “Chemical characterization of particulate emissions from diesel engines: A review,” *Journal of Aerosol Science*, vol. 38, no. 11. Elsevier Ltd, pp. 1079–1118, 2007. doi: 10.1016/j.jaerosci.2007.08.001.

[17] M. Si, Q. Cheng, J. Song, Y. Liu, M. Tao, and C. Lou, “Study on inversion of morphological parameters of soot aggregates in hydrocarbon flames,” *Combust Flame*, vol. 183, pp. 261–270, 2017, doi: 10.1016/j.combustflame.2017.05.019.

[18] V. Fernandez-Alos, J. K. Watson, R. vander Wal, and J. P. Mathews, “Soot and char molecular representations generated directly from HRTEM lattice fringe images using Fringe3D,” *Combust Flame*, vol. 158, no. 9, pp. 1807–1813, Sep. 2011, doi: 10.1016/j.combustflame.2011.01.003.

[19] M. B. Vázquez-Santos, E. Geissler, K. László, J. N. Rouzaud, A. Martínez-Alonso, and J. M. D. Tascón, “Comparative XRD, Raman, and TEM study on graphitization of PBO-derived carbon fibers,” *Journal of Physical Chemistry C*, vol. 116, no. 1, pp. 257–268, Jan. 2012, doi: 10.1021/jp2084499.

[20] T. Ishiguro, Y. Takatori, and K. Akihama, “Brief Communication Microstructure of Diesel Soot Particles Probed by Electron Microscopy: First Observation of Inner Core and Outer Shell,” 1997.

[21] L. Pahalagedara *et al.*, “Structure and oxidation activity correlations for carbon blacks and diesel soot,” in *Energy and Fuels*, Nov. 2012, pp. 6757–6764. doi: 10.1021/ef301331b.

[22] H. M. Oo, P. Karin, C. Charoenphonphanich, N. Chollacoop, and K. Hanamura, “Physicochemical characterization of direct injection Engines’s soot using TEM, EDS, X-ray diffraction and TGA,” *Journal of the Energy Institute*, vol. 96, pp. 181–191, Jun. 2021, doi: 10.1016/j.joei.2021.03.009.

[23] Y. Zhang, D. Lou, Z. Hu, and P. Tan, “Experimental investigation into the number, micromorphology, functional group composition, and oxidation activity of particles from diesel engine with biodiesel blend,” *Fuel*, vol. 289, Apr. 2021, doi: 10.1016/j.fuel.2020.119902.

[24] P. Karin, J. Boonsakda, K. Siricholathum, E. Saenkhumvong, C. Charoenphonphanich, and K. Hanamura, “MORPHOLOGY AND OXIDATION KINETICS OF CI ENGINE’S BIODIESEL PARTICULATE MATTERS ON CORDIERITE DIESEL PARTICULATE FILTERS USING TGA,” *International Journal of Automotive Technology*, vol. 18, no. 1, pp. 31–40, 2017, doi: 10.1007/s12239–017–0003–y.

[25] P. Verma *et al.*, “Influence of fuel-oxygen content on morphology and nanostructure of soot particles,” *Combust Flame*, vol. 205, pp. 206–219, Jul. 2019, doi: 10.1016/j.combustflame.2019.04.009.

[26] L. A. Raman, B. Deepanraj, S. Rajakumar, and V. Sivasubramanian, “Experimental investigation on performance, combustion and emission analysis of a direct injection diesel engine fuelled with rapeseed oil biodiesel,” *Fuel*, vol. 246, pp. 69–74, Jun. 2019, doi: 10.1016/j.fuel.2019.02.106.

[27] S. Baweja, A. Trehan, and R. Kumar, “Combustion, performance, and emission analysis of a CI engine fueled with mustard oil biodiesel blended in diesel fuel,” *Fuel*, vol. 292, May 2021, doi: 10.1016/j.fuel.2021.120346.

[28] R. Karami, M. G. Rasul, M. M. K. Khan, and M. Mahdi Salahi, “Experimental and computational analysis of combustion characteristics of a diesel engine fueled with diesel-tomato seed oil biodiesel blends,” *Fuel*, vol. 285, Feb. 2021, doi: 10.1016/j.fuel.2020.119243.

[29] P. Karin *et al.*, “EFFECT OF BIODIESEL ON COMPRESSION IGNITION ENGINE’S COMBUSTION BEHAVIOR AND PARTICLE EMISSION,” *Journal of Research and Applications in Mechanical Engineering*, vol. 8, no. 2, pp. 92–100, 2020, doi: 10.14456/jrame.2020.11.

[30] V. Nadanakumar, S. Jenoris Muthiya, T. Prudhvi, S. Induja, R. Sathyamurthy, and V. Dharmaraj, “Experimental investigation to control HC, CO & NOx emissions from diesel engines using diesel oxidation catalyst,” in *Materials Today: Proceedings*, Elsevier Ltd, 2020, pp. 434–440. doi: 10.1016/j.matpr.2020.11.964.

[31] Y. Liang *et al.*, “Active oxygen-promoted NO catalytic on monolithic Pt-based diesel oxidation catalyst modified with Ce,” *Catal Today*, pp. 64–72, May 2019, doi: 10.1016/j.cattod.2018.06.008.

[32] S. Liu, X. Wu, D. Weng, and R. Ran, “Ceria-based catalysts for soot oxidation: A review,” *Journal of Rare Earths*, vol. 33, no. 6. Chinese Society of Rare Earths, pp. 567–590, Jun. 01, 2015. doi: 10.1016/S1002-0721(14)60457-9.

[33] M. K. Khair, “A Review of Diesel Particulate Filter Technologies.”

[34] B. Guan, R. Zhan, H. Lin, and Z. Huang, “Review of the state-of-the-art of exhaust particulate filter technology in internal combustion engines,” *Journal of Environmental Management*, vol. 154. Academic Press, pp. 225–258, May 01, 2015. doi: 10.1016/j.jenvman.2015.02.027.

[35] Dipl.-I. R. Brück, Dipl.-I. P. Hirth, and Dipl.-I. R. Konieczny, “Der PM-Metalit™; Erfahrungen mit dem Nebenstrom Partikelfiltersystem hinsichtlich Reduzierung von Partikelanzahl und-Masse bei PKW-und LKW-Anwendungen The PM-Metalit™; Experience with the bypass-flow particulate trap with regard to the reduction of particulate number and-mass for passenger car and truck applications.”

[36] “Emissions Comparisons from Alternative Fuel Buses and Diesel Buses with a Chassis Dynamometer Testing Facility,” 1997. [Online]. Available: https://pubs.acs.org/sharingguidelines

[37] C. Görsmann, “Catalytic coatings for active and passive diesel particulate filter regeneration,” *Monatshefte fur Chemie*, vol. 136, no. 1. pp. 91–105, Jan. 2005. doi: 10.1007/s00706-004-0261-z.

[38] R. Brück, P. Hirth, M. Reizig, P. Treiber, and J. Breuer, “Metal Supported Flow-Through Particulate Trap; a Non-Blocking Solution,” 2001.

[39] B. A. A. L. Van Setten, M. Makkee, and J. A. Moulijn, “Science and technology of catalytic diesel particulate filters,” *Catalysis Reviews - Science and Engineering*, vol. 43, no. 4. pp. 489–564, Nov. 2001. doi: 10.1081/CR-120001810.

[40] M. J. Rauckis and W. J. Mclean, “The effect of hydrogen addition on ignition delays and flame propagation in spark ignition engines,” *Combustion Science and Technology*, vol. 19, no. 5–6, pp. 207–216, Apr. 1979, doi: 10.1080/00102207908946881.

[41] “ref no 41”.

[42] T. Qiu, J. G. Yang, X. J. Bai, and Y. L. Wang, “The preparation of synthetic graphite materials with hierarchical pores from lignite by one-step impregnation and their characterization as dye absorbents,” *RSC Adv*, vol. 9, no. 22, pp. 12737–12746, 2019, doi: 10.1039/c9ra00343f.

[43] P. Karin, P. Koko, C. Charoenphonphanich, N. Chollacoop, and K. Hanamura, “Physicochemical Characterization of Diesel Engine’s Soot and Metal Oxide Ash Nanoparticles Using Electron Microscopy, EDS and TGA,” *Emission Control Science and Technology*, vol. 7, no. 2, pp. 91–104, Jun. 2021, doi: 10.1007/s40825-021-00190-6.

[44] S. Bathmanabhan and S. N. Saragur Madanayak, “Analysis and interpretation of particulate matter - PM10, PM2.5 and PM1 emissions from the heterogeneous traffic near an urban roadway,” *Atmos Pollut Res*, vol. 1, no. 3, pp. 184–194, 2010, doi: 10.5094/APR.2010.024.

[45] J. B. Heywood, *Internal combustion engine fundamentals*. McGraw-Hill, 1988.

[46] M. Dalla Nora, T. D. M. Lanzanova, and H. Zhao, “Effects of valve timing, valve lift and exhaust backpressure on performance and gas exchanging of a two-stroke GDI engine with overhead valves,” *Energy Convers Manag*, vol. 123, pp. 71–83, Sep. 2016, doi: 10.1016/j.enconman.2016.05.059.

[47] I. A. Resitoglu, K. Altinisik, A. Keskin, S. Yildirimcan, K. Ocakoglu, and M. A. Omar, “Development of Fe2O3 based catalysts to control pollutant emissions in diesel engines,” *Fuel*, vol. 208, pp. 111–116, 2017, doi: 10.1016/j.fuel.2017.07.023.

[48] Z. Zhang *et al.*, “Effects of different diesel-ethanol dual fuel ratio on performance and emission characteristics of diesel engine,” *Processes*, vol. 9, no. 7, Jul. 2021, doi: 10.3390/pr9071135.

[49] B. J. Cooper and J. E. Thoss, “Role of NO in Diesel Particulate Emission Control.”

[50] V. Di Sarli, G. Landi, L. Lisi, A. Saliva, and A. Di Benedetto, “Catalytic diesel particulate filters with highly dispersed ceria: Effect of the soot-catalyst contact on the regeneration performance,” *Appl Catal B*, vol. 197, pp. 116–124, Nov. 2016, doi: 10.1016/j.apcatb.2016.01.073.

[51] D. Qi, M. Leick, Y. Liu, and C. F. F. Lee, “Effect of EGR and injection timing on combustion and emission characteristics of split injection strategy DI-diesel engine fueled with biodiesel,” *Fuel*, vol. 90, no. 5, pp. 1884–1891, May 2011, doi: 10.1016/j.fuel.2011.01.016.

[52] T. Grigoratos, G. Fontaras, B. Giechaskiel, and N. Zacharof, “Real world emissions performance of heavy-duty Euro VI diesel vehicles,” *Atmos Environ*, vol. 201, pp. 348–359, Mar. 2019, doi: 10.1016/j.atmosenv.2018.12.042.

[53] T. K. Hansen, M. Høj, B. B. Hansen, T. V. W. Janssens, and A. D. Jensen, “The Effect of Pt Particle Size on the Oxidation of CO, C3H6, and NO Over Pt/Al2O3 for Diesel Exhaust Aftertreatment,” *Top Catal*, vol. 60, no. 17–18, pp. 1333–1344, Nov. 2017, doi: 10.1007/s11244-017-0818-9.

APPENDIX A:

TEST RESULTS

A- 1. Fuel properties of B20

FOCUSLAB Fluid & Oil Analysis Technology

ISO 9001 : 2015 Certified

Focuslab Ltd

Customer Code : 20010
Customer Name : KMITL
Address : 3 Moo 2, Chalongkrung Road
Ladkrabang
Bangkok 10520

Test Code : 811A

Sample Information

Unit ID /
Sample Information Identification : B20
Unit type : FUEL
Oil type : DIESEL B20
Sampling Date : 22-Jun-21
Recieved Date : 22-Jun-21

Test Report Sample No 21063748

Test Description	Test Method	Test Result	Limit (a)
Apperance			
Color	Visual Inspection	Bright and Clear	Bright and Clear
Diesel Fuel			
Density at 15 C , g/cm^3	ASTM D4052	0.827	0.81 - 0.87
Cetane Index	ASTM D976	60.0	Min 50
Distillation , C	ASTM D86		
Initial Boiling Point		177.4	-
90%vol. Recovered		348.4	Max 357
Flash Point	ASTM D93	66.0	Min 52
Fatty Acid Methyl Ester, %vol	EN 14078	22.5	19 - 20
Pour Point , °C	ASTM D97	9.0	Max 10
Flow Properties			
Viscosity at 40 C , cSt	ASTM D445	3.1	1.8 - 4.1
Cleanliness			
Total Contamination , mg/kg	EN 12662	4.2	Max 24.0
Micro Carbon Residue (MCR) , %mass	ASTM D4530	<0.01	Max 0.3
Ash , %wt	ASTM D482	<0.001	Max 0.010
Total Sulfur Content , mg/kg	ASTM D5453	142	Max 50
Water Content , mg/kg	ASTM D6304	1183	Max 300
Water and Sediment , %Vol.	ASTM D2709	<0.01	Max 0.05

Interpretation of the Test Result
- Test results are based on received fuel sample , submitted and identified by client.
- Data is provided above.

Recommendation
- No recommendation for R&D.

Remark
(a) Diesel fuel is from Thailand Diesel Specification - MOE - 2563

Tested and Issued By

Kanjana K.
Lab Technologist

Approved and Authorised by

Somchai J.
Machine Lubricant Analyst

2/57 Bangna Complex Office Tower, 12 th Fl , Soi Bangna- Trad 25, North Bangna, Bangna, Bangkok 10260, Thailand
http://www.focuslab.co.th
Tel : (66 2) 3618600-3 Fax : (66 2) 3618567

FOCUSLAB™ Fluid & Oil Analysis Technology

ISO 9001 : 2015 Certified

Focuslab Ltd

Customer Code	:	20010
Customer Name	:	KMITL
Address	:	3 Moo 2, Chalongkrung Road Ladkrabang Bangkok 10520
Test Code	:	811A

Sample Information

Unit ID / Sample Information Identification	:	B20
Unit type	:	FUEL
Oil type	:	DIESEL B20
Sampling Date	:	22-Jun-21
Recieved Date	:	22-Jun-21

B20

Good and Qualified Diesel Fuel

A-2. Biodiesel's physical and chemical properties

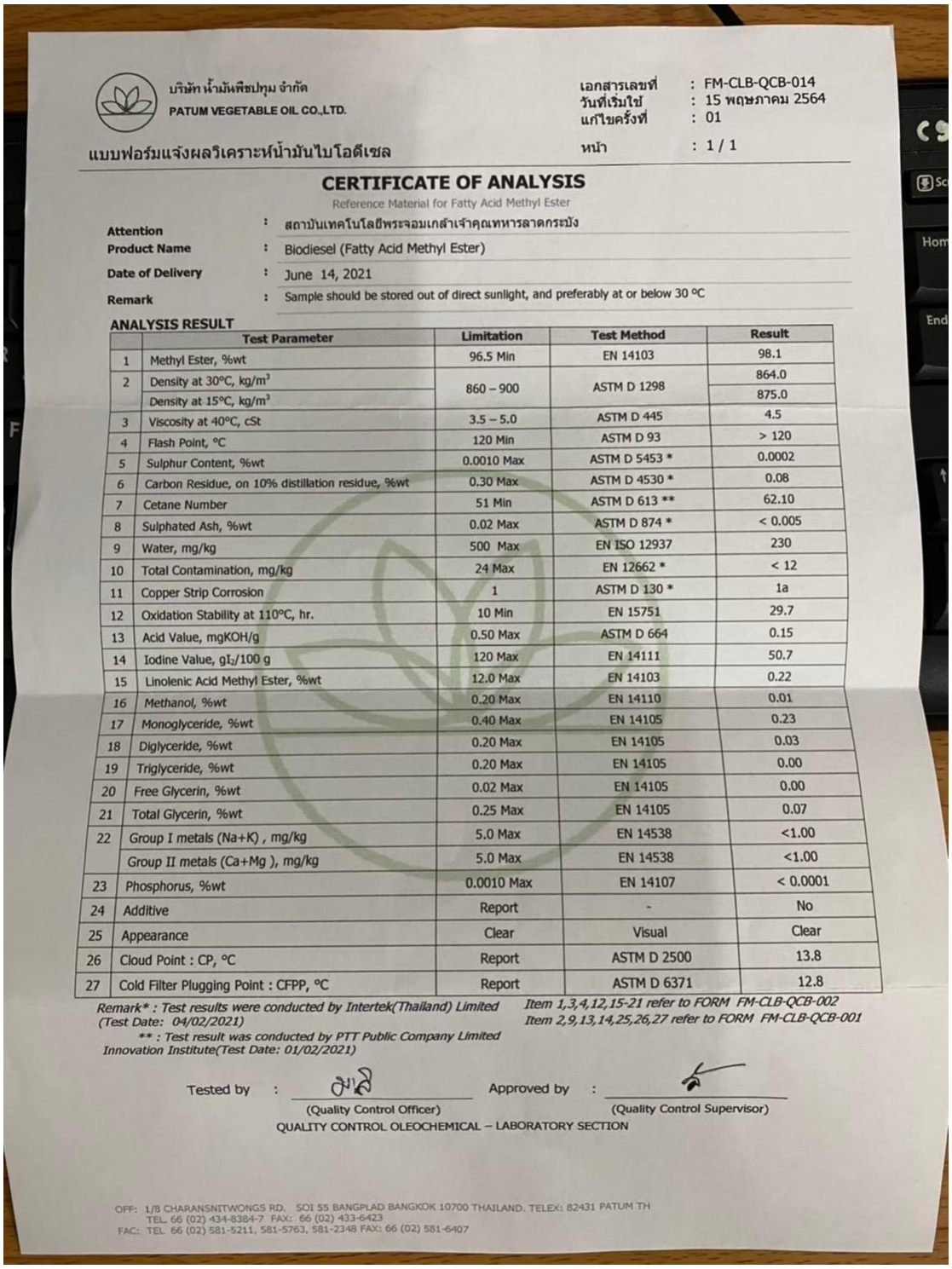

บริษัท น้ำมันพืชปทุม จำกัด
PATUM VEGETABLE OIL CO.,LTD.

เอกสารเลขที่ : FM-CLB-QCB-014
วันที่เริ่มใช้ : 15 พฤษภาคม 2564
แก้ไขครั้งที่ : 01
หน้า : 1 / 1

แบบฟอร์มแจ้งผลวิเคราะห์น้ำมันไบโอดีเซล

CERTIFICATE OF ANALYSIS

Reference Material for Fatty Acid Methyl Ester

Attention : สถาบันเทคโนโลยีพระจอมเกล้าเจ้าคุณทหารลาดกระบัง
Product Name : Biodiesel (Fatty Acid Methyl Ester)
Date of Delivery : June 14, 2021
Remark : Sample should be stored out of direct sunlight, and preferably at or below 30 °C

ANALYSIS RESULT

	Test Parameter	Limitation	Test Method	Result
1	Methyl Ester, %wt	96.5 Min	EN 14103	98.1
2	Density at 30°C, kg/m^3	860 – 900	ASTM D 1298	864.0
	Density at 15°C, kg/m^3			875.0
3	Viscosity at 40°C, cSt	3.5 – 5.0	ASTM D 445	4.5
4	Flash Point, °C	120 Min	ASTM D 93	> 120
5	Sulphur Content, %wt	0.0010 Max	ASTM D 5453 *	0.0002
6	Carbon Residue, on 10% distillation residue, %wt	0.30 Max	ASTM D 4530 *	0.08
7	Cetane Number	51 Min	ASTM D 613 **	62.10
8	Sulphated Ash, %wt	0.02 Max	ASTM D 874 *	< 0.005
9	Water, mg/kg	500 Max	EN ISO 12937	230
10	Total Contamination, mg/kg	24 Max	EN 12662 *	< 12
11	Copper Strip Corrosion	1	ASTM D 130 *	1a
12	Oxidation Stability at 110°C, hr.	10 Min	EN 15751	29.7
13	Acid Value, mgKOH/g	0.50 Max	ASTM D 664	0.15
14	Iodine Value, gI_2/100 g	120 Max	EN 14111	50.7
15	Linolenic Acid Methyl Ester, %wt	12.0 Max	EN 14103	0.22
16	Methanol, %wt	0.20 Max	EN 14110	0.01
17	Monoglyceride, %wt	0.40 Max	EN 14105	0.23
18	Diglyceride, %wt	0.20 Max	EN 14105	0.03
19	Triglyceride, %wt	0.20 Max	EN 14105	0.00
20	Free Glycerin, %wt	0.02 Max	EN 14105	0.00
21	Total Glycerin, %wt	0.25 Max	EN 14105	0.07
22	Group I metals (Na+K) , mg/kg	5.0 Max	EN 14538	<1.00
	Group II metals (Ca+Mg), mg/kg	5.0 Max	EN 14538	<1.00
23	Phosphorus, %wt	0.0010 Max	EN 14107	< 0.0001
24	Additive	Report	-	No
25	Appearance	Clear	Visual	Clear
26	Cloud Point : CP, °C	Report	ASTM D 2500	13.8
27	Cold Filter Plugging Point : CFPP, °C	Report	ASTM D 6371	12.8

Remark : Test results were conducted by Intertek(Thailand) Limited (Test Date: 04/02/2021)*
*** : Test result was conducted by PTT Public Company Limited Innovation Institute(Test Date: 01/02/2021)*

Item 1,3,4,12,15-21 refer to FORM FM-CLB-QCB-002
Item 2,9,13,14,25,26,27 refer to FORM FM-CLB-QCB-001

Tested by : _____ (Quality Control Officer)
Approved by : _____ (Quality Control Supervisor)

QUALITY CONTROL OLEOCHEMICAL – LABORATORY SECTION

OFF: 1/8 CHARANSNITWONGS RD. SOI 55 BANGPLAD BANGKOK 10700 THAILAND. TELEX: 82431 PATUM TH
TEL. 66 (02) 434-8384-7 FAX: 66 (02) 433-6423
FAC: TEL. 66 (02) 581-5211, 581-5763, 581-2348 FAX: 66 (02) 581-6407

A-3. Bomb calorimeter test results

Analysis Report

Sample	Biodiesel
Sample owner	King Mongkut's Institute of Technology Ladkrabang
Objective	To analyse heating value of combustion
Instrument	Automatic Bomb Calorimeter ; Leco model AC - 500
Job ID	640707-9246
Analysis Date	July 28, 2021

Results

Sample name	Heating value of combustion (MJ/kg)		
	#1	#2	Average
Biodiesel B7	45.26	45.24	45.25
Biodiesel B10	45.80	45.46	45.63
Biodiesel B20	44.89	45.01	44.95
Biodiesel B100	39.84	40.03	39.94
Biodiesel B20E5	43.90	43.99	43.95
Biodiesel B20E10	42.66	42.78	42.72
Biodiesel B20E20	40.61	40.45	40.53

(Mrs. Aree Limnirandorn)

Analyst

A- 4. Chemical compositions test results

EagerSmart

Method name : CHNS
Method filename : E:\...\65-002\CHNS.mth

Detection and integration parameters

Time base : (s)
Peak width : 10
Peak threshold : 1
Minimum area : 1500
Skim ratio : 10
Next sample to acquire : 19
Real time plot scale : 10
Real time plot offset : 0

Time events table

#	Time	Events type	New value
1	.1	Disable integration	
2	35	Enable integration	
3	160	Change peak threshold	.1
4	160	Change skim ratio	1
5	160	Change peak width	40
6	500.3922	Disable integration	

Calculation and report parameters

Calibration method : Linear fit
Heat Value calc. : No
CO2 Emission Factor calc. : No
Protein calc. : No
Report on : None
Peak option : Only calibrated peaks
Report format : Default
Report publisher : No
Calibration report : Yes
Concentration unit :
Stripchart format : None
Autoscalling : ---
Stripchart full scale : 10
Stripchart scale offset : 0
Stripchart initial time : 0
Stripchart end time : 600
Append for summarize : Element %
Signal to noise report : Yes
Signal peak name :
Noise evaluation from/to : 0.0-0.0(s):

Custom report

Component table

#	Component name	Ret.T.	Window	Min. %	Max.%
1	Nitrogen	47	10		
2	Carbon	67	14		
3	Hydrogen	194	60		
4	Sulphur	412	88		

Calibration factors

#	Component name	Kb	Kc
1	Nitrogen	1995673	0
2	Carbon	4763351	0
3	Hydrogen	1.488643E+07	0
4	Sulphur	2078495	0

Standard table

Sample Num.4 Sample name: STD1 (BBOT 1.5 mg)
Filename: File004 STD1 (BBOT 1_5 mg) Std name: BBOT

#	Component name	Concentration	Valid
1	Nitrogen	6.53	Yes
2	Carbon	72.58	Yes
3	Hydrogen	6.1	Yes
4	Sulphur	7.41	Yes

Sample Num.5 Sample name: STD2 (BBOT 2 mg)
Filename: File005 STD2 (BBOT 2 mg) Std name: BBOT

#	Component name	Concentration	Valid
1	Nitrogen	6.53	Yes
2	Carbon	72.58	Yes
3	Hydrogen	6.1	Yes
4	Sulphur	7.41	Yes

Sample Num.6 Sample name: STD3 (BBOT 2.5 mg)
Filename: File006 STD3 (BBOT 2_5 mg) Std name: BBOT

#	Component name	Concentration	Valid
1	Nitrogen	6.53	Yes
2	Carbon	72.58	Yes
3	Hydrogen	6.1	Yes
4	Sulphur	7.41	Yes

Sample Num.7 Sample name: STD4 (BBOT 3 mg)
Filename: File007 STD4 (BBOT 3 mg) Std name: BBOT

#	Component name	Concentration	Valid
1	Nitrogen	6.53	Yes
2	Carbon	72.58	Yes
3	Hydrogen	6.1	Yes
4	Sulphur	7.41	Yes

Operator ID/info

Operator ID :
Company name :
Column type :
Column lenght :
Date packing :
Comment :

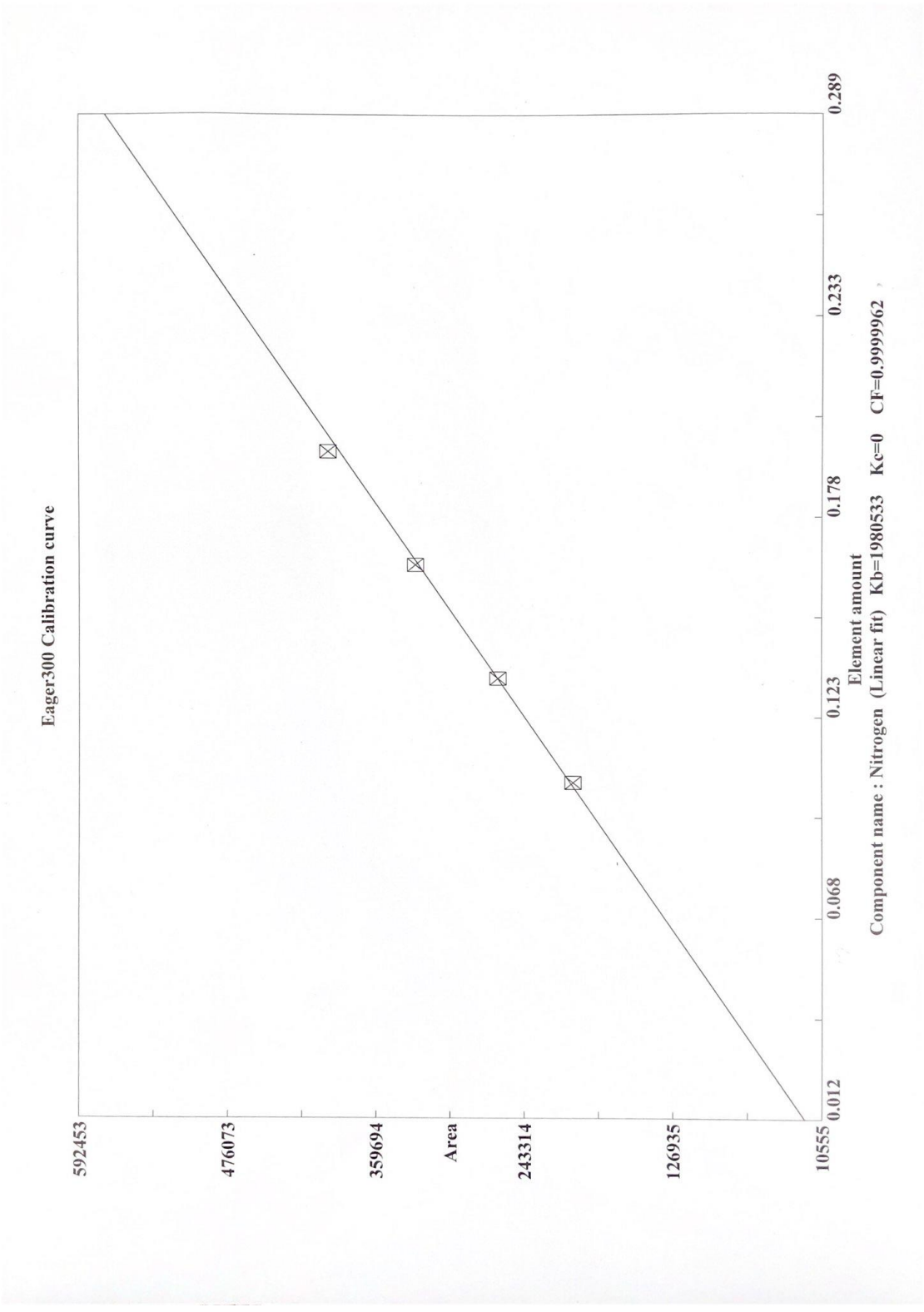
Eager300 Calibration curve
592453
476073
359694
243314
126935
10555
Area
0.012
0.068
0.123
0.178
0.233
0.289
Element amount
Component name : Nitrogen (Linear fit) Kb=1980533 Kc=0 CF=0.9999962

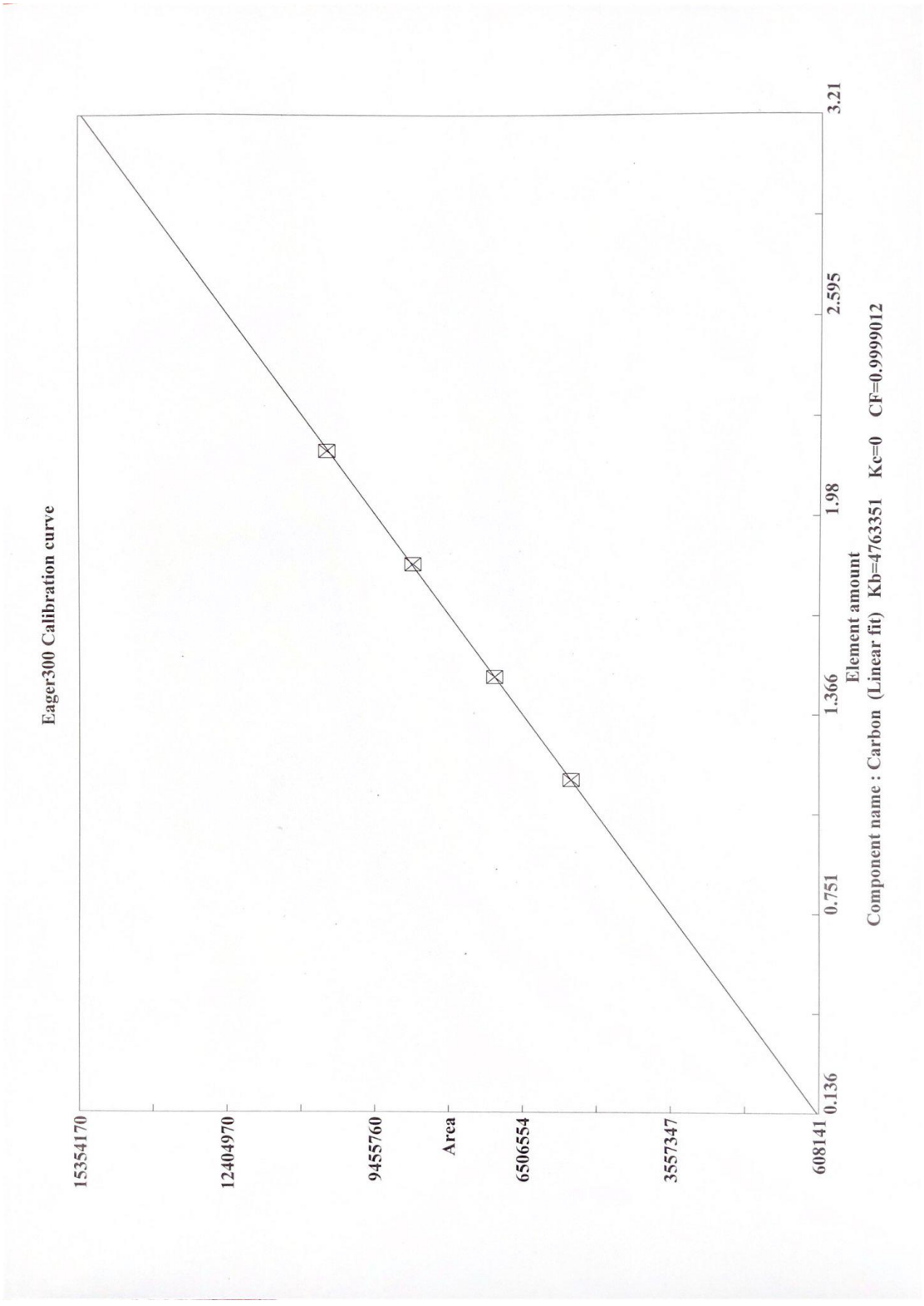
Eager300 Calibration curve
15354170
12404970
9455760
6506554
3557347
608141
Area
0.136
0.751
1.366
1.98
2.595
3.21
Element amount
Component name : Carbon (Linear fit) Kb=4763351 Kc=0 CF=0.9999012

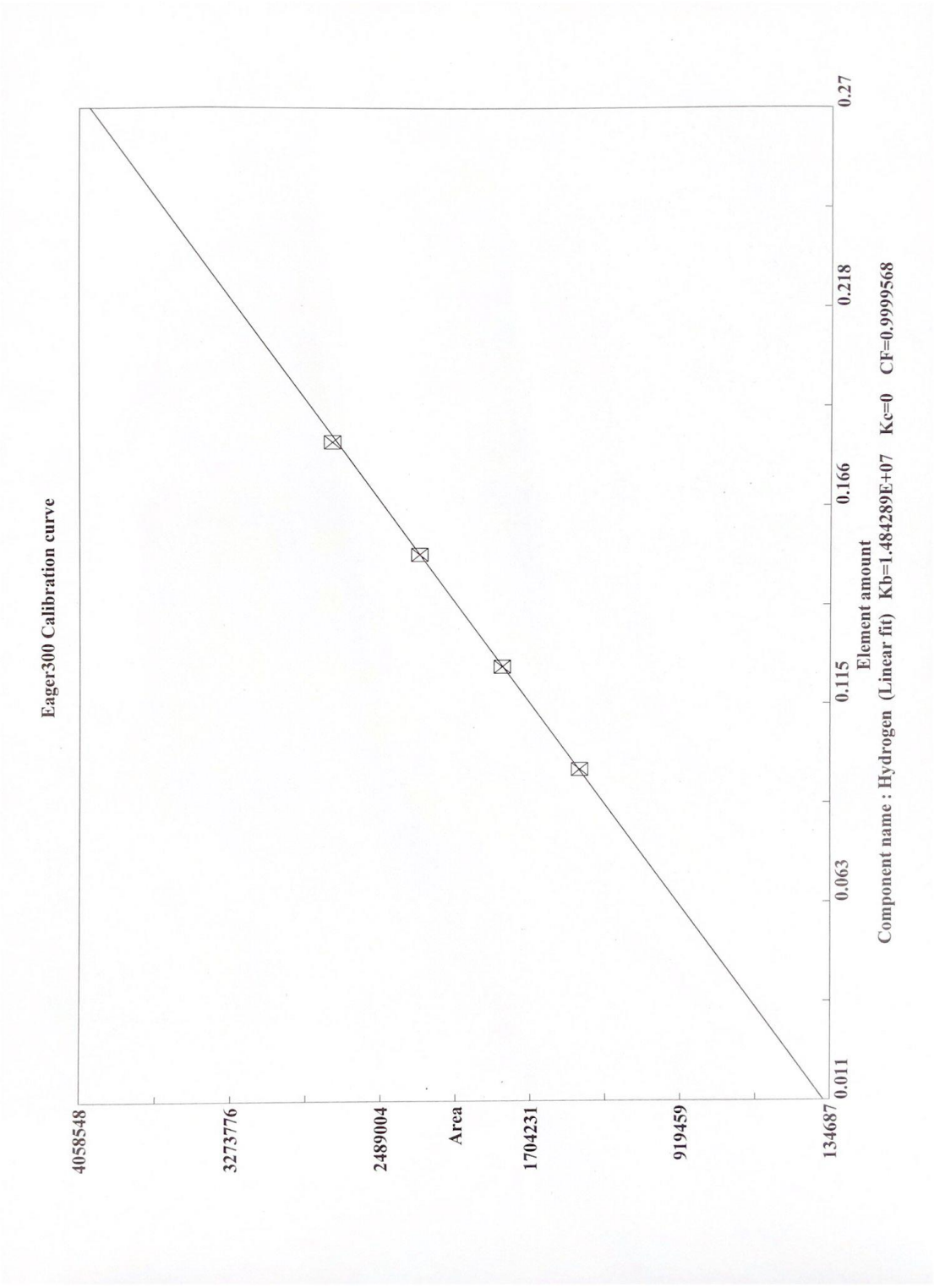
Eager300 Calibration curve
4058548
3273776
2489004
1704231
919459
134687
Area
0.011
0.063
0.115
0.166
0.218
0.27
Element amount
Component name : Hydrogen (Linear fit) Kb=1.484289E+07 Kc=0 CF=0.9999568

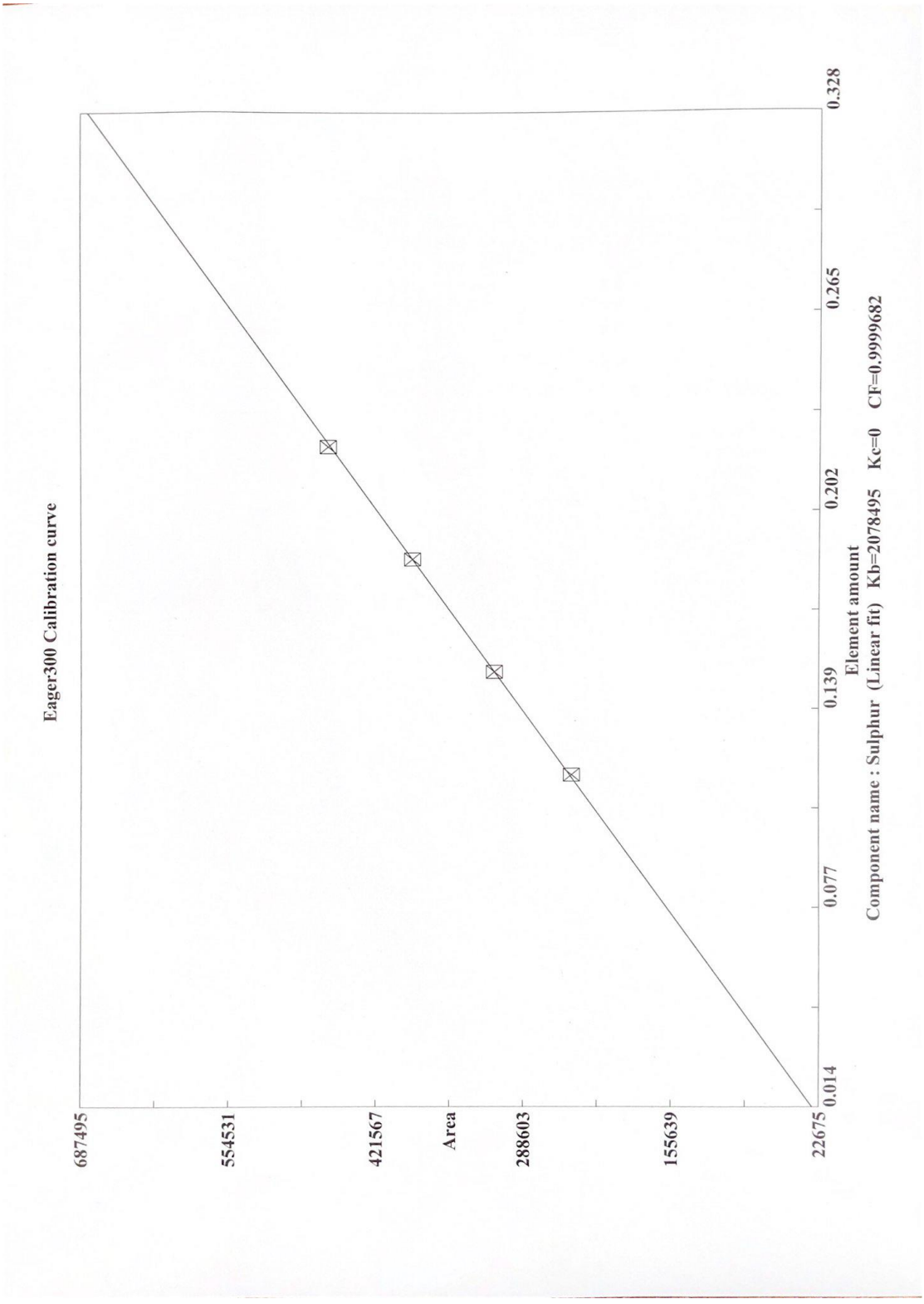
Eager300 Calibration curve
687495
554531
421567
288603
155639
22675
Area
0.014
0.077
0.139
0.202
0.265
0.328
Element amount
Component name : Sulphur (Linear fit) Kb=2078495 Kc=0 CF=0.9999682

EagerSmart Summarize Results

Date : 11/08/2021 at 15:52:41
Method Name : CHNS
Method Filename : CHNS.mth

Group No : 1 Sample Name	Element % Nitrogen	Carbon	Hydrogen	Sulphur
B100_1	0	76.40828705	12.38687801	0
B100_4	0	77.04006958	12.53007603	0
B20_2	0	82.24542999	13.38155937	0
B20_3	0	82.98455048	13.52551937	0
B10_1	0	84.58450317	13.53221703	0
B10_2	0	84.74507141	13.58557034	0

6 Sample(s) in Group No : 1

Component Name	Average	Std. Dev.	% Rel. S. D.	Variance
Nitrogen	0	0.00000	0.0000	0.0000
Carbon	81.33465195	3.70018	4.5493	13.6913
Hydrogen	13.15697002	0.54714	4.1586	0.2994
Sulphur	0	0.00000	0.0000	0.0000

A- 5.TEM-EDS raw data

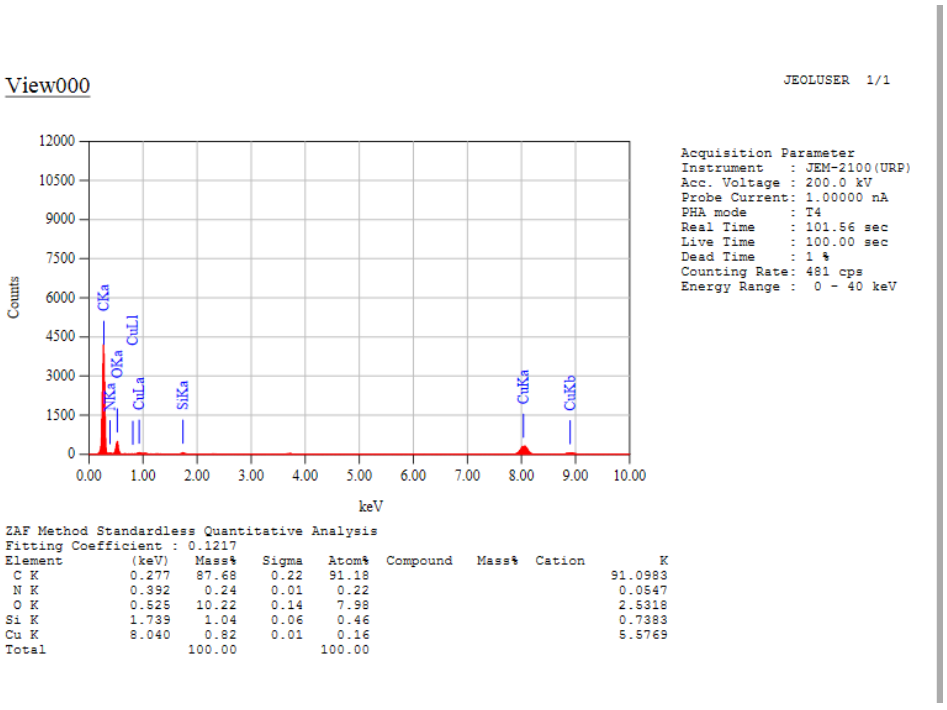

A- 6 XRD raw data

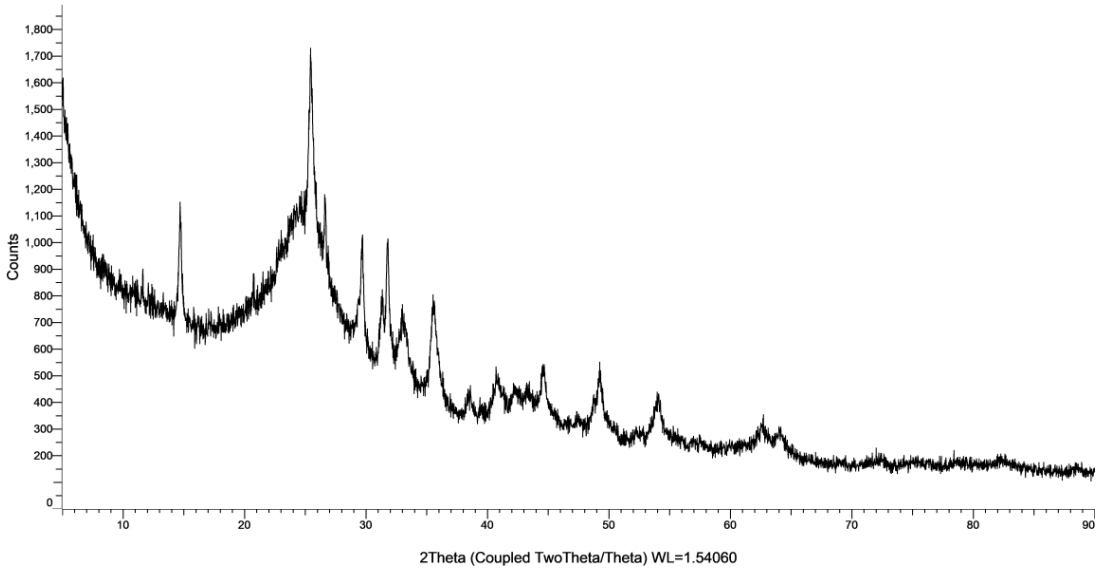

NSTDA Characterization and Testing Service Center

NCTC
NSTDA Characterization and Testing Service Center

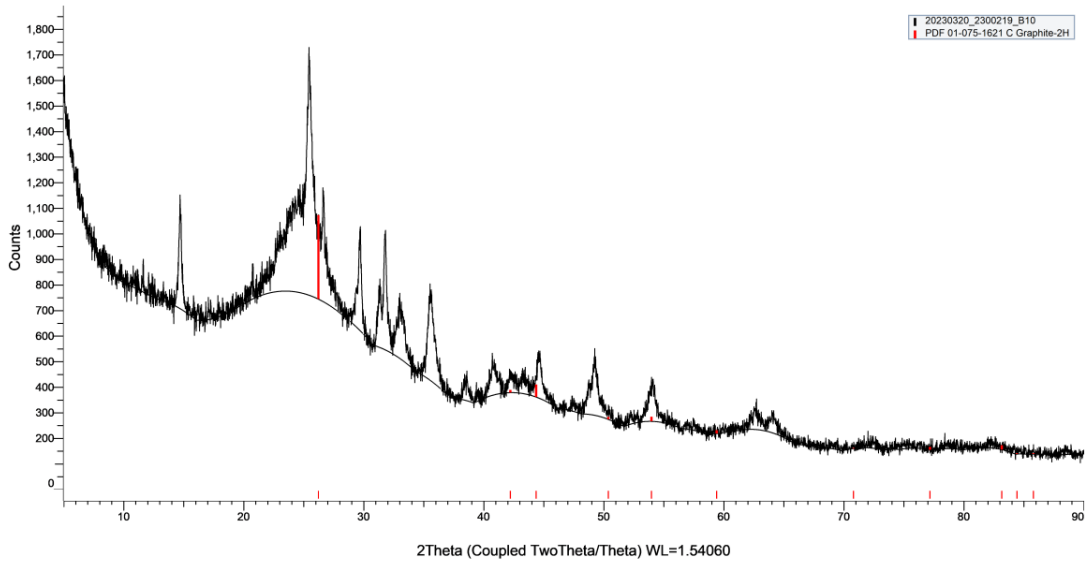

NSTDA Characterization and Testing Service Center

NCTC
NSTDA Characterization and Testing Service Center

APPENDIX B:

CONFERENCE PARTICIPATION

The 12th TSME International Conference on Mechanical Engineering
13th – 16th December 2022
Phuket, Thailand

AEC0013

Impact of Retrofit Partial Flow Diesel Particulate Filter on Diesel Engine Combustion and Particle Emissions Characteristics

M. Thin[1], P. Karin[1], M. Srilomsak[1,*], C. Charoenphonphanich[1], W. Po-ngaen[2], P. Saisirirat[3], N. Chollacoop[3], H. Kosaka[4]

[1]School of Engineering, King Mongkut's Institute of Technology Ladkrabang, Bangkok 10520, Thailand
[2]Faculaty of Technical Education, King Mongkut's University of Technology, North Bangkok, Bangkok 10800, Thailand
[3]National Energy Technology Centre, National Science and Technology Development Agency, Pathum Thani 12120, Thailand
[4]School of Engineering, Tokyo Institute of Technology, Tokyo 152-8552, Japan

* Corresponding Author: mek.sr@kmitl.ac.th

Transactions of the TSME (2022) Vol. 10, No. 2
Journal of Research and Applications in Mechanical Engineering
ISSN: 2229-2152 (Print); 2697-424x (Online)
Paper No. JRAME-22-10-008
DOI: 10.14456/jrame.2022.8

Research Article

VISUALIZATION OF SOOT NANOSTRUCTURE FROM ETHANOL BLENDED BIODIESEL USING ELECTRON MICROSCOPY IMAGE ANALYSES

Myat Hsu Thin[1]
P. Karin[1]
M. Srilomsak[1,*]
W. Po-ngen[2]
P. Saisirirat[3]
N. Chollacoop[3]
H. Kosaka[4]
[1] School of Engineering, King Mongkut's Institute of Technology Ladkrabang, Bangkok 10520, Thailand
[2] Faculty of Technical Education, King Mongkut's University of Technology North Bangkok, Bangkok 10800, Thailand
[3] National Energy Technology Center, National Science and Technology Development Agency, Pathum Thani 12120, Thailand
[4] School of Engineering, Tokyo Institute of Technology, Tokyo 152-8552, Japan

Received 21 June 2022
Revised 16 July 2022
Accepted 20 July 2022

ABSTRACT:
Characteristics of particulate matter from ethanol-blended biodiesel on the diesel engine in terms of nanostructure were investigated through electron microscopy. Commercial B20 fuel (20% palm and 80% diesel) was used as the baseline fuel and ethanol was blended at 5% and 10% with B20 fuel. The agglomerated particle size was reduced by increasing the weight ratio of ethanol. The average diameter sizes of the single primary nanoparticles of B20, B20E5, and B20E10 are about 20-40 nm while inter-planar spacing is about 0.404 nm, 0.383 nm, and 0.352 nm, respectively. The total fringe lengths of B20, B20E5, and B20E10 are approximately 521 nm, 470 nm, and 262 nm measured from the areas of 20 nm x 20 nm of primary nanoparticles.

Keywords: *Particulate Matter, Electron Microscopy, Diesel Engine, Biodiesel, Soot nanostructure*

APPENDIX C:

INTERNATIONAL JOURNAL SUBMISSION

Evaluation of Particle Emissions Emitted from a Light-duty Diesel Vehicle Equipped with Retrofit Ceria and Platinum Partial Flow Diesel Particulate Filters

MyatHsu Thin[a], Plan Teekatasn Cosh[a], Poonnut Thaeviriyakul[a], Phobkrit Kanokkhanarat[a], Mek Srilomsak[a], Chinda Charoenphonphanich[a], Manop Masomtob[b], Peerawat Saisirirat[b], Sompong Srimanosaowapak[c], Watcharin Po-ngaen[d], Hidenori Kosaka[e], Preechar Karin[a,*]

[a] School of Engineering, King Mongkut's Institute of Technology Ladkrabang, Bangkok, 10520, Thailand
[b] National Energy Technology Center, National Science and Technology Development Agency, Pathum Thani, 12120, Thailand
[c] National Metal and Materials Technology Center, National Science and Technology Development Agency, Pathum Thani, 12120, Thailand
[d] Faculty of Technical Education, King Mongkut's University of Technology North Bangkok, Bangkok 10800, Thailand
[e] School of Engineering, Tokyo Institute of Technology, Tokyo, 152-8552, Japan

* Corresponding author: preechar.ka@kmitl.ac.th

Effect of Metallic Microfiber Partial-flow Diesel Particulate Filter on Combustion analysis and Emission Characteristics using Biodiesel Blends

MyatHsu Thin[a], Hai Liu[a], Poonnut Thaeviriyakul[a], Phyo Wai[a], Chaiwat Nuthong[a], Mek Srilomsak[a], Chinda Charoenphonphanich[a], Manop Masomtob[b], Peerawat Saisirirat[b], Sompong Srimanosaowapak[c], Watcharin Po-ngaen[d], Hidenori Kosaka[e], Preechar Karin[a,*]

[a] School of Engineering, King Mongkut's Institute of Technology Ladkrabang, Bangkok, 10520, Thailand
[b] National Energy Technology Center, National Science and Technology Development Agency, Pathum Thani, 12120, Thailand
[c] National Metal and Materials Technology Center, National Science and Technology Development Agency, Pathum Thani, 12120, Thailand
[d] Faculty of Technical Education, King Mongkut's University of Technology North Bangkok, Bangkok 10800, Thailand
[e] School of Engineering, Tokyo Institute of Technology, Tokyo, 152-8552, Japan

* Corresponding author: preechar.ka@kmitl.ac.th

APPENDIX D:

REVISED QUESTIONS AND ANSWERS

Questions by Prof. Dr. Hidenori Kosaka

Q1. How to confirm the average temperature inside the combustion chamber using measured pressure data?

Revised Answer

By using only, the information of pressure versus volume diagram and pressure versus crank angle, the explanation for the impact of employing partial flow filter system may not be enough. Therefore, temperature versus crank angle diagram was provided as an additional information to compare the combustion characteristics of the engine with and without employing the partial flow filter by using the ideal gas law equation, PV = mRT. In the Figure, at 1000 rpm, the temperature during the intake and exhaust stroke increased because of the increased residual gas fraction inside the chamber due to the backpressure. However, it became stable at 1500 and 2000 rpm and at these engine conditions, the temperature of the combustion and power stroke increased because the heat loss and exhaust loss were reduced by the P-DPF system. The detail comparisons of the temperature vs crank angle diagram are added in Section 4.2.1 as Figure 4-11.

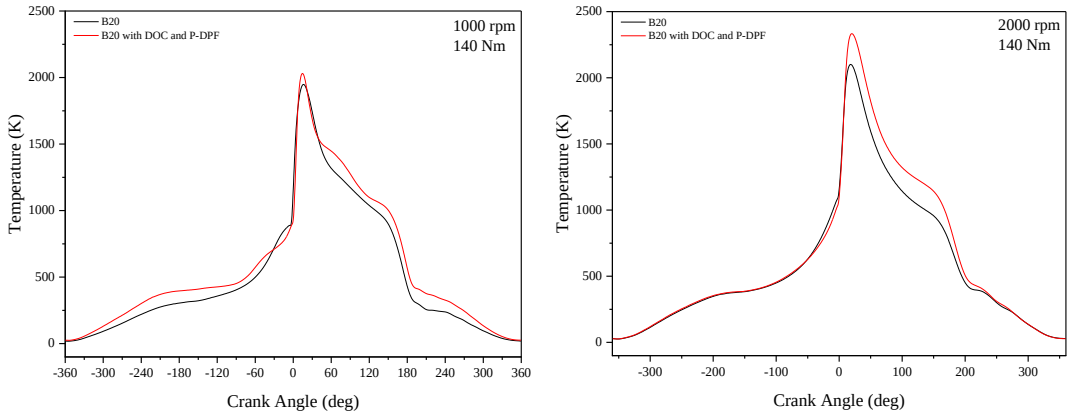

Q2. What is the main reason for the increase in difference between ITE and BTE by adding the P-DPF system?

Revised Answer

With the installation of the partial filter system, the indicated power increased which might also lead to incrased the indicated thermal efficiency with same power input. However, the installation of the partial filter had no significant impact on the fuel

consumption, brake specific fuel consumption as well as brake thermal efficiency. Therefore, the difference between ITE and BTE with P-DPF system was higher than that without P-DPF because the friction loss increased due to the backpressure from the after-treatment system.

Questions by Dr. Peerawat Saisirirat

Q1. How to measure the pressure drop and where do the pressure sensors set up?

Revised Answer

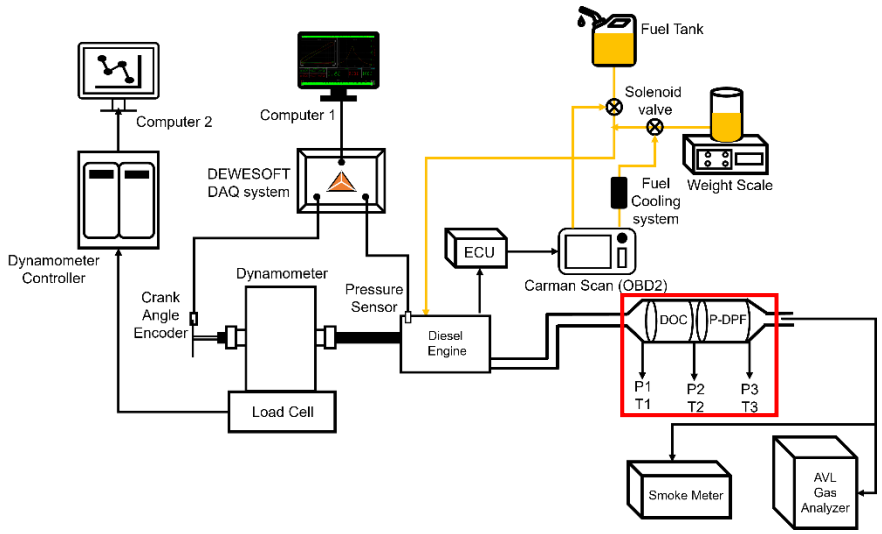

In the study, three pressure sensors were strategically deployed at distinct locations, namely, upstream of the Diesel Oxidation Catalyst (DOC), upstream of the Particulate Diesel Particulate Filter (P-DPF), and downstream of the P-DPF, in order to monitor pressure variations under various engine operating conditions. The pressure differentials across the DOC and P-DPF were individually examined and subsequently aggregated to derive the cumulative total pressure drop.

Q2. Was the fuel temperature controlled during the engine operation?

Revised Answer

In the context of the fuel supply system, three solenoid valves were employed to control the processes of fuel recirculation and fuel drainage. To ensure temperature regulation, a water-cooling system was employed to maintain the temperature of the recirculated fuel from the engine at a constant 50 degrees Celsius.

Q3. Compare the emissions results of diesel engine and vehicle?

Revised Answer

In diesel engine analysis, P-DPF achieved an average of 65% PM reduction. Moreover, NO and O2 decreased while CO2 increased. As a hypothesis analysis, the trapped PM on the partial filter could be oxidized by both NO2 and O2. However, in the diesel vehicle analysis, P-DPF system can reduce PN and PM from 40-66% and ceria coated P-DPF showed a better PN and PM reduction performance. NOx and CO2 were not significantly affected by the installation of P-DPF. The oxidation of PM could not be occurred due to the short duration testing and under no load condition.

Questions by Asst. Prof. Dr. Chinda Charoenpphonphanich

Q1. Can you explain clearly about the conversion of NO to NO2 in DOC and the reaction of NO2 with soot in P-DPF at slide number 29?

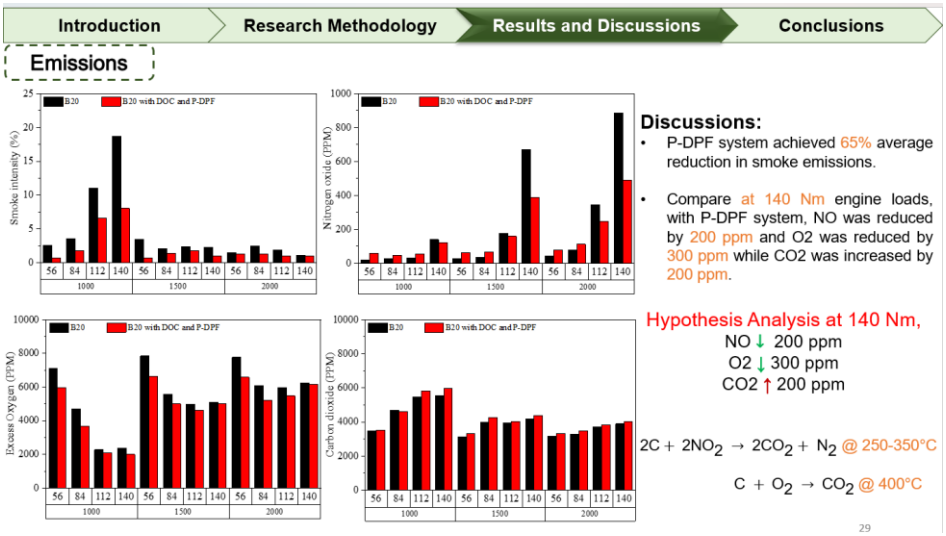

Revised Answer

The experimental AVL gas analyzer in this study could only focus on the measurement of nitrogen oxide (NO). Upon implementing the P-DPF system, significant reductions in both NO and O_2 emissions were observed, amounting to decreases of 200 ppm and 300 ppm, respectively. Concurrently, there was an increase of 200 ppm in CO_2 emissions. As a part of our hypothesis-driven analysis, it is postulated that the diesel oxidation catalyst, featuring a ceria coating, facilitated the conversion of NO to NO_2. Subsequently, NO_2 was utilized in the partial flow filter for the oxidation of soot, following the chemical reactions delineated by the subsequent equations.

In Diesel Oxidation Catalyst (DOC),

$$NO + \frac{1}{2}O_2 \rightarrow NO_2 \quad \text{at } 200°C$$

In Partial flow Diesel Particulate Filter (P-DPF),

$$2C\ (PM) + 2NO_2 \rightarrow 2CO_2 + N_2 \quad \text{at } 250\text{-}350°C$$

$$C\ (PM) + O_2 \rightarrow CO_2 \quad \text{at } 400°C$$

Question by Dr. Nuwong Chollacoop

Q1. Have you monitored the regeneration efficiency of the partial-flow filter during the test?

Revised Answer

In the context of this research, the primary emphasis lies not in the quantification of regeneration efficiency but rather in the comprehensive exploration of various facets encompassing emissions reduction, engine combustion dynamics, and overall engine performance. Moreover, the measurement of regeneration efficiency pertaining to soot in the Partial Flow Diesel Particulate Filter (P-DPF) entails intricate experimental configurations and demanding data analysis processes, which demand a significant allocation of time and resources. Nevertheless, it is imperative to underline that the soot oxidation was substantiated by monitoring exhaust temperatures. Specifically, in the thermogravimetric analysis (TGA) conducted by H.M. Oo et al. [22], it was established that the oxidation of diesel particulate matter commenced at approximately 400°C. In the current investigation, exhaust temperatures consistently reached or exceeded 400°C, notably observed at an engine load of 140 Nm across various engine speeds. For additional reference, the left figure presents a profile depicting the relationship between PM oxidation rate and temperature derived from pertinent literature, while the right figure showcases the exhaust temperature measurements derived from the current study.

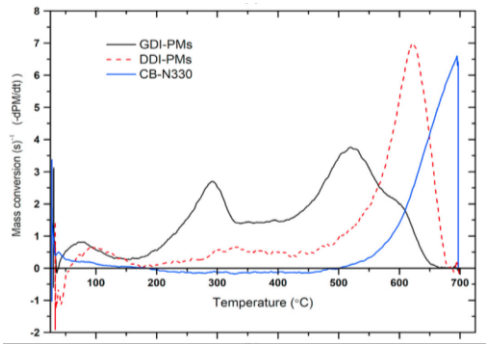

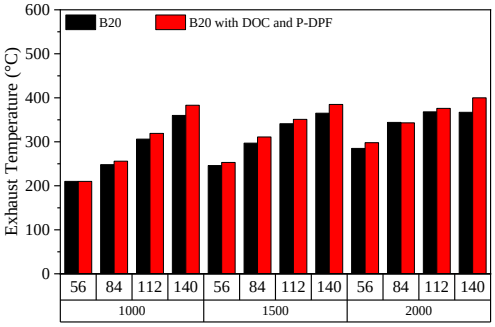

Q2. How much is the exact composition of fatty acid methyl ester in the fuel blend?

Revised Answer

The composition of fatty acid methyl ester (% vol) is added in the fuel properties as shown in Table. The detail test report of fuel properties is provided in Appendix A.

Fuel Properties	**Standard**	**B20**
Calorific Value (MJ/kg)	ASTM D 240	44.95
Viscosity @ 40°C (mm^2/s)	ASTM D 445	3.1
Density @ 15°C (kg/m^3)	ASTM D 1298	827
Distillation (°C)	ASTM D 86-11b	
T10		177.4
T90		348.4
Carbon (% mass)	ASTM D 5291	82.61
Hydrogen (% mass)	ASTM D 5291	13.45
Oxygen (% mass)	ASTM D 5291	3.94
Fatty Acid Methyl Ester (% vol)	EN 14078	22.5

AUTHOR BIOGRAPHY

Author: Ms. Myat Hsu Thin
Nationality: Myanmar
Email: 64601179@kmitl.ac.th

Education:

2023 Master of Automotive and Advance Transportation Engineering
Faculty of Engineering, King Mongkut's Institute of Technology Ladkrabang

2019 Bachelor of Engineering, Mechanical Engineering
Yangon Technological University (COE)

Conference Participation Publications:

[1] M. Thin, P. Karin, M. Srilomsak, C. Charoenphonphanich, W. Po-ngaen, P. Saisirirat, N. Chollacoop and H. Kosaka "Impact of Retrofit Partial Flow Diesel Particulate Filter on Diesel Engine Combustion and Particle Emissions Characteristics.", 12th TSME International Conference on Mechanical Engineering Proceedings, 2022.

[2] Myat Hsu Thin, Preechar Karin, Mek Srilomsak, Watcharin Po-ngen, Peerawat Saisirirat, Nuwong Chollacoop, Hidenori Kosaka, "Visualization of Soot Nanostructure from Ethanol Blended Biodiesel using Electron Microscopy Image Analysis", The 16th ASIAN SYMPOSIUM ON VISUALIZATION (ASV16), (Published in Journal of Research and Applications in Mechanical Engineering, Jrame)

[3] M. Thin, PT. Cosh, P. Thaeviriyakul, P. Kanokkhanarat, M. Srilimsak, C. Charoenphonphanich, M. Masomtob, P. Saisirirat, S. Srimanosaowapak, W. Po-ngaen, H. Kosaka, P. Karin, "Evaluation of Particle Emissions Emitted from a Light-duty Diesel Vehicle Equipped with Retrofit Ceria and Platinum Partial Flow Diesel Particulate Filters" Submitted, 2023

[4] M. Thin, H. Liu, P. Thaeviriyakul, P. Wai, C. Nuthong, M. Srilimsak, C. Charoenphonphanich, M. Masomtob, P. Saisirirat, S. Srimanosaowapak, W. Po-ngaen, H. Kosaka, P. Karin, "Effect of Metallic Microfiber Partial-flow Diesel

Particulate Filter on Combustion analysis and Emission Characteristics using Biodiesel Blends", Submitted, 2023.